

Electronic Thesis and Dissertation Repository

7-28-2022 2:00 PM

Simulation of non-homogeneous wind processes, comparison between numerical and experimental model of a bridge

Héctor Hernández Landero, *The University of Western Ontario*

Supervisor: Hong, Han-Ping, *The University of Western Ontario*

Co-Supervisor: Zhou, Wenxing, *The University of Western Ontario*

A thesis submitted in partial fulfillment of the requirements for the Doctor of Philosophy degree in Civil and Environmental Engineering

© Héctor Hernández Landero 2022

Follow this and additional works at: <https://ir.lib.uwo.ca/etd>



Part of the [Structural Engineering Commons](#)

Recommended Citation

Hernández Landero, Héctor, "Simulation of non-homogeneous wind processes, comparison between numerical and experimental model of a bridge" (2022). *Electronic Thesis and Dissertation Repository*. 8996.

<https://ir.lib.uwo.ca/etd/8996>

This Dissertation/Thesis is brought to you for free and open access by Scholarship@Western. It has been accepted for inclusion in Electronic Thesis and Dissertation Repository by an authorized administrator of Scholarship@Western. For more information, please contact wlsadmin@uwo.ca.

Abstract

The scaled aerodynamic model of a bridge is often tested in the boundary layer wind tunnel laboratory (BLWTL). In this study a numerical model of the Baluarte Bridge subjected to wind loading is investigated. The scaled full bridge aerodynamic model was previously studied at the University of Western Ontario, Canada. For the numerical model a finite element model (FEM) is implemented, and the characterization of the buffeting forces are considered on the frequency and time domain. In the former case, the so-called pseudo excitation method is used to characterize the wind load, while in the latter the spectral representation method (SRM) is used to generate the synthetic wind speed field. In both cases, an inhomogeneous stochastic process is generated. The corresponding energy of the wind is formulated in terms of the power spectral density function, and appropriate coherence functions. Apart from the formulation of non-homogeneous wind, the simulation of non-stationary fluctuating winds at multiple points is also considered.

Both the frequency domain approach and the time domain approach are used to evaluate the root-mean-square (RMS) displacements, due to the fluctuating horizontal and vertical winds. For the time domain, the lateral RMS displacement obtained from the FEM is similar to the one obtained on the experimental tests. In contrast, for the frequency domain approach the results are on average 20-30% and 2-15% below, for the case of buffeting and self-excited forces, respectively. For the vertical RMS displacement, the values are on average 30% below, with an exception when the wind speed of 45 m/s is considered. In this case, the difference becomes 30% for the frequency and 20% for the time domain. The results indicate that by using the large deformation option on the time domain analysis, the displacements at high wind speed are closer to those ones predicted under the BLWTL. A sensitivity analysis conducted on the decay parameter indicates that the exponential decay coefficients of the coherence could significantly influence the calculated RMS values, particularly for the case of vertical displacements.

Key words: Stationary processes, non-homogeneous wind, Boundary Layer Wind Tunnel Laboratory, buffeting forces, self-excited forces, gust wind.

Summary for Lay Audience

The scaled model of a bridge is often tested on the Wind tunnel facility. A full bridge scaled model of a major bridge in Mexico was tested at the wind tunnel laboratory at the University of Western Ontario, Canada. The modelling and analysis of the Baluarte Bridge subjected to wind loading is investigated. The analysis of the numerical model is carried out on the frequency and time domain approaches. For the frequency domain, the energy content of the wind is characterized by a series of harmonic analyses. For the time domain analysis, synthetic time histories of the wind fluctuations are generated. In both cases, an inhomogeneous wind field is generated. The energy of the wind is modelled by the spectrum, and appropriate coherence functions. Apart from the formulation of an inhomogeneous wind, the simulation of non-stationary fluctuating winds at multiple points is also considered.

Both, the frequency and the time domain analysis are used to evaluate the responses of the bridge due to the fluctuating horizontal and vertical wind. For the time domain, in the case of fluctuating lateral displacement, the results are almost identical to those from the Wind tunnel. In contrast, on the frequency domain the results are 20-30% and 2-15% below, for fluctuating wind alone, and for fluctuating wind and self-excited forces, respectively. In the case of the vertical fluctuating wind, the displacements of the numerical model are on average 30% below those from the experimental tests. However, by considering a wind speed of 45 m/s, the difference becomes 30% for the frequency and 20% for the time domain analysis. The results indicate that by using the large deformation option on the time domain analysis the displacements at high wind speed are closer to the experimental results. A sensitivity analysis conducted on the decay parameter indicates that the exponential decay coefficients of the coherence could significantly influence the calculated displacement, particularly in the case of vertical fluctuating wind.

Key words: Wind tunnel facility, full bridge scaled model, numerical model, experimental model, inhomogeneous wind

Co-Authorship Statement

The materials presented in this thesis are based on two joint-authored manuscripts.

Chapter 2 is co-authored with H.P. Hong with assistance from S.C. Yang for the finite element modeling.

Chapter 3 is co-authored with H.P. Hong with assistance from Cui X.Z. and Xiao. M.Y. to validate the simulated wind time histories.

Acknowledgments

I would like to express my gratitude and appreciation to my supervisor for his guidance throughout the Thesis. Although the work presented many obstacles, his attitude towards me and the investigation was always ethical, and professional. Dr. Han-Ping Hong was always supportive and encouraging throughout my stay at the University of Western Ontario. His dedication, commitment, and passion for research are very inspirational. Special mention is given to the co-tutorship given by Dr. Wenxing Zhou, who was present in the different meetings throughout the evolution of the work. Shucheng-Yang also gave valuable assistance for implementing the wind processes into the Finite Element model. I also like to acknowledge the support of Ruth Martin, Kamran Siddiqui, and Ayman El Ansari.

My gratitude goes for two members of the Institute of Engineering (II), from the National Autonomous University of Mexico (UNAM). First, I would like to thank Dr. Roberto Gómez Martínez who encourage my coming to Canada for pursuing a Ph.D. in Wind Engineering. Second, I would like to thank Dr. Adrián Pozos Estrada who also gave me valuable external advice and suggestions. Not only do I acknowledge his professional integrity, but also his kind and generous attitude.

The National Council on Science and Technology (CONACyT-FiideM) from México, and The Graduate Program in Civil and Environmental Engineering throughout the MERCURY Financial Support Packages are gratefully appreciated. Thanks is given to these two institutions that are encouraging and supporting science and research for international students.

At last, but not least, I would like to thank my parents and my family for all their support and encouragement. The term family in this context is not referred exclusively to blood ties, but also to people sharing our lives based on common interests, love and appreciation.

Table of Contents

Abstract	ii
Summary for Lay Audience	iii
Co-Authorship Statement	iv
Acknowledgments	v
Table of Contents	vi
List of Tables	viii
List of Figures	x
List of Appendices	xiii
List of symbols and abbreviations	xiv
Introduction	1
1.1 Introduction and background.....	1
1.2 Wind force modeling	9
1.3 Modelling of fluctuating wind speed	14
1.4 Some studies of wind loading on bridges and boundary layer wind tunnel tests ..	17
1.5 Computational fluid dynamics (CFD) in the study of bridges	24
1.1 Objectives and thesis organization.....	28
2 Comparison of Boundary Layer Wind Tunnel Laboratory Test Results and Finite Element Results for Baluarte Bridge	31
2.1 Introduction	31
2.2 General characteristics of the bridge.....	33
2.1 Validation of Finite Element Models based on experimental results from the BLWTL	38
2.1.1 Finite element modelling	38
2.1.2 Simplified FE model and its dynamic characteristics	43
2.2 Procedure to calculate responses to wind load based on the frequency domain approach	47

2.2.1	Basic equations to estimate responses to winds based on random vibration theory	47
2.2.2	Characteristics of wind and Buffeting force	50
2.2.3	Modelling aeroelastic forces and analysis procedure	57
2.3	Numerical analysis results and comparison	61
2.4	Conclusions	67
3	Response of Baluarte bridge subjected to wind loading – an application of the time-domain approach.....	69
3.1	Introduction	69
3.2	Recapitulation of results from the frequency domain approach.....	71
3.3	Modelling and simulation of wind speed field acted on the bridge.....	74
3.3.1	Mean wind profiles at the Baluarte bridge site	74
3.3.2	Characterization of the fluctuating wind field and its simulation	76
3.4	RMS of the responses by considering time-invariant mean wind speed	88
3.4.1	Time history responses at the midspan.....	88
3.4.2	Influence of mean wind speed and the exponential decay coefficients for the coherence on the responses	91
3.5	Conclusions	94
4	Summary, conclusions, and potential future works.....	96
4.1	Summary and conclusions.....	96
4.2	Potential future research works	97
4.2.1	Assessment of time history responses with nonstationary mean winds	98
5	Bibliography.....	101
	Appendix A Preliminary analysis of the deck girder from the Baluarte bridge by CFD	101
	Appendix B Preliminary analysis of the wind hazard for the country of Mexico ...	103
	Curriculum Vitae.....	133

List of Tables

Table 1.1 Previous studies conducted in the past related to the comparison between numerical and full bridge scaled models	6
Table 1.2 Aerodynamic coefficients from the scaled section model (Flamand 2003; King et al. 2010).	20
Table 1.3 Scaling parameters ratios between model and prototype.	23
Table 2.1 Dynamic characteristics of the bridge.....	37
Table 2.2 Aerodynamic coefficients for drag, lift, and moment, and their derivatives with respect to the angle of attack from the scaled section model.....	37
Table 2.3 Parameters considered for developing the FE model of Baluarte Bridge.	39
Table 2.4 Parameters for simplified FE model.	44
Table 2.5 Comparison of the properties of the main span deck.....	46
Table 2.6 Mean response of the bridge considering static wind loading condition.	62
Table 2.7 RMS displacements due to fluctuating wind component.....	65
Table 3.1 Dynamic characteristics of the bridge.....	72
Table 3.2 Mean response of the bridge.....	73
Table 3.3 RMS displacements dues to fluctuating wind component.	73
Table 3.4 Comparison of the RMS horizontal displacements dues to fluctuating wind component.	91
Table 3.5 Comparison of the RMS vertical displacements dues to fluctuating wind component.	91

Table 3.6 Effect of the assigned coherence and turbulence intensity on the estimated RMS responses (sensitivity to the decay coefficient C_w for $C_x = 16$ and $C_y = 10$). 93

Table 3.7 Effect of the assigned coherence and turbulence intensity on the estimated RMS responses (sensitivity to the decay coefficient C_x and C_y for $C_w = 8$)..... 93

List of Figures

Figure 1.1 Illustration of the bridge deck subjected to wind loading.....	10
Figure 1.2 Scaled section model with three ranks of baffles and a 45° inclined cornice (Flamand, 2003).	20
Figure 1.3 Simulation of the ABL for uniform flow and expected site conditions (King et al. 2010).	21
Figure 2.1 Location and photos: a) Geographic location and, b) and c) photos of Baluarte bridge (https://vidamaz.com/2013/11/09/our-first-trip-on-the-durango-mazatlan-highway-and-the-baluarte-bridge/ ; https://www.pinterest.ca/pin/364017582355349438/).	34
Figure 2.2 Elevation view of the bridge (Pozos-Estrada et al. 2016).	35
Figure 2.3 Cross-section of the main span (top plot) and side span deck (bottom plot) (King et al. 2011).	35
Figure 2.4 Test setup in the BLWTL at UWO (King and Kong 2010).	36
Figure 2.5 Isometric view of the (high-resolution model) 3D-FE model of Baluarte Bridge.	40
Figure 2.6 Modelling of the deck of mid-span.	41
Figure 2.7 Identified vibration modes by using the 3D-FE model.	43
Figure 2.8 Schematic of the modelling matrix element.	57
Figure 2.9 PSD functions of the horizontal displacement and vertical displacement at midspan by considering the buffeting effect.	63
Figure 2.10 PSD function of the horizontal displacement and vertical displacement at midspan by considering the aeroelastic and buffeting effect.	64
Figure 2.11 RMS of the horizontal displacement and vertical displacement at midspan for a range of U_{mid} values.	65

Figure 2.12 Influence of turbulence intensity on the RMS of the horizontal displacement and vertical displacement at midspan for a range of U_{mid} values.	66
Figure 3.1 Isometric view of a simplified 3D-FE model of Baluarte Bridge and the four selected vibration modes.....	74
Figure 3.2 Coordinates and the mean wind profile for Baluarte bridge: a) Defined coordinates; b) Horizontal mean wind speed profile, $rU_{x,zdeck}(x) = U_{x,zdeck}(x)/U_{mid}$; and c) Mean wind speed surface.	76
Figure 3.3 Illustration of the typical sampled records at four locations by using SRM.	79
Figure 3.4 Comparison of the average of the PSD function estimated from the sampled records to its target.	79
Figure 3.5 Comparison of the average of the coherence functions estimated from the sampled records to its target.	80
Figure 3.6 Illustration of the typical nonstationary sampled records at four locations by considering nonstationary effects.....	82
Figure 3.7 Illustration of the typical sampled records at four locations by considering nonstationary effects (amplitude modulation and frequency modulation).	85
Figure 3.8 Comparison of the average of the PSD function estimated from the sampled records to its target: a) to d) Comparison at four locations in terms of ζ , e) to h) Comparison at four locations in terms of frequency.	87
Figure 3.9 Comparison of the average of the coherence function estimated from the sampled records to its target in terms of ζ	88
Figure 3.10 Sampled wind at midspan ($x = 250$ m, see Figure 3.2): The first row for $U_{mid} = 30$ m/s, and the second row for $U_{mid} = 40$ m/s.	89
Figure 3.11 Typical horizontal and vertical displacements at the midspan ($x = 250$ m, see Figure 3.2) due to wind load. The displacements are related to their static equilibrium	

position, including the large deformation effect. The first row for $U_{mid} = 30$ m/s, and the second row for $U_{mid} = 40$ m/s..... 90

Figure 3.12 RMS of the horizontal displacement and vertical displacement at midspan for a range of U_{mid} values and comparison of RMS obtained based on time-domain and frequency domain approach. 92

Figure 4.1 Samples nonstationary winds at a few selected locations: a) Mean and fluctuating wind, b) fluctuating horizontal wind, and c) fluctuating vertical wind. 99

Figure 4.2 Calculated time histories of the displacements at midspan: a) horizontal displacement and b) vertical displacement.100

List of Appendices

Appendix A Preliminary analysis of the deck girder from the Baluarte bridge by CFD

Appendix B Preliminary analysis of the wind hazard for the country of Mexico

List of symbols and abbreviations

α	Rotational displacement
$\dot{\alpha}$	Rotational velocity
$\alpha(x)$	Power law coefficient of the power law model for the wind profile, associated to the coordinate x
$\alpha_{Damping}$	Proportionality coefficient for Rayleigh damping
α_e	Effective angle of attack considered for the quasi-steady theory
α_s	Wind angle of attack when the bridge deck is at the equilibrium position, or steady angle of attack
$\beta_{Damping}$	Proportionality coefficient for Rayleigh damping
$\gamma_{\tilde{u},jk}(\zeta)$	Coherency function for along wind
$\gamma_{\tilde{w},jk}(\zeta)$	Coherency function for across wind
Δn	Frequency increment
δ	Thickness of the Boundary Layer within the BLWT tests
ζ	Monin coordinate or reduced frequency, nz/U
η	Coefficient for the dynamic angle of attack that specifies the difference between the stiffness and aerodynamic center
η_p	The peak response
λ_δ	Scale ratio of the boundary layer thickness
λ_ρ	Scale density ratio, ρ_m/ρ_p

λ_{EI}	Scale Elastic stiffness ratio, $\lambda_U^2 \lambda_L^4$
λ_j	Scale mass moment of inertia per unit length ratio, $\lambda_m \lambda_L^2$
λ_L	Scale length ratio, L_m/L_p
λ_m	Scale mass per unit length ratio, $\lambda_\rho \lambda_L^2$
λ_T	Scale time ratio, T_m/T_p
λ_U	Scale velocity ratio, U_m/U_p
μ	Viscosity of the flow
ν_0^+	Zero up-crossing rate
ν_r	Coefficient of variation of the response, σ_r/\bar{r}
ξ_y	Separation length in the y coordinate, $= y_2 - y_1$
ξ_z	Separation length in the z coordinate, $= z_2 - z_1$
ρ	Air density, 1.2929 kg/m^3
σ_0	Constant standard deviation of a stationary process
σ_r	Standard deviation of the response
$\sigma_{\dot{r}}$	Standard deviation of the temporal derivative of the response
σ_u	Standard deviation for along wind $u(t)$, $\sqrt{6}u_*$
σ_w	Standard deviation for vertical wind $w(t)$, $\sqrt{1.67}u_*$
$\tau(t)$	Non-dimensional time, $U(z)t/z$
$\tau'(t)$	Derivative of the non-dimensional time τ
ν	Kinematic viscosity of the flow, μ/ρ

ϕ	Dynamic angle of attack originated from the bridge deck motion
ϕ_l	Independent and uniformly distributed phase angle
ϕ_{qj}	Phase angle
ω	frequency in radians/second
A_m^*	Aerodynamic derivatives associated with the rotational-wind motion
B	Cross sectional width
b	Mid-chord section of a cross section, $b = B/2$
C	Global damping matrix
\bar{C}	Equivalent Raleigh damping
Ca	Cauchy number, $\rho U^2/E$
C_{ae}	Global aeroelastic damping matrix
\bar{C}_{ae}	Equivalent Raleigh aeroelastic damping
C_D	Abbreviation for the Drag Static coefficient, $C_D(\alpha_s)$
C'_D	Abbreviation for $dC_D/d\alpha$
C_L	Abbreviation for the Lift Static coefficient, $C_L(\alpha_s)$
C'_L	Abbreviation for $dC_L/d\alpha$
C_M	Abbreviation for the Moment Static coefficient, $C_M(\alpha_s)$
C'_M	Abbreviation for $dC_M/d\alpha$
$coh()$	coherence function between fluctuating wind speeds

C_w	Exponential decay coefficient for the coherence of vertical or crosswind
C_y	Exponential decay coefficient for the coherence of along-wind in the directions of the y-axis
C_z	Exponential decay coefficient for the coherence of along-wind in the directions of the z-axis
D	Drag buffeting force
$D(f)$	Diagonal matrix from the Cholesky decomposition of $S_{FF}(f)$
D_{ae}	Drag self-excited force
$D_{ae}(t)$	Drag aeroelastic self-excited force as a function of the time-varying load
D_b	Drag buffeting force
$D_b(t)$	Drag buffeting force as a function of the time-varying load
D_s	Time-averaged static drag force
E_b^e	Force coefficients matrix for the Finite Element model
E_u	Euler number, $p/\rho U^2$
f	Frequency in Hertz
f^*	Reduced frequency, $\delta f/U$
$F(\eta_p)$	probability distribution of peak response
F_{ae}	Aeroelastic force
F_b	Buffeting force

F_b^e	Nodal forces for the Finite Element model
$F_b^{e,s}$	Nodal forces in the global coordinate system, for the Finite Element model
f_c	Coriolis frequency or Coriolis parameter
F_D	Drag steady buffeting forces
F_L	Lift steady buffeting forces
F_r	Froude number, $U^2/g\delta$
F_s	Static force
$F_x(t)$	Time history for lateral wind forces
$F_z(t)$	Time history for vertical wind forces
g	Gravitational acceleration
g_p	The peak factor
G_T	Gust factor
h	Vertical displacement
\dot{h}	Vertical velocity of the deck cross section
$H(if)$	Transfer function of the for the bridge system
H_m^*	Aerodynamic derivatives associated with the vertical-wind motion
$\Im()$	Imaginary part of an argument
J_e	Jensen number, δ/z_0

K	Global stiffness matrix
K_{ae}	Global aeroelastic stiffness matrix
L	Lift buffeting forces
$L(f)$	Decomposed matrix of $S_{FF}(n)$, obtained by Cholesky decomposition or eigenvalue decomposition
$L_{\gamma}(f)$	Decomposed matrix of $S_{FF}(f)$, obtained by Choleski decomposition or eigenvalue decomposition
L_{ae}	Lift self-excited force
$L_{ae}(t)$	Lift aeroelastic self-excited force as a function of the time-varying load
L_b	Lift buffeting force
$L_b(t)$	Lift buffeting force as a function of the time-varying load
L_s	Time-averaged static lift force
M	Global mass matrix
M_{ae}	Pitching moment produced by the self-excited force
$M_{ae}(t)$	Pitching moment aeroelastic self-excited force as a function of the time-varying load
M_b	Pitching moment buffeting force
$M_b(t)$	Pitching moment buffeting force as a function of the time-varying load
M_s	Time-averaged static pitching moment force
m_{η}	The mean of the peak response

n	Frequency in Hertz
n_s	Vortex shedding frequency
P	Reference pressure
p	Horizontal displacement
\dot{p}	Lateral velocity
p_i	Midpoint of element i
p_j	Midpoint of element j
P_m^*	Aerodynamic derivatives associated with the along-wind motion
q^e	Fluctuating velocities for the Finite Element model
\bar{r}	Response due to mean wind speed
$\Re()$	Real part of an argument
R_e	Reynolds number, $U\delta/\nu$
r_u	Horizontal mean wind profile along the deck
$S(f)$	One-sided Power spectral density function
$S_0(f)$	Spectral density function for a homogeneous process
$S_u(\zeta)$	The power spectral density of $u(\tau)$
S_{uu}	Cross-spectral density function for along wind
$S_{\tilde{u}}(\zeta)$	The power spectral density of $\tilde{u}(\tau)$
$S_{u,jk}(\zeta)$	Cross PSD (XPSD) function of $u(\tau)$
$S_{\tilde{u},jk}(\zeta)$	Cross PSD (XPSD) function of $\tilde{u}(\tau)$

$S_w(\zeta)$	The power spectral density of $w(\tau)$
S_{ww}	Cross-spectral density function for along wind
$S_{\tilde{w}}(\zeta)$	The power spectral density of $\tilde{w}(\tau)$
$S_{w,jk}(\zeta)$	Cross PSD (XPSD) function of $w(\tau)$
$S_{\tilde{w},jk}(\zeta)$	Cross PSD (XPSD) function of $\tilde{w}(\tau)$
$S_{X_1 X_2}(\omega)$	Cross-spectral density function
$S_{X_1}(z_1, \omega)$	Power Spectral density function of the fluctuating wind speed at height z_1
$S_{X_2}(z_2, \omega)$	Power Spectral density function of the fluctuating wind speed at height z_2
T^e	Coordinate transformation matrix for the Finite Element model
U	Abbreviation for the reference mean wind velocity $U(z)$
U_0	Constant mean wind speed of a stationary process
\bar{U}	Average of the mean wind speed at points p_i and p_j
$\bar{U}_{j,k}$	Weighted average of the mean wind speed at p_j and p_k
U_{mid}	Reference hourly-mean wind speed at mid-span
U_r	Relative wind velocity which considers buffeting and self-excited forces (quasi-steady model)
u	Instantaneous wind fluctuations for horizontal wind
u_0	Stationary process with a mean wind speed U_0
$u(t)$	Instantaneous wind fluctuations for horizontal wind

$\tilde{u}(\tau)$	Definition of normalized instantaneous wind fluctuations for horizontal wind, $u(t)/\sigma(z)$
u_*	Shear friction velocity
w	Instantaneous wind fluctuations for vertical wind
$w(t)$	Instantaneous wind fluctuations for vertical wind
X	Nodal displacement vector
\dot{X}	Nodal velocity vector
\ddot{X}	Nodal acceleration vector
$x(t)$	The sample of a Gaussian stationary process $X(t)$ with one-sided power spectral density function
z	The height above ground surface
z_0	Roughness length, length-scale representation of the roughness of the surface
\bar{z}	Average value of z_i and z_j
$z_{deck}(x)$	reference deck height associated to the coordinate x

APPENDIX A

α	Scale parameter
ξ	Shape parameter for the GEV distribution
$D_{crit,\alpha}$	The critical value at $1-\alpha$ level, for the Kolmogorov-Smirnov test
$F(x_m)$	Estimated value of for each ranked annual maximum
$F_X(x)$	Cumulative distribution function
$J(x)$	Jacobian matrix from the Newton-Raphson method
N	Total number of observations
m	Ranked value
P_i	Ranked observed annual maxima
$s(x)$	Merit function
T_r	Return period
u	Location parameter or mode of the distribution
U_z	Wind velocity at a height z
y	Reduced variate for the Gumbel distribution
z_0	Roughness length, length-scale representation of the roughness of the surface

ABBREVIATIONS

ABL	Atmospheric boundary layer
BLWT	Boundary Layer Wind Tunnel
c.d.f.	Cumulative distribution function
CFD	Computational fluid dynamics
CSTB	Centre Scientifique et Technique du Batiment, in French
CWE	Computational Wind Engineering
FE	Finite element
GEV	General extreme value
p.d.f.	Probability density function
PSD	Power spectral density
PWM	Probability weighted moments
LSM	Least square method
MLM	Method of L-moments
MML	Method of maximum likelihood
MOM	Method of moments
UNAM	Universidad Nacional Autónoma de Mexico, in Spanish
XPSD	Cross Power spectral density

Chapter 1

Introduction

1.1 Introduction and background

For the study of the aerodynamic response of long-span bridges, it is of paramount importance the relation between numerical and experimental modeling. The numerical model is carried out by means of a Finite Element (FE) model in the case of the structural model, while in the case of characterizing wind forces is studied in terms of stochastic processes. The numerical or analytical model is generally calibrated with the aid of experimental data obtained from boundary layer wind tunnel laboratory (BLWTL). The test models are classified as a full-bridge aeroelastic model, scaled section model, and taut-strip model. The purpose of the scaled model is to test the aerodynamic performance of the deck cross section, or to modify the original design to improve its aerodynamic performance. A taut-strip model is a simplification of the full aerodynamic model with the objective of matching the dynamic characteristics of the bridge. For this type of model, the main degrees of freedom are set up by springs that are adjusted to give the correct frequencies of the section under study (Scanlan, 1983). The study of the spatial structure of the wind, which is related to the wind coherence or the force coherence can easily be implemented into this type of model. Besides, the taut-strip models also allow different sinusoidal mode shapes to participate in the gust wind response (Larsen, 1993). On the other hand, the third type of modelling, which is the full-bridge aerodynamic model, allows a complete assessment of the bridge performance in relation to the spatio temporal gusty wind.

In 1965 one of the first boundary layer wind tunnels laboratory (BLWTL) in the world was constructed by Alan G. Davenport (1967) and associates, at The University of Western Ontario, Canada. Subsequently, many of the world's tallest buildings and longest span bridges were tested in this facility. A robust description of the fundamental principles that exist between a scaled model under the wind tunnel and its corresponding prototype is given by Wardlaw (1980):

“Model scale observations can only be extrapolated with confidence to prototype scale if sound scaling principles have been applied in the design of the model and the experiment. This will ensure that the relative magnitudes of the various forces involved in the bridge dynamics -the gravitational, inertial, aerodynamic, elastic, and structural damping forces- will be the same for the model and the prototype and that the motion amplitudes will be in the same proportion as the geometric scale ratio. As will be shown, the scaling of different physical variables will not always be compatible and judicious relaxations of one or more of the dimensionless scaling parameters will be required after careful examination of their relative importance in the behavior of the bridge.”

In a preliminary stage, under the study of buffeting forces, nondimensional aerodynamic coefficients are obtained from section model studies. These coefficients are used to translate nondimensional forces into the model, and to assess the stress levels. The aerodynamic forces under study are generally divided into static, self-excited, and buffeting forces. The description of the static component is based on the mean time average wind load component.

Self-excited and buffeting forces are related to the interaction between structure and wind, and to the gust wind component, respectively. These two dynamic components of the load are separated on the bases of linearized theory. The linearization is valid below the onset of flutter instability, where displacements are assumed to be small. Admittance functions represent the transfer function between the gust wind component and the buffeting forces. Flutter derivatives, on the other hand, represent the transfer function between the gust wind component and the self excited forces.

Generally, admittance functions and flutter derivatives are measured on the section model studied under the Wind tunnel. Both functions undermine the possibility that wind loads for buffeting and self-excited forces are not necessarily quasi-steady. To consider the temporal and spatial variation of aerodynamic forces, Davenport (1962) introduced the concept of aerodynamic admittance function and joint acceptance function in the study of line-like structures. This type of structures are extended longitudinally in one direction, while the cross section dimensions are relatively small (ex. Bridges and transmission lines).

The self-excited forces and the problem of flutter instability on bridges were first presented by Scanlan and Tomoko, (1971). The aerodynamic performances of several bridges, including the standard airfoil case and the Tacoma Narrows bridge cross section were investigated based on this approach.

A standard methodology within the study of aerodynamic forces on cable-stayed bridges is to obtain under the mean wind loading the deformation of the bridge, and to perform with the deformed configuration a linearization of the aerodynamic forces around the steady equilibrium position. The influence of the steady deformation on the Bosphorus suspension bridge, due to the mean wind component on the critical wind velocity is studied by Salvatori and Spinelli (2007). In this study a linearization around the reference configuration, which is the cross section of the bridge before applying the steady load, and around the steady deformed configuration are evaluated and compared. The steady deformed configuration tends to alter the bridge aerodynamics when compared to the reference configuration.

In the study of analytical models on bridges, different theoretical models can be considered that are originated from the underlying physical assumptions made during the modelling process. A category theory-based modelling approach is presented by Kavrakov et al. (2019) between a diverse set of models for the study of bridge aerodynamics. A simplified form of aerodynamic forces is considered by any of the theoretical approaches presented by Kavrakov and associates, which can account or neglect certain physical phenomena based on different assumptions. For example, any of the theoretical models can consider or not the aerodynamic nonlinearity, the fading fluid memory, or the aerodynamic coupling. The aerodynamic nonlinearity is associated to the use of unsteady models and the use of flutter derivatives; the fading fluid memory relates unsteady models on the time domain via the use of indicial functions. Aerodynamic coupling, on the other hand refers to the coupling between different modes.

The main analytical model considered in this investigation is the quasi-steady model. One of the main drawbacks of this particular model is that it ignores frequency dependent characteristics in the modeling of aerodynamic forces. When considering the quasi-steady

model, the admittance functions are taken as one, and self-excited forces are qualitatively approximated via steady coefficients. The quasi-steady model represents a simplification of the aeroelastic problem. In this case, the estimation of the fluid-structure interaction is based on information extracted from the study of the steady coefficients. Even though, the quasi-steady model considers nonlinearities in the aerodynamic forces, it disregards the unsteady fluid memory effect that is characteristic of the unsteady model. Functional relationships that exist between the quasi-steady model and the unsteady model are discussed by Chen and Kareem (2002).

In contrast to the unsteady model, the quasi-steady model is valid for small values of the reduced frequency. Besides, another important feature of this type of model is that it can only be used when the disturbance in the flow has appreciably larger dimensions compared to the deck. A study of the quasi-steady approach with emphasis on the self-excited forces is presented by Chen et al. (2009). In this study decay coefficients of coherence functions from buffeting forces are obtained from the experimental model of the Xiaoguan bridge. This study suggests that wind analysis based on the coherence of wind turbulence may considerably underestimate the buffeting response when compared to the actual experimentally measured force coherence. Similar findings are also found in Larose and Mann (1998), who actually study more carefully the span-wise coherence of buffeting forces.

When unsteady models are used, frequency-dependent characteristics are incorporated into the theoretical model. In the case of buffeting forces, the frequency-dependent characteristics are introduced via admittance and the by the use of the joint acceptance function. Conversely, frequency-dependent characteristics for self-excited forces are introduced via experimentally quantified flutter derivatives. For the case of unsteady models, the fluid memory effect generates a frequency-dependent attenuation and a phase delay in the aerodynamic forces. When considering the problem in the time domain, indicial or rational functions are fitted based on experimentally obtained flutter derivatives.

By the use of convolution integrals and rational function approximations, Chen et al. (2000a) studied the effect of coupled flutter and buffeting response on a bridge. The

unsteadiness from self-excited forces is mapped from experimentally measured flutter derivatives by means of rational functions. Similarly, the unsteadiness of buffeting forces is mapped from experimentally measured aerodynamic admittance functions and spanwise coherence. For very long-span bridges, unsteady characteristics of wind forces and aerodynamic coupling can have a significant influence on the bridge response, and in the assessment of the bridge aerodynamics. Chen et al. (2000a) studied a bridge of 2000 meters and emphasizes the importance of unsteady characteristics derived from experimentally measured spanwise coherence of aerodynamic forces. Chen et al. (2009), found that the pressure field throughout the bridge deck has a higher spanwise correlation to that one of the wind field which is considered under the strip assumption. Similar observations are found in the work of Larose and Mann (1998). In this case, it is possible that the strip assumption, can possibly underestimate the gust wind response.

The strip assumption establishes that the spatial distribution of the wind fluctuations can be taken as representative of the spatial distribution of the force loading produced by buffeting (Larose, 1998). In Jakobsen et al. (1997), the span-wise correlation of buffeting lift and overturning moment on a bridge box-girder is estimated based on surface pressure measurements under the wind tunnel. The span-wise structure of buffeting forces, again is found to be considerably stronger than the structure of the oncoming turbulence. A similar study on cylinders with flat hexagonal and rectangular cross sections is presented by Kimura et al. (1997). This study also indicates that the cross-correlation of pressures is significantly greater than the correlation of the incident turbulence. Sankaran and Jancauskas, (1993) found that an increase in both turbulence intensity and length scale produces a significant increase in cross-correlation and coherence. When considering more recent studies, Li et al. (2018) suggest that the ratio of characteristic lengths of structures to the integral length scales of turbulence has a significant impact in the study of the spanwise coherence.

The comparison of analytical and experimental modeling are indispensable in the study of aerodynamic forces on bridges. An extensive literature concerned with this topic has been generated over the last years. However, the comparison of the numerical model and the full bridge scaled model are very scarce. One of the first of this type of studies is

presented by Larose et al. (1992). In this case, the consistency of the experimental results from the BLWTL are verified in relation to a theoretical model based on the quasi-steady aerodynamic approach. The theoretical prediction for the lateral RMS is consistent with experimental results in the case of the Humber bridge, with a more conservative predictions for a high reduced velocity. A similar work of this kind is presented by Larsen, (1993) for the Great-Belt East bridges. In this last study, the peak lateral response obtained from the numerical model result in a lower displacement when compared to the experimental model under the full bridge scaled model.

The full bridge aeroelastic model of the Stonecutters bridge is studied by Hui and Yau, (2010) by means of a 3-D finite element model. Hui and Yau improved the traditional approach based on wind coherences, and instead made use of the coherence of wind pressures. Another study related to the comparison between numerical and experimental model for the Akashi-Kaikyo bridge is presented by Boonyapinyo, (1999).

All of the main contributions of the comparison between a numerical and of a full bridge scaled model are presented in Table 1.1, for easy of reference. Besides, in the following a brief description of the work of Diana et al. (1995), which is considered at the time the more complete study related to this topic, is presented.

Table 1.1 Previous studies conducted in the past related to the comparison between numerical and full bridge scaled models

Name of the bridge	Authors of the study	year	Scale	Compared response
Humber bridge, England	G.L. Larose, A.G. Davenport and J.P.C. King	1992	1:175	RMS of displacements and accelerations
The Great Belt East bridge, Denmark	A. Larsen	1993	1:200	The peak lateral response
Stretto di Messina suspension bridge, Italy	G. Diana, M. Falco, S. Bruni, A. Cigada, G.L. Larose, A. Damsgaard and A. Collina	1995	1:250	Comparision of a torsional mode

The Akashi Kaikyo bridges, Japan	V. Boonyapinyo, T. Miyata and H. Yamada	1999	1:100	horizontal and torsional buffeting responses
The Stonecutters bridge, Hong Kong	M.C.H. Hui and D.M.S. Yau	2010	1:200	Spatial correlation of buffeting forces

The most important study conducted in the past related to the comparison between numerical and the full bridge scaled model is the one of Diana et al. (1995), on the Strait of Messina bridge, located in Italy. This study was conducted under a full bridge aeroelastic model at the Martin Jensen Wind tunnel, on a 1:250 scale. The FE model and the theoretical model of wind forces were developed by Politecnico de Milano (Falco et al. 1992). The implemented theoretical model in this case is based on a quasi-steady corrected theory, which differentiates between a low and a high frequency component of the turbulence. For the quasi-steady corrected theory, flutter derivatives are considered for a zero-incidence case and for a variation of the incident angle of attack, for the range of high frequencies. This same numerical modeling was also considered by Diana et al. (1992) for the study of the Humber bridge in the United Kingdom.

The study of modal coupling on the Akashi-Kaikyo bridge is presented by Katsuchi et al. (1998). This Akashi-Kaikyo bridge has a central span of 1,991 m, which makes the bridge very susceptible to wind forces. In this particular case, when the wind speed increases, the coupling effects on the multimode calculation become significant. The effect of aerodynamic coupling is also investigated by Chen et al.(2000b). Chen and associates pointed out that for long-span suspension bridges, the vertical and torsional motions are likely to be coupled at high wind speeds. Conversely, Jain et al. (1996) studied the behavior of a cable-stayed bridge with a central main span of 430 m. In this case, the model presents well-separated frequencies, and the adequacy of the single-mode procedures is adequate for the analysis.

The characterization of aerodynamic forces can be considered on the frequency domain or time domain approach. In the frequency domain, the characterization of the stochastic

process is presented in terms of the power spectral density function (PSDF). The PSDF characterizes the energy content of the gust wind throughout different ranges of frequencies. In contrast, the time-domain approach requires the simulation of the fluctuating wind component as a time history based on the stochastic characterization of the wind. Frequency domain analysis is based on a linear hypothesis, where the evaluation of the response can be considered by numerically integrating the product of the bridge's transfer function and the wind load spectra (Yang et al. 1997). For the frequency domain approach, Sun et al. (1999) uses a finite element approach and a pseudo excitation method for the characterization of wind forces. For the pseudo-excitation method, aeroelastic forces on a bridge deck are changed into nodal forces to form aeroelastic damping and stiffness matrices, while aerodynamic forces are converted into nodal forces and assigned to the deck, towers, and cables. As mentioned previously, the use of unsteady models in the frequency domain approach facilitates the modeling of frequency dependent characteristics considered for unsteady aerodynamic forces, via experimentally measured flutter derivatives. Nevertheless, this type of approach is constrained by the assumptions of linearity in structural dynamics, aerodynamics, and stationarity of wind fluctuations (Chen and Kareem, 2003).

Several methods for synthesizing homogeneous random fields based on the second-order statistics are discussed in Spanos and Zeldin (1998). Two of the more used methods for simulating sample functions on the time domain are the auto-regressive moving average (ARMA) method (Kareem, 2008; Di Paola, 1998) and the spectral representation method (SRM) (Shinozuka, 1972). The SRM is a well-known method for digital simulation in engineering that made use of the superposition of trigonometric functions and the use of a random phase angle. An improvement in the computational efficiency of the SRM by using the fast Fourier transform (FFT) was developed in previous studies (Yang, 1972; Witting & Sinha, 1975). Another modification to the SRM was made by Cao et al, (2000), who expressed the Cholesky decomposition of the cross-spectral density matrix in algebraic formulas. However, the improvement is only valid for an homogeneous process simulated at equidistant points.

A historical perspective of the different types of simulation, for the inflow conditions is summarised in Kareem, (2008), which includes Non-stationary, non-homogeneous processes, non-Gaussian simulation, and conditional simulation of Gaussian processes. The inhomogeneity of the wind is an important aspect of the characterization of wind processes throughout the study of the Baluarte bridge. The non-homogeneous wind is produced by the canyon. In this case, compression on the wind flow is produced when the flow cross throughout the canyon, generating disturbances that accelerate the intensities of the pressures on the main girder in an inhomogeneous manner.

1.2 Wind force modeling

The wind is usually decomposed as mean wind component and fluctuating wind component (Simiu and Scanlan 1996). The wind force acted on bridges may be classified as (Salvatori and Borri 2007):

- a) mean wind velocity dependent steady load,
- b) fluctuating wind dependent buffeting load, and
- c) aeroelastic self-excited load which depends on the motion of the cross-section.

The mean wind velocity dependent load is treated as a static load. The studies given by Davenport (1962) provided the theoretical framework to evaluate the buffeting force and the structural responses to buffeting force based on the gust factor approach. The study of Davenport (1962) and Scanlan (1978) also provided the basis for the frequency domain approach to evaluate the bridge response subjected to wind load. Consider as a particular case the bridge deck cross-section shown in Figure 1.1, which is subjected to the wind field. In the figure, U represents the (along wind) mean wind velocity, u and w are the fluctuating winds in the alongwind and crosswind directions. \dot{p} and \dot{h} are the lateral and vertical velocities of the deck cross section.

$$\phi = \tan^{-1} \left(\frac{w + \dot{h} + \eta B \dot{\alpha}}{U + u - \dot{p}} \right), \quad (1.2)$$

The drag and lift forces are given by,

$$D_s = \frac{1}{2} \rho U_r^2 B C_D(\alpha_e), \quad (1.3a)$$

and,

$$L_s = \frac{1}{2} \rho U_r^2 B C_L(\alpha_e), \quad (1.3b)$$

in which ρ is the air density, B a characteristic length (i.e., section width), and the wind velocity of the quasi-steady model, or relative velocity U_r , is given by,

$$U_r = \sqrt{(U + u - \dot{p})^2 + (w + \dot{h} + \eta B \dot{\alpha})^2} \quad (1.4)$$

where η is the coefficient for the dynamic angle of attack that specifies the difference between the center of stiffness and aerodynamic center in the case of self-excited forces.

By assuming that the instantaneous effective angle of incidence is small, and if the use of the linearized forces (Simiu and Scanlan 1996; Chen and Kareem 2002; Strømmen 2010) is adequate, the drag force, lift force, and torsional moment, denoted as D , L , and M acted on the bridge deck can be expressed as,

$$D_b = \frac{1}{2} \rho U^2 B \left[C_D + 2C_D \frac{u}{U} + C'_D \frac{w}{U} \right] \quad (1.5a)$$

$$L_b = \frac{1}{2} \rho U^2 B \left[C_L + 2C_L \frac{u}{U} + (C'_L + C_D) \frac{w}{U} \right] \quad (1.5b)$$

and,

$$M_b = \frac{1}{2} \rho U^2 B^2 \left[C_M + 2C_M \frac{u}{U} + C'_M \frac{w}{U} \right] \quad (1.5c)$$

where $C_D = C_D(\alpha_s)$, $C_L = C_L(\alpha_s)$ and $C_M = C_M(\alpha_s)$ are the steady coefficients as a function of the steady angle of attack α_s , and the prime assigned to the steady coefficients

is the abbreviation for $dC_D/d\alpha$, $dC_L/d\alpha$ and $dC_M/d\alpha$, respectively. Further, ρ is the density of the air, U the abbreviation for the reference mean wind velocity $U(z)$, u the longitudinal gust wind, and w the vertical gust wind component. The first component in Eqs. (1.5a) to (1.5c) forms the static force while the remaining components represent the buffeting forces. Note that the use of the frequency domain approach was considered in Sun et al. (1999) for analyzing bridges, where the calculation of the power spectral density of the responses is based on the so-called pseudo-excitation method. In the pseudo-excitation method, the loading spectrum is decomposed by applying eigenvalue decomposition and use as the basis to define the non-homogeneous loads for an array of selected frequencies. The obtained responses are then used to obtain the power spectrum of the responses. This method will be explained in detail and used to calculate the response of the Baluarte bridge based on the frequency domain approach.

The characterization of the aeroelastic self-excited forces is more completed than characterizing the mean wind and buffeting forces. Salvatori and Borri (2007) considered that aeroelastic self-excited forces could be classified as quasi-steady self-excited forces, unsteady self-excited forces in the frequency domain, and unsteady self-excited forces in the time-domain through indicial functions. In the case of indicial functions, aerodynamic forces have a rise in time and attain their quasi-steady value asymptotically. This type of model, on the time domain allows structural nonlinearities. However, nonlinearity on the wind load is not considered, since indicial functions are obtained from flutter derivatives, and flutter derivatives are obtained based on a linearized theory (Salvatori and Spinelli, 2007). In contrast, the quasi-steady formulation can consider nonlinearities in the aerodynamic forces related to the incidence angle of the wind. However, the quasi-steady theory discards the unsteady fluid memory effect.

The derivation of the quasi-steady load model is similar to the case of deriving the buffeting forces, except that it considers that the wind forces are affected by the motion of the bridge deck (Miyata et al. 1995; Salvatori and Borri 2007). In this case, the wind forces (D , L , and M) (i.e., including the mean, buffeting, and quasi-steady force) can be written as,

$$D_{ae} = \frac{1}{2} \rho U^2 B \left[C_D + 2C_D \frac{u}{U} + C'_D \frac{w}{U} + (C'_L + C_D) \frac{\dot{h} + \eta B \dot{\alpha}}{U} + C'_D \alpha + 2C_D \frac{\dot{p}}{U} \right] \quad (1.6a)$$

$$L_{ae} = \frac{1}{2} \rho U^2 B \left[C_L + 2C_L \frac{u}{U} + (C'_L + C_D) \frac{w}{U} + (C'_L + C_D) \frac{\dot{h} + \eta B \dot{\alpha}}{U} + C'_L \alpha + 2C_L \frac{\dot{p}}{U} \right] \quad (1.6b)$$

and,

$$M_{ae} = \frac{1}{2} \rho U^2 B^2 \left[C_M + 2C_M \frac{u}{U} + C'_M \frac{w}{U} + C'_M \frac{\dot{h} + \eta B \dot{\alpha}}{U} + C'_M \alpha + 2C_M \frac{\dot{p}}{U} \right] \quad (1.6c)$$

where a dot over p , h , and α (which denote the horizontal displacement, vertical displacement, and rotation) represent their derivatives with respect to time.

The unsteady self-excited forces in the frequency domain were introduced by Scanlan and Tomko (1971). In this case, Scanlan and Tomoko (1971), further extended to include the along wind forces and displacements, as:

$$D_{ae} = \frac{1}{2} \rho U^2 B \left[kP_1^* \frac{\dot{p}}{U} + kP_2^* \frac{B\dot{\alpha}}{U} + k^2 P_3^* \alpha + k^2 P_4^* \frac{p}{B} - kP_5^* \frac{\dot{h}}{U} - k^2 P_6^* \frac{h}{B} \right] \quad (1.7a)$$

$$L_{ae} = \frac{1}{2} \rho U^2 B \left[kH_1^* \frac{\dot{h}}{U} - kH_2^* \frac{B\dot{\alpha}}{U} - k^2 H_3^* \alpha + k^2 H_4^* \frac{h}{B} - kH_5^* \frac{\dot{p}}{U} - k^2 H_6^* \frac{p}{B} \right] \quad (1.7b)$$

$$M_{ae} = \frac{1}{2} \rho U^2 B^2 \left[-kA_1^* \frac{\dot{h}}{U} + kA_2^* \frac{B\dot{\alpha}}{U} + k^2 A_3^* \alpha + k^2 A_4^* \frac{h}{B} + kA_5^* \frac{\dot{p}}{U} + k^2 A_6^* \frac{p}{B} \right] \quad (1.7c)$$

where $k(= \omega B/U)$ is the reduced frequency; P_m^* , H_m^* , and A_m^* , ($m=1, \dots, 6$) are the aeroelastic derivatives, and the subscript ae to D , L , and M is used to indicate that these quantities are aeroelastic forces to be included as part of the drag force, lift force, and torsional moment. The derivation of these equations was elaborated in Salvatori and Borri (2007) and Karvrakov et al. (2019).

Instead of presenting the aeroelastic forces in terms of aerodynamic derivatives, Scanlan et al. (1974) introduce the concept of indicial aerodynamic functions for bridge decks. The studies of Scanlan et al. (1974), Chen et al. (2000a, b), and Salvatori and Borri (2007) indicated that it is advantageous to use the indicial aerodynamic functions in carrying out the responses of the bridge to wind load based on the state-space formulation.

The estimation of the indicial function from experimental procedures was discussed in Caracoglia and Jones (2003).

It should be noted that in the frequency approach, it is often assumed that the fluctuating wind component is a stationary Gaussian process. The consideration of the nonstationary or non-Gaussian process complicates the analysis in the frequency domain. In such a case, the analysis could be carried out in the time domain, which involves the simulation of the fluctuating winds and analysis of the structural response using the time history method. A short description of the stochastic process and the simulation of the stochastic process is presented in the following section.

1.3 Modelling of fluctuating wind speed

The wind speed is frequently decomposed into the mean and fluctuating wind component. Winds can be treated as stationary or as nonstationary. Since the fluctuating winds vary in time in a random manner, it is generally modeled as a stochastic process with the assumption that the fluctuating wind speed is a stationary Gaussian process (Simiu and Scanlan 1996). A Gaussian process could be viewed as a generalization or extension of a multivariate normally distributed random variable. The marginal probability of the Gaussian process is a normal distribution. The use of the stochastic process as the input to a dynamic system for estimating the structural response and structural reliability can be found in Madsen et al. (2006).

A stationary process can be characterized by the power spectral density (PSD) function, which can be estimated based on the samples of the stochastic process and Fourier amplitude spectrum (Newland 2012). Given the PSD function of a stationary process, the samples of the process can be simulated by applying the very popular spectral representation method (SRM) (Shinozuka and Jan 1972). According to the SRM, the sample of a Gaussian stationary process $X(t)$ with one-sided power spectral density function $S(n)$, can be sampled using,

$$x(t) = \sqrt{2} \sum_{l=1}^{N/2+1} \sqrt{S((l-1)\Delta f)\Delta f} \cos(2\pi((l-1)\Delta f)t + \phi_l), \quad (1.8)$$

where ϕ_l is an independent and uniformly distributed phase angle, distributed between 0 and 2π , and Δf is a considered frequency increment.

The multivariate stationary processes can be characterized by the non-crossed or crossed PSD function:

$$S_{X_1 X_2}(\omega) = \sqrt{S_{X_1}(z_1, \omega) S_{X_2}(z_2, \omega)} \text{coh}(z_1, y_1, \xi_z, \xi_y, \omega) \quad (1.9)$$

where $\xi_z = z_2 - z_1$ and $\xi_y = y_2 - y_1$; S_{X_1} and S_{X_2} are the PSD of the fluctuating wind speed at height z_1 and z_2 ; $\text{coh}()$ is the coherence function between fluctuating wind speeds. If S_{X_1} , S_{X_2} and the coherence are independent of their coordinates, the spectrum and the coherence are simplified, and the cross power spectral density (C-PSD) function, corresponds now to the case of homogeneous stationary random processes,

$$S_{X_1 X_2}(\omega) = S_0(\omega) \text{coh}(\xi_z, \xi_y, \omega) \quad (1.10)$$

where $S_0(\omega)$, is a homogeneous stationary Power Spectral Density (PSD) function.

Note that several generalizations of the SRM are given in the literature, including simulating the vector of evolutionary processes (Shinozuka and Deodatis 1996), where the evolutionary spectrum is defined by Priestley (1965). It can also be used to simulate the sum of several evolutionary processes (e.g., Shinozuka and Deodatis 1996; Huang and Chen 2009). It was also extended to simulate the nonstationary non-Gaussian process in several studies, including Shields and Deodatis (2013).

Rather than considering the fluctuating wind as an evolutionary process, based on the observation that the commonly used power spectral density function of fluctuating wind depends on the mean wind speed, Hong (2016) proposed the use of the amplitude modulated and frequency modulated process to model the fluctuating winds with a time-varying mean, or to model a vector of winds, each with a different mean wind speed. In such a case, the use of the time transformation concept (Yeh and Wen 1990) is employed. Other methods for simulating the stationary and nonstationary processes are also available.

The interested readers are referred to Phoon et al. (2002); Ghanem and Spanos (2003); Spanos and Zeldin (1998); and Shield and Kim (2017).

Note that, by using the simulated fluctuating winds, the responses of a bridge subjected to wind load that is formulated based on quasi-steady theory was presented in Chen et al. (2009) by using the simulated vector of fluctuating winds. For their analysis, a finite element model was developed to represent the full bridge. Since, once the quasi-steady theory is adopted, the finite element model is independent of whether the wind field is nonstationary or non-Gaussian or inhomogeneous. Therefore, this time domain analysis is very practical and relatively simple to use. It is adopted in Chapter 3 to evaluate the response of the Baluarte bridge to the wind load based on the time domain approach.

In the case of non-stationary random processes, the concept of a spectral density function differs quite significantly from the case of stationary processes. In this case, Priestly (1966), gives a legitimate description of a time-variant frequency content by means of the evolutionary power spectral density (EPSD) function. With the aid of the Evolutionary spectrum is possible to study processes with continuously changing spectral patterns in time, with the only requisite of using slowly varying functions. The Non-stationarity aspect of wind forces represents a challenging problem within the study of random processes. Non-stationary events such as hurricanes and thunderstorms are in constant flux and are very difficult to be measured. Chen and Letchford, (2007) presented a model for the characterization of non-stationary thunderstorm downburst wind fields. The fluctuating wind is modeled as a uniformly modulated evolutionary vector process, which is generated by modulation of the amplitude of a stationary Gaussian process. Chay et al. (2006) also used the concept of amplitude modulation, but instead of the SRM they applied the autoregressive moving average (ARMA) technique for the simulation. In certain cases, not only the amplitude presents a challenge for the study of non-stationary processes, but also the frequency modulation needs to be included in the analysis. Yeh and Wen (1990) showed that the time-varying frequency content has a significant impact on the response of structures. The model proposed by Ye and Wen is a modification of the amplitude and frequency modulated random processes originally proposed by Grigoriu et al. (1988). The concept of amplitude and frequency modulation has been applied in wind

engineering for the simulation of nonstationary fluctuating winds at multiple points, which are best represented by AM/FM processes (Hong, 2016).

1.4 Some studies of wind loading on bridges and boundary layer wind tunnel tests

A well-known example of bridge failure is the collapse of the 1940 Tacoma narrow bridge - a suspension bridge in the U.S. states that spanned the Tacoma Narrows strait of Puget Sound between Tacoma and the Kitsap Peninsula (Amman et al. 1941; Billah and Scanlan 1991). Footage of the failure can be found on the YouTube website (e.g., <https://www.youtube.com/watch?v=j-zczJXSxnw>, <https://www.youtube.com/watch?v=KogpyCUecLk>, Access July 8, 2021). For the design of long bridges, often model tests are carried out in the boundary layer wind tunnel based on a scaled model of the bridges, to find several coefficients that are required to evaluate the wind forces and effects acted on the bridges. The test could be done for a section model (i.e., rigid model of the bridge deck), or an aeroelastic model, including topographic effect.

The wind test was originally used for the aeronautical industry. It could be an open-circuit type where the air is drawn into the tunnel from the external environment at the inlet and discharged at the outlet. It could also be a closed-circuit type, where the air is circulating within the tunnel. The open-circuit configuration is more convenient to control the flow; the closed-circuit configuration is more suitable for cases where atmospheric pressure is considered important. One of the earlier major wind tunnels used for tall buildings and long bridges was constructed at the University of Western Ontario (Davenport et al. 1985). The development of the boundary layer wind tunnels (BLWTs) for application in civil engineering was presented in Cermak (2003), emphasizing that physical modelling of wind effects requires a properly simulated boundary-layer flow. More sophisticated wind tunnels such as the WindEEE dome at the University of Western Ontario were developed in recent years. This type of facility could be used to simulate the tornado effects on structures (Hangan 2014) (see also <https://www.eng.uwo.ca/windeeee/facilities.html>).

There are numerous tall buildings and bridges that have been tested in the BLWT, at the University of Western Ontario. The test results provide the basis for the design of buildings and bridges subjected to wind loads. In this case an aeroelastic model of a major cable-stayed bridge – Baluarte bridge – that was built in Mexico was tested at the BLWTL at the University of Western Ontario (King and Kong 2010; King et al. 2011). The test includes the topographic effects. A short description of the wind tunnel tests for the Baluarte bridge is presented in this section.

The BLWT test results of bridges served the civil engineering community well in designing such structural systems efficiently. The comparison of the responses from the wind tunnel test to the numerical modelling of the bridges subjected to wind loads is starting to attract the interest of several researchers. For instance, Diana et al. (1995, 2013), provided an overview of the wind tunnel activities and methodologies developed to support the design of long suspension bridges. They called for a synergistic approach in dealing with the design and evaluation of bridges under wind loading by incorporating numerical modelling and wind tunnel experimental methodologies. Prior to the study of Diana, Larose et al. (1992) compared quasi-steady numerical models of the Humber suspension bridge in England, the Farø Bridge in Denmark, and the Sunshine Skyway bridge in the U.S.A. with full-bridge aero-elastic models of each bridge. Another study of this kind is the one of Hui, (2013), where a 1:200 scale full aeroelastic model of the Stonecutters Bridge in Hong Kong, is compared to analytical results. On the study of Hui, M.C.H, buffeting analysis was conducted based on direct measurement of buffeting forces on a section model. Another important study of this kind is the one conducted by Katsuchi et al. (1998) on the Akashi-Kaikyo Bridge. In this case, analytical studies of mode coupling in the flutter and buffeting of the Akashi-Kaikyo Bridge were performed and compared with the behavior of a full bridge scaled model on the wind tunnel.

The evaluation of bridge responses to aerodynamic and aeroelastic effects could be carried out based on the frequency domain approach or time domain approach. These subjects were presented extensively in the literature, including Scanlan and Tomko (1971), Sun et al. (1999); Chen et al. (2000a, b), Chen and Kareem (2002); Salvatori and Borri (2007); Chen et al. (2009), Strømmen (2010). The frequency domain approach requires

the characterization of the fluctuating wind component as a stochastic process using the power spectral density function; the time-domain approach requires the simulation of the fluctuating wind component based on the stochastic characteristics of the fluctuating wind.

Atmospheric motion is primarily the result of complex boundary conditions, such as differences in temperature distributions, non-uniform roughness, topography, and local climatological factors. This complexity of the natural wind often differs from those characteristics associated with the most conventional boundary layers. In most cases, the turbulence structure may be inhomogeneous in planes parallel to the surface. “Because of this strong nonlinear interaction between atmospheric motion and the objects over which flow takes place, engineers have learned to rely more heavily on physical modeling and similarity analysis than on mathematical analysis for a quantitative description of the wind effects” (Cermak 1975).

One fundamental aspect of the wind tunnel which connects experimental and mathematical procedures is the integration of the mean wind pressures, which enables the prediction of the aerodynamic forces (Davenport and Isyumov 1967). The aerodynamic forces are expressed in terms of the static coefficients. Nondimensional aerodynamic coefficients are extracted from sectional tests to test the aerodynamic performance of the deck cross section. Sectional model tests of the Baluarte bridge were conducted at the CSTB (Centre Scientifique et Technique du Batiment, in French) BLWT, in Nantes, France, on July 2003. From the section model studies, fundamental aerodynamic information on the bridge deck was provided. The studies considered the aerodynamic coefficients at a different steady angle of attack (α_s). A 1:50 scale was considered between model/prototype. From these preliminary studies, an improvement in the performance of the main span deck was achieved by adding three ranks of baffles under the bridge deck to suppress the vortex shedding. Another improvement was generated by implementing a 45° cornice throughout 200 meters of length located at the centerline of the main span. The modifications to the main-span deck for the scaled model is presented in Figure 1.2 (Flamand, 2003).

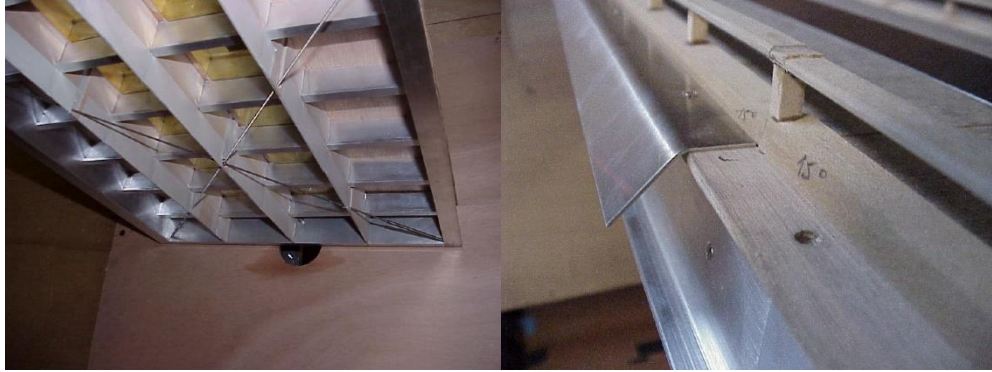


Figure 1.2 Scaled section model with three ranks of baffles and a 45° inclined cornice (Flamand, 2003).

Table 1.2 Aerodynamic coefficients from the scaled section model (Flamand 2003; King et al. 2010).

	C_D	C_L	C_M	$dC_D/d\alpha$	$dC_L/d\alpha$	$dC_M/d\alpha$
Composite section for main span	0.145	-0.097	-0.033	0.086	6.217	1.518
Concrete section for side span	0.190	-0.307	0.012	-0.115	7.678	0.285

After the preliminary study on the section model on the Wind tunnel located in France, the study of the full bridge aerodynamic model was initiated by members of the Engineer Institute (II), at UNAM (Universidad Nacional Autónoma de México, in Spanish). The main purpose of this second study was to provide an overall picture of the bridge response to wind forces and to assure the stability of the structure under high winds. On this occasion, the scaled model was studied under a three-dimensional gust wind condition, and over a full range of wind speeds. The study of the full aerodynamic model of Baluarte bridge was conducted at the University of Western Ontario, Canada (King et al. 2010).

A uniform wind profile and a profile of the expected site conditions were considered for the experimental setups. In both profiles, a portion of the topography near the bridge was considered, with the sole purpose of creating a transition between the floor and the base of the model (King et al. 2010). The Wind tunnel setups for a smooth flow simulation (without roughness elements) and for the expected site conditions are presented in Figure 1.3. A roughness length z_0 , of 0.0005 m and an average turbulence intensity of 0.2%, are

considered for the smooth flow profile. In the case of the expected site conditions, a roughness length z_0 , of 1.5 m, and an average turbulence intensity I_u , of 1.7%, are considered. The main purpose of the smooth flow profile is to identify any vortex shedding associated with the isolated pylon, or the erection and final stages of construction of the main deck. No instabilities were found below 37 m/s for the cantilevered construction stage, and below 45 m/s for the completed bridge configuration. The previous values are above the mean hourly wind speed at the deck level that is used for design purposes. In this case, the value of the 200-year, 3-second gust wind speed is 35.7 m/s. This guarantees that no instability would occur. The nominal damping of the actual bridge performed by CSTB was based on Eurocode or British Standard, which estimates $0.32\% \leq \xi \leq 0.64\%$. The studies at CSTB on actual bridges show that the damping can reach very low values and it was preferred to take the value of ξ , as 0.32%.

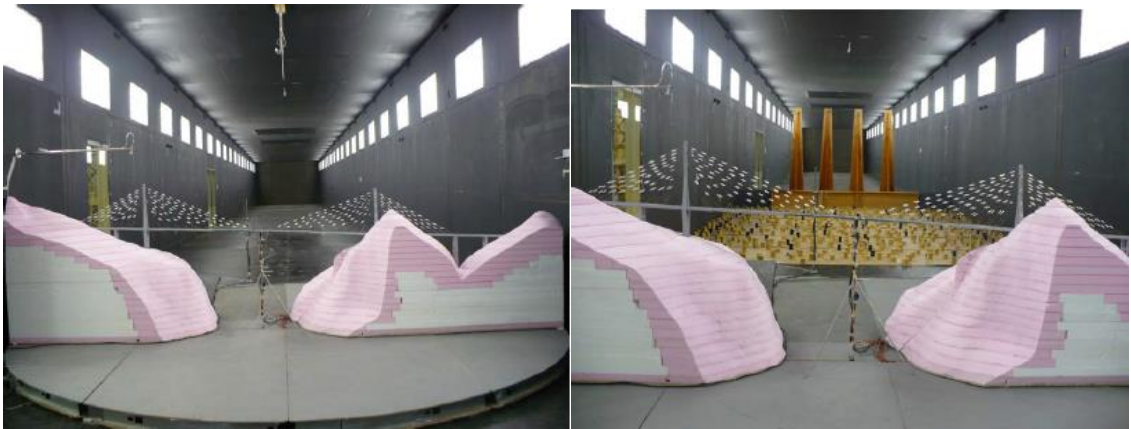


Figure 1.3 Simulation of the ABL for uniform flow and expected site conditions (King et al. 2010).

Several non-dimensional numbers are used regularly to translate the wind effects from the prototype into the scaled model on the Wind tunnel. Some of the most fundamental parameters associated with non-dimensional numbers are the thickness of the boundary layer δ , the reference velocity U , the reference pressure P , the gravitational acceleration g , the air mass density ρ , and the viscosity of the flow μ , or kinematic viscosity of the flow,

$\nu (= \mu/\rho)$ (Simiu and Scanlan 1996). Some of the non-dimensional numbers and associated parameters are defined as:

1. The Euler number $E_u (= p/\rho U^2)$, associates the different pressures throughout the model.
2. The Reynolds number $R_e (= U\delta/\nu)$ is the ratio of inertial to viscous forces.
3. The reduced frequency $f^* (= \delta n/U)$ can be either be the Strouhal number, if the frequency is associated with the vortex shedding frequency n_s , or the Rossby number if the frequency is associated with the Coriolis parameter f_c .
4. The Froude number $F_r (= U^2/g\delta)$, is the ratio of gravitational to inertial forces.
5. the Jensen number $J_e (= \delta/z_0)$, is the ratio of the roughness length to the boundary layer thickness.

The scale ratio of the boundary layer thickness λ_δ is the most important parameter, and other scale parameters depend on it. This parameter is not an independent quantity, and the selection of the Jensen number is related to the size of the wind tunnel, the thickness of the ABL, and the roughness length, z_0 . “When geometric similarity is preserved, “exact” dynamic similarity can be achieved if each of the following parameters is equal for the two systems: Rossby number (R_0); Richardson number (Ri); and Reynolds number (R_e)” (Cermak 1987). However, the modeling of the ABL is considered based on “approximate similarity”, in which the primary compromise is in the relaxation of the Reynolds and the Rossby numbers. The Rossby number, in general, can be eliminated from the similarity requirements if the horizontal length is less than 150 km. In the scaled turbulent boundary layer, the upwind terrain was modelled within the 42.6 m length of the wind tunnel section, which corresponds to 10.7 km of upwind fetch. In this case, the Rossby number is in the order of 0.1, and the convective or local accelerations dominate over the Coriolis acceleration (Cermak 1987).

On a scaled model, the roughness characteristics can make the flow approach similarity asymptotically and become Reynolds number independent. For turbulent flows, the

effective Reynolds number is in the order of 1000 times smaller than the one considered under the condition of laminar flow. With this in mind, it is possible to achieve similarity for the gross characteristics of gust winds. On the other hand, when considering a local cross section of the scaled model, if the geometry that interacts with the flow patterns presents sharp edges, the mean flow patterns can also become Reynolds number independent (Cermak 1966). The Reynolds number for the laboratory boundary layer is approximately 500 times smaller than those values of the atmospheric boundary layer (ABL) (Cermak 1984).

Some similarity requirements are presented in Table 1.3, where the subscript m and p are the real physical model and the prototype of the bridge. On the BLWT tests, the density ratio defined by λ_ρ , is preserved. The length scale ratio λ_L , which is the ratio between the physical length of the model L_m and the length of the prototype L_p is considered as 1:250. The velocity ratio λ_U , presents the same value as the time scale λ_T . The time scale λ_T , can also be defined as the reduced ratio of length λ_L divided by the reduced ratio of the velocity λ_U .

Table 1.3 Scaling parameters ratios between model and prototype.

Parameter	Unit	Reduced ratio	Similarity definition
Length	m	1:250	$\lambda_L = L_m/L_p$
Velocity	m/s	1:15.81	$\lambda_U = U_m/U_p$
Density	kg/m ³	1	$\lambda_\rho = \rho_m/\rho_p$
Time	s	1:15.81	$\lambda_T = T_m/T_p = \lambda_L/\lambda_U$
Mass per unit length	kg/m	1:62500	$\lambda_m = \lambda_\rho \lambda_L^2$
Mass moment of inertia per unit length	kg-m ² /m	1:3.91E9	$\lambda_j = \lambda_m \lambda_L^2$
Elastic stiffness	N-m ²	1:9.77E11	$\lambda_{EI} = \lambda_U^2 \lambda_L^4$

From the wind tunnel tests, it was decided that the Froude number $F_r (= U^2/g\delta)$, should be preserved. Since velocity and length scales are coupled by the Froude number, low wind speeds are considered in the simulation. Another number that was preserved in the tests was the Cauchy number $Ca (= \rho U^2/E)$. This last number represents the ratio of the elastic forces of the bridge to the inertial forces of the flow. The Cauchy number is related to the similarity requirement of the elastic stiffness λ_{EI} . The parameter of mass per unit length is related to the length reduced ratio squared λ_L^2 and the density reduced ratio λ_ρ . The mass moment of inertia per unit length is related to the ratio of mass per unit length and the reduced ratio of velocity squared λ_V^2 . For more information in regards to the scaled parameter the reader is referred to King et al. (2011).

1.5 Computational fluid dynamics (CFD) in the study of bridges

Incident wind flow and forces on bridges are related by means of static nonlinear relationships based on steady coefficients and their derivatives, throughout the use of quasi-steady theory (Davenport, 1962). However, this type of theory cannot cope completely with the unsteady nature of the wind forces and the problem of fluid-structure interaction. Even though flutter derivatives can deal with the problem of unsteady forces, the theory is only valid for small displacements, before the actual onset of flutter (Scanlan and Tomoko, 1971). Another type of nonlinear behavior of the flow-deck system is produced at a high incidence angle of the wind, or at a high stall. In some cases, highly complicated flows can be developed, which can also alter the original configuration of the deck section. The study of Computational Fluid Dynamics (CFD) can be of great advantage in the prediction of aerodynamic forces or for the study of highly complicated flows (Dagneu and Bitsuamalak, 2013). CFD models can also enhance our understanding of the phenomenon of fluid-structure interaction. This section included within the first chapter is devoted to a brief introduction into Computational Fluid Dynamics (CFD), and the role of this discipline in the study of bridge aerodynamics.

Nowadays, bridges have incredibly large spans that are spanning between one and two kilometers. These types of structures are likely to present all kinds of difficulties in relation

to experimental and analytical models. And perhaps the section of the Wind tunnel in which this type of model could be studied must be of quite an enormous size. In this case, not all conventional tunnels can cope with that requirement. For the study of flow structure interaction, wind tunnel tests have been the dominant procedure via the use of flutter derivatives. Flow separation and reattachment, three-dimensional and complex geometric environments are inherent qualities associated with the wind flow (Dagnev and Bitsuamalak, 2013). In recent years, the advances in computational power and turbulence modeling on Computational wind engineering (CWE), had made these types of modeling an attractive alternative for the study of aerodynamic forces. The term CWE in this case refers to the study of the structure of the wind flow, whereas the term CFD is referred to the use of any kind of fluid flow (Tamura, 2015). One of the advantages of the use of CFD is the direct applicability of high Reynolds numbers under the computational domain.

Typical Reynolds numbers in the order of 10^5 - 10^8 (Turkiyyah et al, 1995; Patruno, 2015), are used for CWE simulations. This range of the Reynolds number are the ones regularly used under the Wind tunnel under operational conditions. Beatke and Werner (1990) pointed out, that numerical simulations of turbulent flows over and around different obstacles, with the use of high Reynolds numbers, are an important aspect in the study of wind engineering. For instance, elements such as cables, elements with smooth edges, and decks at high stalls are influenced by a difference in the Reynolds number. A numerical simulation around a fixed section model of the Great Belt East bridge is presented by Kuroda (1997), with particular emphasis on high Reynolds numbers. The comparison of the steady coefficients obtained from their computational model on CFD compared well with those obtained from the Wind tunnel at the Danish Maritime Institute (DMI). The flutter derivatives and the critical wind speed of a great diversity of bridge decks typologies are presented by Patruno (2015). This study is related to the use of different Reynolds numbers and different incidence angles of attack from the wind. It was found that the cases that are more susceptible to a variation in the Reynolds number, are those measured at different angles of attack.. Another study associated with the study of the Reynolds number is the one presented by Sarrate et al. (2001). In this study, Sarrate and associates presented an algorithm for fluid rigid body interaction, and an analysis of the attenuation of the rotational motion of a rectangular cylinder submerged in a viscous fluid.

Two of the main methods used in CFD to generate the flow field are the Reynolds-averaged Navier Stokes (RANS) and the Large Eddy Simulation (LES) (Dagnew and Bitsuamalak, 2013). The RANS model is recommended for geometrically simple domains with simple boundary conditions. The RANS model offers maximum accuracy for a reasonable computational cost and is very practical for the case of a 2-D analysis. Nevertheless, this type of model is not recommended for a wide range of flows and geometries (Ferziger, 1993). The analysis of the steady wind around the main deck of the girder, for the Baluarte bridge is presented in Appendix A. In this case, a RANS simulation is considered for the analysis on CFD. The main objective of Appendix A is to present the contours of the different velocities around the deck and to highlight the shortcoming associated with the strip assumption, and quasi-steady theory that was previously discussed in section 1.2. Although this is not a rigorous deduction, we can observe that the steady flow is translated into a range of different pressures around the deck, which highlights the actual difference between oncoming wind and measured pressures.

While the steady force might be well computed by a RANS model, the frequency and intensity of the unsteady forces are better represented by LES. The latter type of model is recommended for the study of a three-dimensional model, or for the study of separated flows (Beatke, 1990). Well-resolved LES models are not generally recommended, since the grid requirements can become computationally overwhelming. Also, establishing a fully developed turbulence model may take a significant amount of computing time. Therefore, in order to provide initial turbulent conditions is important to initialize the flow with a particular form of perturbation. It is also important that the perturbation must be spatially correlated as in the case of real flows (Huang et al, 2010). Some LES simulations can start by initializing the inlet boundary condition from the flow field of previous RANS solutions. The Reynolds stress terms from the previous RANS solution are used to construct the spatially and temporally correlated perturbed inlet for the initial conditions of the LES model (Smirnov et al. 2001). A turbulence inflow generator technique that is used as the inflow boundary condition in LES is proposed by Aboshosha et al. (2015). The proposed technique can reproduce, both the turbulent spectra and the coherence function of the target atmospheric boundary flow (ABL).

An analysis by CFD of an unsteady flow field past a two-dimensional square cylinder is reviewed by Murakami and Mochida (1995). While it is found that the 2-D computation of the LES cannot provide a good representation of the flow field around the square cylinder, a 3-D LES results in a better agreement between computational and experimental data from the Wind tunnel. Larsen and Walther (1997) also considered a 2-D analysis, but contrary to Murakami and Mochida they applied the discrete vortex method. In the study of Larsen and Walther, the drag coefficients, Strouhal number, and the aerodynamic derivatives of different girders are assessed. In the study of CFD models, it is found that there are sections that are characterized by strong detachments on the leading edge. Predicting the moving reattachment point on the top and bottom flanges of a girder is an equally challenging problem. According to Frandsen (2004), the flutter predictions appear to be mainly affected by the leading-edge separations and the associated pressure forces. In this respect, CFD can improve our understanding of the complexities associated to different types of flows. Besides, CFD models can also support information gathered from experimental studies under the Wind tunnel.

Most fluid FE analyses are accomplished using the Eulerian description in which the mesh is fixed in space and the material particles flow through the mesh. The flow simulation around a stationary bridge deck adopts the Eulerian scheme in the entire fluid domain. In an aeroelastic analysis, the Eulerian description is inadequate as the domain surrounding the structure is itself in motion. The usual numerical representation for structural motion is the Lagrangian description in which the mesh motion coincides with the motion of the material particles. The discrete vortex method, which is used extensively by Larsen and Walther (1997), made use of the Lagrangian formulation. In this type of representation, the equations of the flow are formulated in terms of vorticity rather than in terms of velocity (Barba et al. 2005). One of the main difficulties for the vortex methods to be accepted in main CFD, is related to their numerical complexity. The fluid structure interaction on CFD is sometimes treated as a moving boundary problem. The study of the problem of a classical flutter on the Great Belt East Bridge (Denmark), is considered by Frandsen (2004). In this case, Frandsen considers an Arbitrary Lagrangian-Eulerian (ALE) finite element method for the simulation of fluid domains with moving structures. The interface between the fluid and the solid domains is part of the fluid domain, and its position

is unknown a priori (Sarrate et al. 2001). The Lagrangian scheme is adopted near the boundaries between the fluid and the moving structure, and it gives the fluid the ability to be deformed, accordingly. The Eulerian formulation is used in the remaining fluid domain.

Flutter derivatives of the Great Belt East Bridge are identified by CFD simulation by Grinderslev et al. (2018), and compared with experimental results from the Danish Maritime Institute (DMI) and the University of Western Ontario. Reasonable agreement between the results from CWE and experimental results demonstrates the potential application of CFD for nonlinear aeroelastic analysis. However, caution must be taken for decks with secondary elements. The study of CFD models related to the interaction between flow and structure can be of great advantage in the understanding of bridge aerodynamics. Besides, the simple visualization of the flow that the CFD models provide, can enhance our understanding concerning the accurate representation of the wind flow.

1.1 Objectives and thesis organization

Considering the complexity of the physical study of turbulence, and the interaction between the random characteristics of gusts and the motion of the bridge deck, the quasi-steady theory is a convenient tool for the calculation of displacements. However, in the case of vertical displacement for long-span bridges, the lengthscales of the vertical gusts are not necessary larger than the depth of the bridge deck. In this case, what is needed is a more in depth understanding of the character of the gust forces, and in particular for the physical characterization of the coherence that would be evaluated on the numerical model.

In actuality, a distinction is made between the coherence of the wind fluctuations and the coherence of the actual wind forces on the bridge deck. In this case, it is established by previous experience that the coherence of the wind forces is greater than the coherence of the fluctuating wind (Larose and Mann, 1998). When experimental data of the force coherence is not available, the decay parameter can be used to establish the gap that exist between the coherence of wind fluctuations and the coherence of wind forces (or pressures). Consequently, a more reliable prediction of the wind forces acting on the deck can be established.

The main objectives of this thesis are:

- 1) To give an overall perspective on the progress of bridge aerodynamics and wind engineering, and to explore the study and calibration of numerical models in regards to the experimental scaled model studied under the BLWTL.
- 2) To compare the mean and RMS responses of the Baluarte bridge obtained from the aeroelastic model test, including the topographical effects, to the response obtained based on a developed finite element model subjected to an inhomogeneous wind field on the frequency domain
- 3) To compare the mean and RMS responses of the Baluarte bridge obtained from the aeroelastic model test, including the topographical effects, to the response obtained based on a developed finite element model subjected to an inhomogeneous wind field on the time domain.
- 4) To compare the differences of the RMS responses on the numerical model, when applying the frequency domain or the time domain approach.
- 5) To show that the time domain approach can be easily employed to evaluate the response of the bridge subjected to nonstationary and inhomogeneous wind fields.
- 6) To evaluate and analyse the underlying conditions that generate the discrepancy between the results on the RMS displacements, obtained from the BLWT tests and the numerical modeling, based on previous experiences from similar studies conducted in the past (similarities and differences between experimental and numerical modelling).
- 7) To establish the importance of the decay parameter for the correct parametrization of the force coherence, when experimental data are not available to determine the experimental coherence. In this case, a sensitivity analysis of the decay parameter is conducted to determine the rate of change of the RMS vertical displacement in relation to different values assigned to the parameter.

To achieve these objectives, a detailed finite element of the Baluarte bridge is developed. The dynamic characteristics of the finite element model are compared with those obtained from the BLWT tests. The results of this sophisticated finite element model are used as the basis to evaluate equivalent section properties which are used to develop a simplified finite element model that can be used for evaluating the responses subjected to wind loads. A recapitulation of numerical models that are used for the study of buffeting where described in this Chapter 1.

The development of the finite element model, as well as the evaluation of the bridge responses to buffeting load on the frequency domain are presented in Chapter 2. In chapter 3, similar analysis is carried on, but this time considering the time domain analysis. In this Chapter a brief introduction to the characterization of nonstationary processes is also included. Finally, the main findings and final conclusions, as well as coments of the potential future research work are discussed in Chapter 4.

Chapter 2

2 Comparison of Boundary Layer Wind Tunnel Laboratory Test Results and Finite Element Results for Baluarte Bridge

2.1 Introduction

Long-span bridges are highly susceptible to wind excitations because they are light and flexible. The interaction between the wind and the bridge is quite complex. The theoretical basis to evaluate the bridge response to the wind load are well developed (Strømme 2010). The analysis of the wind-induced response of the a bridge system can be evaluated based on the frequency-domain approach or time-domain approach. The frequency-domain approach for estimating the structural response subjected to stochastic wind load was developed and elaborated by Davenport (1962, 1981, 1983) and by Scanlan and Tomko (1971). In this approach, the wind speed is decomposed into a mean wind component and a fluctuating wind component that is defined by its power spectral density (PSD) function. The use of the random vibration theory and the PSD function of the wind leads to the PSD of the response that is used to evaluate the gust factor. An extensive review of the numerical modelling and classification of the wind forces on bridges was presented in Salvatori and Borri (2007). It indicates that the wind load is usually linearized, and the load is classified as (i) a mean wind velocity dependent steady load, (ii) a fluctuating wind dependent buffeting load, and (iii) an aeroelastic self-excited load depending on the motion of the cross-section. The aeroelastic force can be further classified as quasi-steady self-excited forces, unsteady self-excited forces in the frequency domain (Scanlan and Tomko 1971), and unsteady self-excited forces in the time domain (Scanlan et al. 1974). The quasi-steady load is evaluated based on experimental coefficients measured on a rigidly supported cross-section. The unsteady load model for self-excited forces in the frequency domain is characterized by aerodynamic derivatives that depend on the frequency. The unsteady self-excited forces in the time domain are evaluated by using the convolution and the indicial functions.

The application of the frequency-domain approach was applied to estimate the response of bridges subjected to wind load by many researchers, including Davenport (1962, 1981, 1983), Jain et al. (1996), Simiu and Scanlan (1996), Xu et al. (1998), Sun et al. (1999), and Chen et al. (2000a, b), and Caracoglia and Jones (2003). The wind load acted on the bridge is sensitive to the geometric shape of structural components of the bridge, especially to the geometric shape of the deck (Gu et al. 2001; Chen and Kareem 2002; Chowdhury and Sarkar 2003).

Model scale tests of the deck section and full aeroelastic model of the bridge are often carried out to assess the drag, lift, and pitching moment coefficients, the change of these coefficients with respect to the attack angle of the wind, and dynamic characteristics. Moreover, aerodynamic derivatives of the bridge are estimated from the boundary layer wind tunnel test results, and the maximum structural responses, including the critical wind speed for instability, are also measured. Easy to implement procedures of the frequency approach with existing finite element software to estimate the bridge responses were presented in Hua et al. (2007) and Chen et al. (2009). However, a comparison of responses from the full aeroelastic model of the bridge, with those obtained from finite element modelling and by considering quasi-steady self-excited forces in the case of the frequency domain is scarce. It is noted that Diana et al. (1995, 2013) carried out a comparison of the responses obtained from the wind tunnel tests on a full aeroelastic model of the proposed bridge over Stretto di Messina. The tests and comparison were aimed at verifying the aerodynamic behaviour of the bridge in smooth and turbulent flow and the threshold wind speed for the flutter instability.

For the case of a frequency domain approaches, Sun et al. (1999) uses a finite element approach and a pseudo excitation method for the characterization of wind forces. The pseudo excitation method considers the wind load spectra in terms of the power spectral density function (PSDF) for wind processes, and the spectrum is discretized into its different frequency components and applied to the structure as a series of harmonic loads. In the case of considering the effects of self-excited forces, aeroelastic forces on a bridge deck are changed into nodal forces to form aeroelastic damping and stiffness matrices. Frequency domain analysis is based on a linear hypothesis, where the evaluation of the

response can be considered by numerically integrating the product of the bridge's transfer function and the wind load spectra (Yang et al. 1997).

It must be emphasized that the pressure coefficients, and the rate of their change with the angle of attack, are sensitive to the geometric and dynamic characteristics of the bridge. As such characteristics vary from a bridge to bridge, the test of a full aeroelastic model of a proposed major bridge is always carried out in a boundary layer wind tunnel. A major cable-stayed bridge – Baluarte bridge – was proposed and constructed in Mexico. The bridge crosses a gorge in the Sierra Madre Occidental mountains with a clearance of 390 metres below the deck; the bridge is one of the most important of its kind in the world. A full aeroelastic model of the bridge was tested in the Boundary layer wind tunnel laboratory (BLWTL) at the University of Western Ontario (UWO). The test was carried out in the topographic flow conditions by including the topographic model as well. The inspection of the design and construction of the Baluarte bridge was under the supervision of the Institute of Engineering at the Autonomous National University of Mexico (UNAM).

The main objectives of this chapter are to carry out the finite element modelling of the bridge, compare the dynamic characteristics of the aeroelastic model, and most importantly, compare the measured responses to those calculated by using the established finite element model. The bridge response evaluation in this chapter is carried out using the frequency-domain approach. The considered wind forces are those determined based on the quasi-steady theory. It is acknowledged that some of the aerodynamic derivatives for the section model of the bridge were available for the Baluarte bridge (Costa et al. 2007), the consideration of these coefficients for the unsteady self-excited forces as well as the study of a yaw angle of the mean wind is outside of the scope of this study.

2.2 General characteristics of the bridge

The Baluarte Bridge is a cable-stayed bridge located at the border between the states of Sinaloa and Durango, in the Northwest part of Mexico. This bridge that is in operation since 2013 has a total length of 1224 m, and a mid-span length of 520 m. The main deck of the bridge reaches a maximum height of 390 m above the canyon (with the road deck at 403 m above the valley below), which is one of the highest bridges in the world. A full

perspective of the bridge is presented in Figure 2.1.

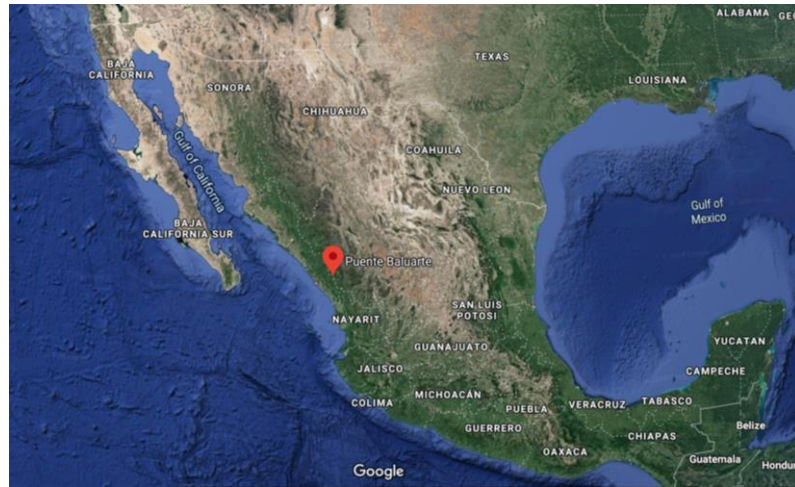


Figure 2.1 Location and photos: a) Geographic location and, b) and c) photos of Baluarte bridge (<https://vidamaz.com/2013/11/09/our-first-trip-on-the-durango-mazatlan-highway-and-the-baluarte-bridge/>; <https://www.pinterest.ca/pin/364017582355349438/>).

The superstructure of the bridge is supported by two delta shape pylons, eight reinforced concrete frame piers, and two abutments at the ends of the bridge. The two main pylons are made of a hollow concrete box section. Their total heights are 169 m for the pylon situated on the side of Durango, and 147 m for the pylon on the side of Mazatlán. From each one of the main pylons, 76 stayed cables are anchored to the upper section of the pylon and to the edge of the deck. All piers are made of reinforced concrete frames, by a system

of columns connected by post-tension beams. The height of the piers ranges from 40 to 140 m, approximately. An elevation view of the whole bridge is presented in Figure 2.2. In the case of the superstructure, the cross-section of the side-spans is made of prestressed concrete box dowels and the main-span of A-50 steel I beams. Both cross-sections are presented in Figure 2.3.

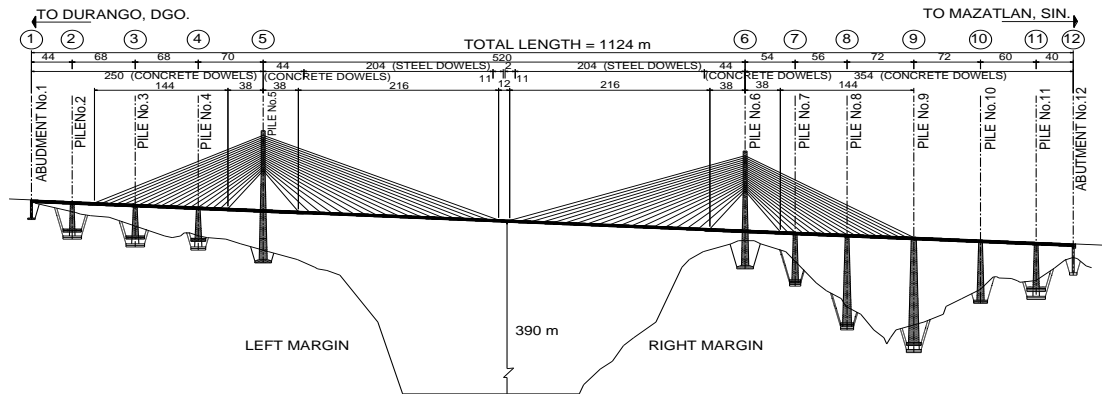


Figure 2.2 Elevation view of the bridge (Pozos-Estrada et al. 2016).

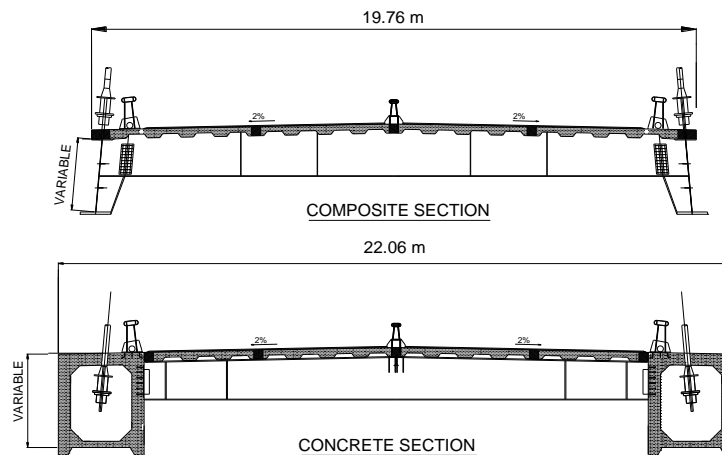


Figure 2.3 Cross-section of the main span (top plot) and side span deck (bottom plot) (King et al. 2011).

The cover slab for the superstructure is of prestressed concrete. A membrane of asphalt concrete on top of the slab is used as the bearing surface. The widths of the cross-sections

are 22.06 and 19.76 m, for side-spans and midspan, respectively.

An aeroelastic model was designed for the whole bridge with a geometric scale of 1:250 (see Figure 2.4). This scale was determined based on the characteristics of the turbulent wind flow generated in the wind tunnel, as well as the overall length of the bridge (King and Kong 2010; King et al. 2011). In addition to the overall geometric similarity, the design of the full aeroelastic model preserved the Froude number and the Cauchy number scaling. The density ratio was preserved, and the damping ratio was assumed to take a value of 0.32% of the critical. The full aeroelastic bridge model was tested under smooth and topographic flow conditions in the Boundary Layer Wind Tunnel Laboratory (BLWTL) at the University of Western Ontario (UWO) (King and Kong 2010). The test results of the whole bridge aeroelastic model, including the dynamic characteristics, the mean wind response, and the buffeting responses, are also presented in King and Kong (2010). The dynamic characteristics of the full bridge aerodynamic model on the wind tunnel and the sophisticated and simplified FE model are presented in Table 2.1.

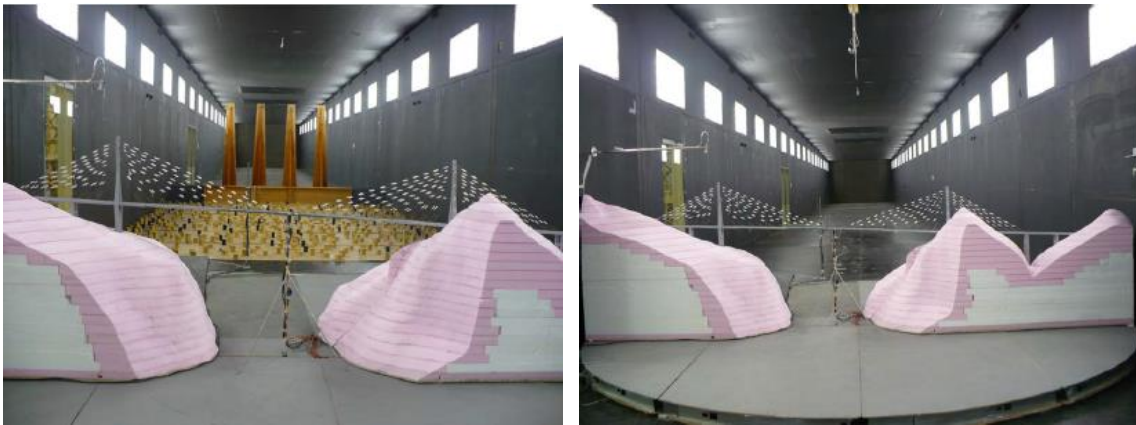


Figure 2.4 Test setup in the BLWTL at UWO (King and Kong 2010).

Table 2.1 Dynamic characteristics of the bridge.

	Test (BLWTL)	Sophisticated 3D-FE model		Simplified FE model	
		FE analysis	Relative difference		
Mode shape	Frequency (Hz)				
Lateral vibration	0.251	0.251	< 0.1%	0.251	< 0.1%
Vertical vibration	0.299	0.299	< 0.1%	0.309	3.4%
2 nd lateral vibration	0.388	0.405	4.2%	0.397	2.4%
Torsion	0.434	0.437	0.6%	0.435	0.2%

Before the study of the full aerodynamic model test on the BLWT, a section model test for the deck was initiated at CSTB(Centre Scientifique et Technique du Batiment, in French), by Flamand,(2003) in France. The main objective of the study conducted by Flamand was to assess the aerodynamic characteristics of the central span of the bridge deck during construction and at the service stage. The considered geometric scale for the scaled model of the deck is 1:50. The aerodynamic coefficients, from the tests, are summarized in Table 2.2. In this case, C_D , C_L , and C_M are the drag, lift, and pitching moment coefficients, and α represents the incidence angle. The rate of change of the drag coefficient is positive for the composite section and negative for the concrete section considered for the side spans. The rate of change for the lift and moment coefficients are both positive. In addition to the aerodynamic coefficients for the deck, the drag coefficients for the principal pylons and the cables are equal to 1.7 and 1.2, respectively (CAN/CSA S16-19 2019).

Table 2.2 Aerodynamic coefficients for drag, lift, and moment, and their derivatives with respect to the angle of attack from the scaled section model.

	C_D	C_L	C_M	$dC_D/d\alpha$	$dC_L/d\alpha$	$dC_M/d\alpha$
Composite section for main span	0.145	-0.097	-0.033	0.086	6.217	1.518
Concrete section for side span	0.190	-0.307	0.012	-0.115	7.678	0.285

After the studies conducted by Flamand on the scaled deck section of the bridge, the studies of the scaled full bridge were conducted at the BLWT at UWO by King et al. (2011). In the study of the scaled full aerodynamic model of the bridge two characteristic wind profiles are characterized. In the first case a free flow simulation to study possible vibrations and instabilities on the bridge, and in the second case, a flow simulation of the expected site conditions which also considers the surrounding topography. A roughness length z_0 of 1.5 m and an average turbulence intensity I_u of 15% are considered for the case of the expected site conditions, and for the simulation of the wind profile. In contrast, a roughness length z_0 of 0.0005 m and average turbulence intensity, I_u of 2%, are considered for the free flow simulation. In order to provide a transition between the floor and the base of the model for both types of flow, a portion of the topography near the bridge was modelled (Fig 2.4) (King et al. 2011).

2.1 Validation of Finite Element Models based on experimental results from the BLWTL

2.1.1 Finite element modelling

A three-dimensional FE (3D-FE) model of the Baluarte Bridge is developed in ANSYS (2017), according to the prototype design employed for the full aeroelastic model. The material properties and geometric variables consistent with those used for the prototype design are used to develop the FE model for the bridge. These variables are given in Table 2.3. A complete isometric view of the developed model and the global coordinates are depicted in Figure 2.5. There are a total of 13765 elements for the developed FE model with an average element size of 4 m. The model is developed by taking into account the requirement of accurate modelling but with a manageable computational effort for evaluating peak wind responses. The full-bridge FE model, including the piers, pylons, deck, and cables, are modelled with details given below.

Table 2.3 Parameters considered for developing the FE model of Baluarte Bridge.

Bridge component	Member	Parameter	Value used in the FE model
Deck	Longitudinal steel girder; steel supporting beam.	Elastic modulus	200 GPa
		Density	$7.85 \times 10^3 \text{ kg/m}^3$
		Poisson's ratio	0.30
	Concrete topping	Elastic modulus	24.9 GPa
		Density	$2.83 \times 10^3 \text{ kg/m}^3$
		Poisson's ratio	0.15
	Concrete girder	Thickness	17.5 cm
		Elastic modulus	24.9 GPa
		Density	$2.40 \times 10^3 \text{ kg/m}^3$
Pylon	Hollow concrete sections	Poisson's ratio	0.15
		Material properties are the same as for the concrete girder.	
Pier	Hollow concrete sections	Thickness ⁽¹⁾	40 cm
		Material properties are the same as for the concrete girder.	
Cable	Circular cross-sections ⁽²⁾	Thickness	70 cm
		Elastic modulus	195 GPa
		Density	$7.85 \times 10^3 \text{ kg/m}^3$
		Poisson's ratio	0.30
		Area	$1950 \sim 8680 \text{ mm}^2$
		Length	$62.09 \sim 270.05 \text{ m}$

Note: (1). The thickness of 40 cm is obtained by averaging the design thickness of the hollow sections of the pylon; (2). The material properties of cables are obtained from the design data.

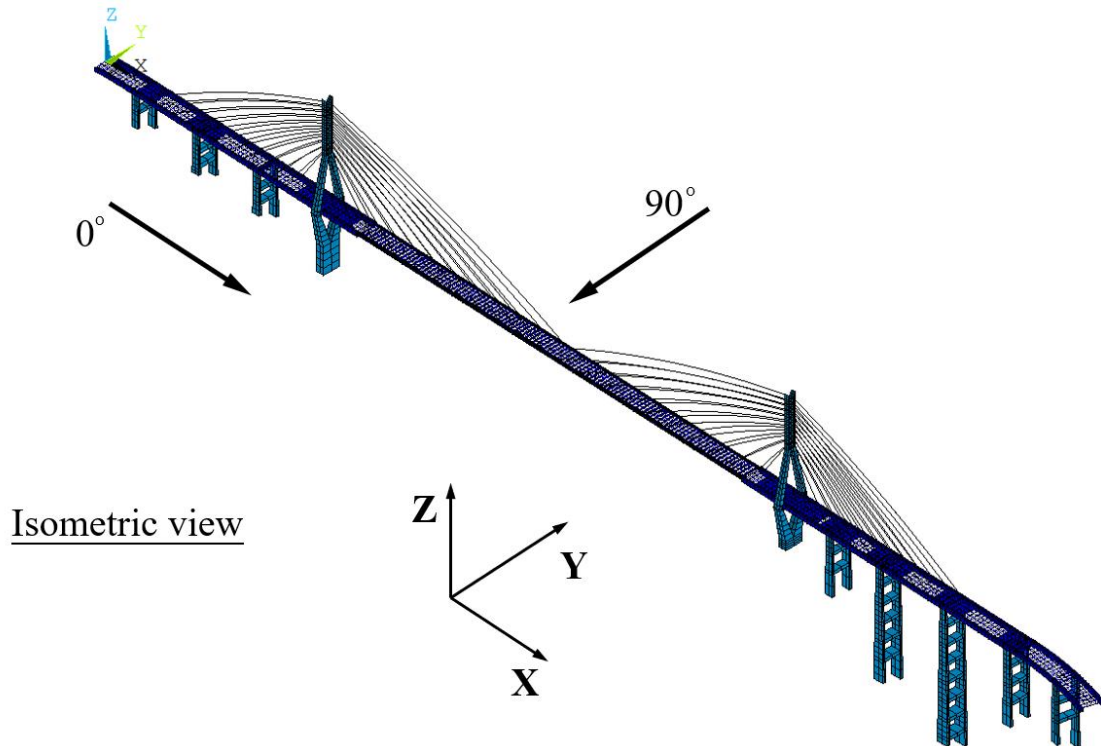


Figure 2.5 Isometric view of the (high-resolution model) 3D-FE model of Baluarte Bridge.

The piers and pylons of the bridge are modelled using the SHELL181 element (see ANSYS (2017)) with three or four nodes depending on the shape of the meshed element. There are six degrees of freedom at each node, including translations in the x , y , and z directions and rotations about the x , y , and z -axes. Since the piers and pylons are designed with hollow cross-sections, the use of the shell element is considered to be suitable to analyze these thin shell structures. The coordinates of the nodes and thickness for the shell elements are defined in accordance with the prototype design. To accurately reflect the tested full-scale aeroelastic model, the first and the last piers of the bridge, as designed, are not included in the FE model, since they are not included in the aeroelastic model.

The bridge deck consists of concrete topping, concrete box girders (longitudinal), steel girders (longitudinal), and steel supporting beams (longitudinal and transversal). Except for the steel supporting beams, other components are modelled by SHELL181 element with four nodes. The use of such an element is due to the fact that it is well-suited for linear, large rotation, and/or large strain nonlinear applications. The coordinates of the nodes for

defining the shell elements, as well as the thicknesses of each component, are defined in accordance with the prototype design. For the concrete topping, an equivalent thickness of 20 cm is used to take into account its half-hollow shape. The steel supporting beams beneath the concrete topping are modelled by using the 2-node BEAM188 element in ANSYS for its suitability and computation efficiency. For modelling the supporting beams, the nodes used to define the shell elements for the concrete topping are first selected according to the design geometry of the supporting beams. The selected nodes are then used to model the beam elements with defined cross-sections. Further, these elements are offset to the actual location of the supporting beams to form a concrete-steel composite deck component. An illustration of the modelled concrete-steel composite deck is shown in Figure 2.6, where the modelled components of the deck are rigidly connected.

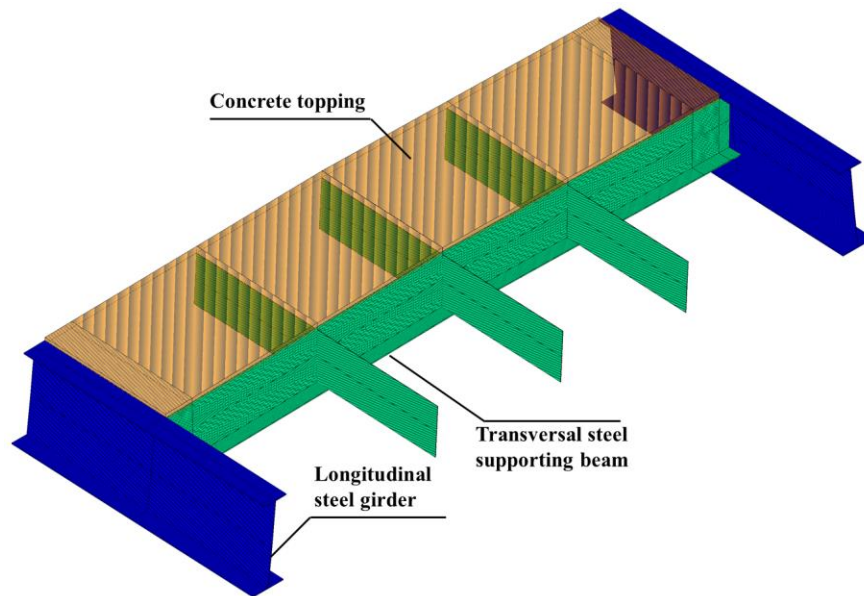


Figure 2.6 Modelling of the deck of mid-span.

The stay cables are modelled by the 2-node TRUSS180 element in ANSYS. Each node of the element has three translational degrees of freedom, and the element is specified to take the tension only along the direction of the cable. Again, the geometry of the cables and their corresponding material properties are consistent with the full-scale model (King and Kong 2010).

The cables are pre-tensioned due to the effect of the dead load from the deck and self-weight. To define the initial geometry of the cable profile and the coordinates of the nodes, an iterative procedure is used to calculate the coordinates of the needed nodes to define the elements for the cable. The procedure starts by modelling the geometry of the cable and deck without gravity load. Static analysis is carried out by applying the gravity load to determine its deformed shape and the corresponding coordinates of the nodes. Since the deformed shape is unlikely to meet the straight target line of the deck, the coordinates of the nodes for the deformed cable are adjusted iteratively to meet the target configuration of the deck. The results from the initial configuration of the cable for the last iteration (i.e., before applying gravity) are used to define the initial geometry of the cable profile. Further, the initial strain for the last iteration is adjusted to ensure the strain of cable due to gravity load is identical or within a specified tolerance to the strain calculated by using design tension (which includes the load effect from the dead load of the deck).

The boundary conditions of the Finite Element model are as follows. Fixed restraints are used between the deck and pylon, and deck and piers through coupling the degrees of freedom of the connecting nodes. The cables are hinged at both ends. The foundations of the piers and pylons are fixed to the ground. The ends of the bridge are restrained for the vertical motion and deck torsion but allow for longitudinal displacement.

A modal analysis is carried out using the developed FE model to identify the dynamic characteristics of the bridge. More specifically, the dead load (i.e., gravity load) is first applied to the modelled bridge. The modal analysis is then performed considering the stress caused by the pre-tensioned cables. Four identified modes with the predominant motion of the bridge (i.e., the modes with the predominant motion of cables are ignored) are identified and shown in Figure 2.7. The obtained vibration frequencies are summarized in Table 2.1 and compared with those obtained from the aeroelastic model. The table shows that the predicted dynamic characteristics of the bridge by using the developed detailed 3D-FE model match well those obtained from the tests. The relative differences are less than 5% for the considered modes.

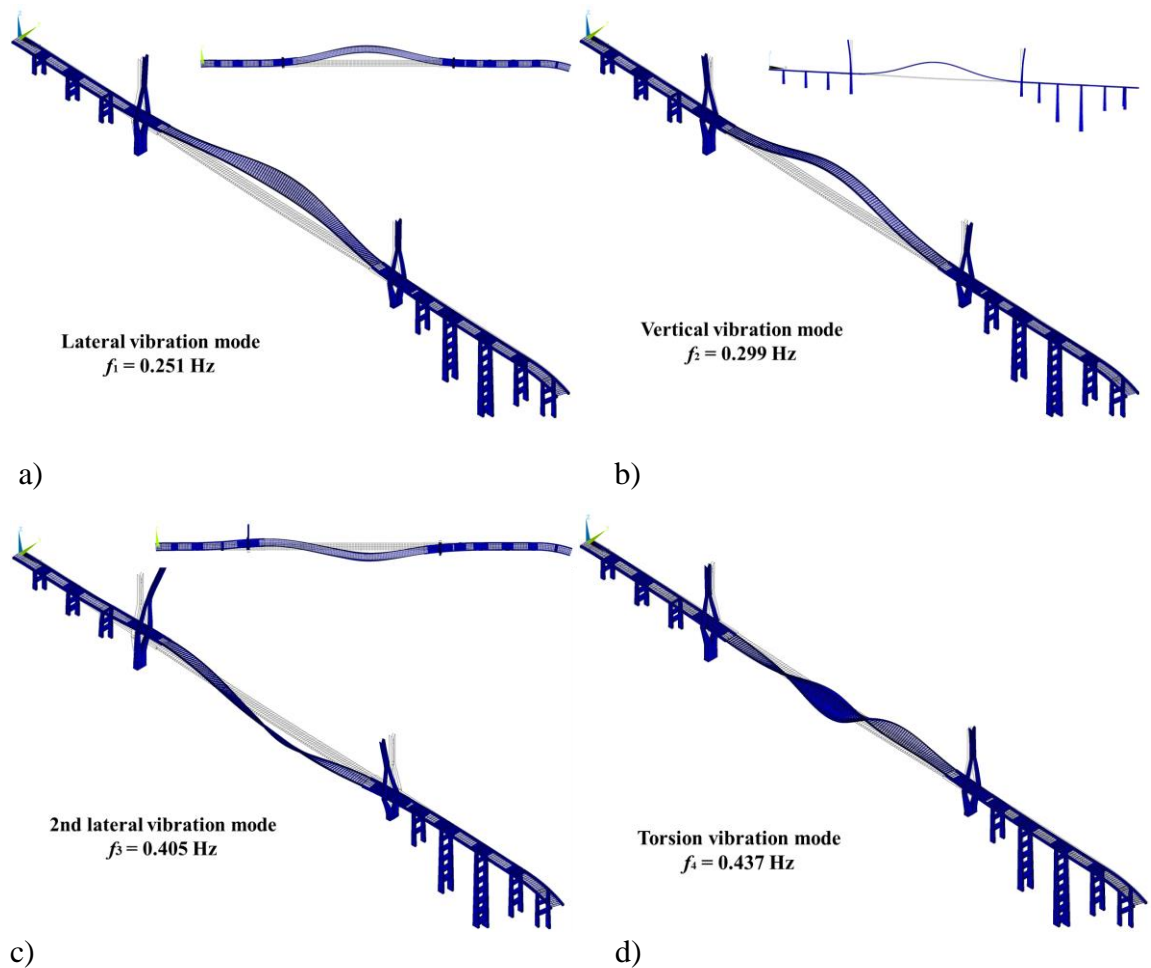


Figure 2.7 Identified vibration modes by using the 3D-FE model.

2.1.2 Simplified FE model and its dynamic characteristics

An attempt is made in applying the frequency-domain and time-domain analysis procedure to estimate the wind responses. It is found that the use of the sophisticated 3D-FE model described in the previous section for such a purpose is extremely time-consuming. Subsequently, a simplified version of the sophisticated 3D-FE model of the bridge is developed. The simplified 3D FE model with 1565 elements is shown in Figure 2.8. For the simplified model, the equivalent material properties and geometric variables shown in Table 2.4 are used. The equivalent material properties and geometric variables are derived based on the sophisticated FE model presented in the previous section. The estimation of the equivalent properties for the simplified model is explained in the

following.

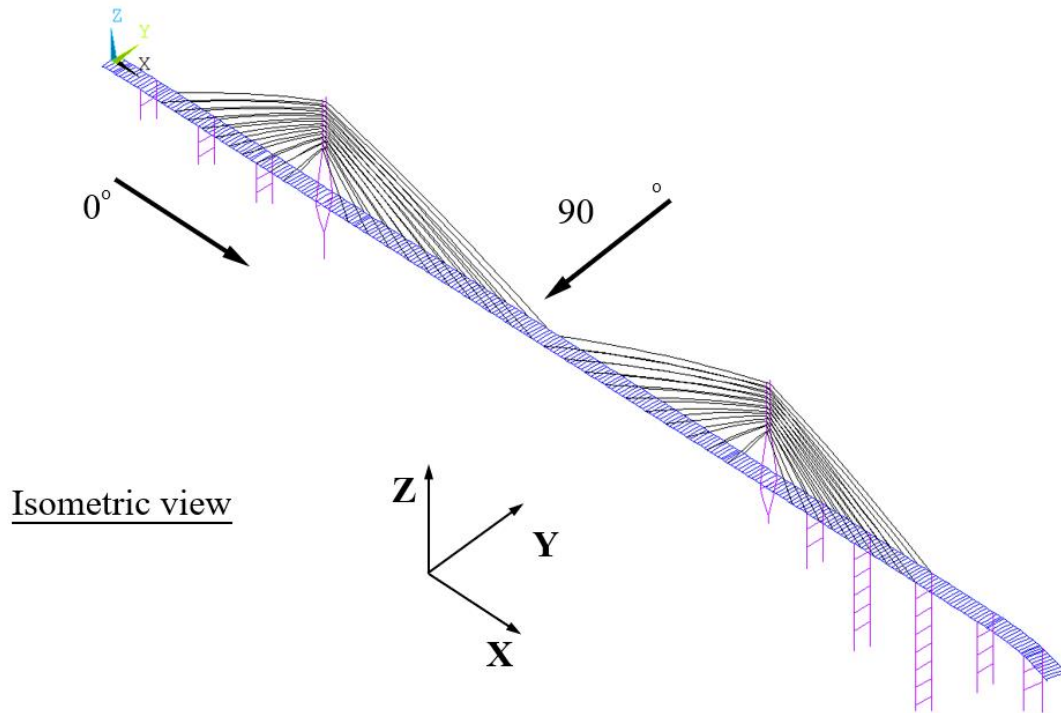


Figure 2.8 Isometric view of the simplified 3D-FE model of Baluarte Bridge.

Table 2.4 Parameters for simplified FE model.

Bridge component	Member	Parameter	Value used in the FE model
Deck	Longitudinal steel girder; steel supporting beam.	Elastic modulus	200 GPa
		Density	$7.85 \times 10^3 \text{ kg/m}^3$
		Poisson's ratio	0.30
	Concrete topping	Elastic modulus	68 GPa
		Density	$3.25 \times 10^3 \text{ kg/m}^3$
		Thickness	30 cm
		Width per element	2.5 m
	Concrete girder	Poisson's ratio	0.15
Pylon	Hollow concrete	Material properties are the same as the sophisticated model	Material properties are the same as the

sections		sophisticated model	
		Cross-section area ⁽¹⁾	5.04 ~ 6.68 m ²
Pier	Hollow concrete sections	Material properties are the same as the sophisticated model	
		Cross-section area ⁽¹⁾	5.26 ~ 8.64 m ²
Cable	Material properties are the same as the sophisticated model		

Note: (1). The cross-section area is obtained by averaging the design cross-sections of the hollow sections of the pylon.

For the simplified 3D-FE model, the deck of the bridge is modelled using the 2-node BEAM188 element with six degrees of freedom at each node. The concrete topping of the deck is represented by using the horizontal beam elements along the transversal direction of the bridge with an interval of 4 m. The material properties and the cross-sections of the beam elements used to represent the topping are adjusted through trial and error such that the mass and stiffness of the deck of the sophisticated and simplified 3D models are practically identical. The beam element is also used for longitudinal girders, forming a frame to represent the deck of the bridge, as shown in Figure 2.9. In the figure, the simplified model of the main span deck with defined cross-sections for the beam elements is also shown. A comparison of the properties of the main span deck for the sophisticated and simplified 3D-FE models is presented in Table 2.5, indicating that their resemblance is satisfactory. For the simplified FE model, the hollow cross-sections for piers and pylons are modelled using the average section area. For the cables, the same model used for the sophisticated FE model is employed. The considerations for the connections and boundary conditions are identical to those for the sophisticated 3D-FE model, as explained in the previous section.

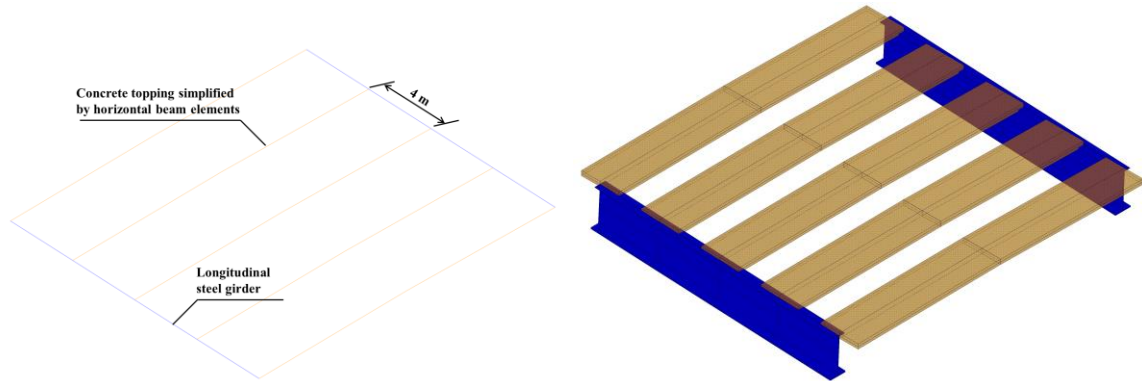
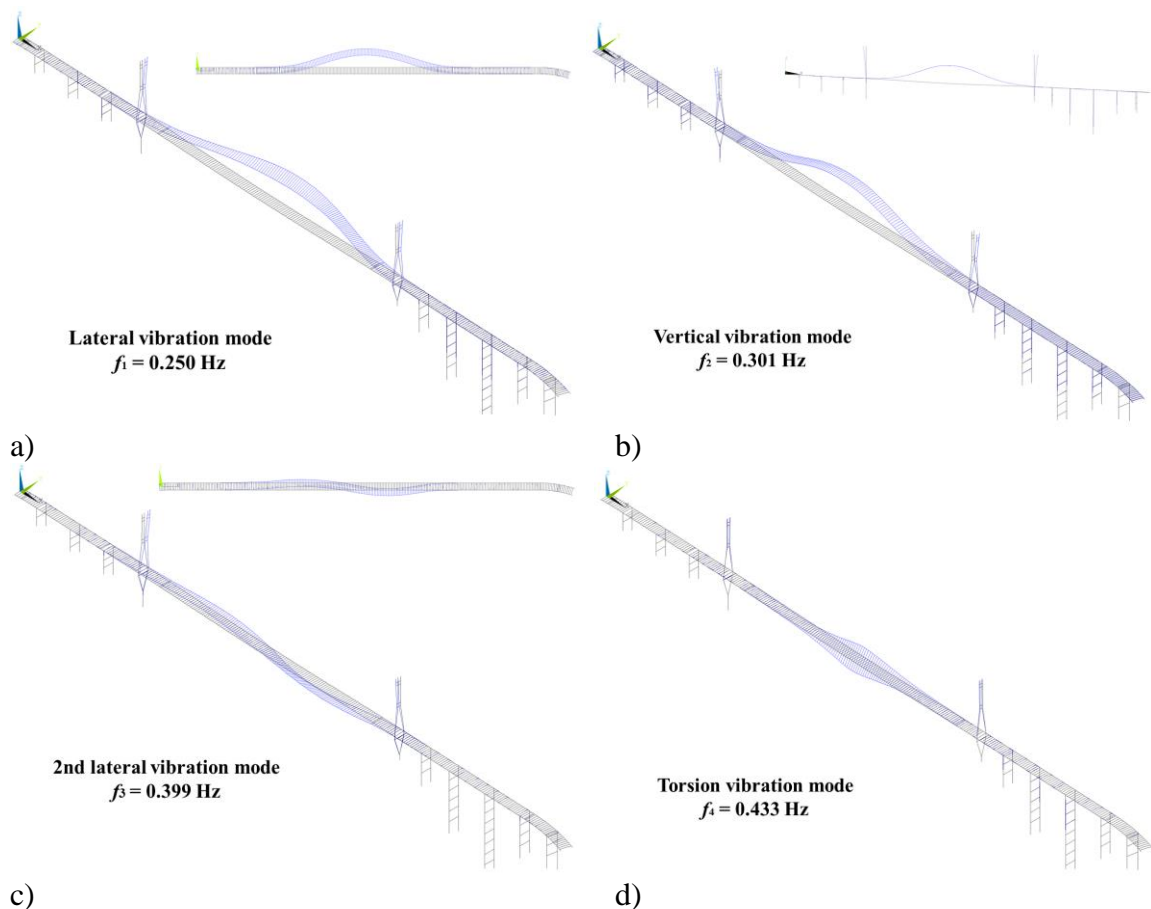


Figure 2.9 Simplified model of the main span of the deck: a) frame formed by beam elements; b) beam elements with defined cross-sections.

Table 2.5 Comparison of the properties of the main span deck.

Parameters	Sophisticated FE model	Simplified FE modal	Relative difference
Vertical moment of inertia	2.27 m ⁴	2.12 m ⁴	7.0%
Lateral moment of inertia	67.44 m ⁴	64.18 m ⁴	5.1%
Torsional constant	1.95×10 ⁻³ m ⁴	1.89×10 ⁻³ m ⁴	3.2%
Mass per unit length	19912 kg/m	19195 kg/m	3.7%

A modal analysis is carried out to obtain vibration modes and vibration frequencies. The obtained four vibration models corresponding to those shown in Figure 2.7 are shown in Figure 2.10, and the comparison of the vibration frequencies to those obtained from the wind tunnel test is shown in Table 2.1. The vibration models shown in Figure 2.10 are consistent with those presented in Figure 2.7. From Table 2.1, it can be observed that the vibration frequencies obtained from the simplified 3D-FE model are in very good agreement with those obtained from the sophisticated 3D-FE model and from the full aeroelastic model.



c) d)
Figure 2.10 Vibration modes obtained based on a simplified 3D-FE model.

2.2 Procedure to calculate responses to wind load based on the frequency domain approach

2.2.1 Basic equations to estimate responses to winds based on random vibration theory

The theoretical basis for estimating the bridge response subjected to the wind load is well-established and presented in Davenport (1962, 1966, 1981, 1983), Simiu and Scanlan (1996), and Strømmen (2010). The wind load on bridges could be classified as time-averaged static, buffeting, and aeroelastic forces. The treatment of the static force is straightforward. The buffeting forces are due to the spatiotemporally varying winds, and the aeroelastic forces are caused by the interaction of the wind and the oscillation of the bridge. The drag force $D(t)$, lift force $L(t)$, and pitching moment $M(t)$, due to wind can be written as (Simiu and Scanlan 1996),

$$D(t) = D_s + D_b(t) + D_{ae}(t), \quad (2.1a)$$

$$L(t) = L_s + L_b(t) + L_{ae}(t), \quad (2.1b)$$

and,

$$M(t) = M_s + M_b(t) + M_{ae}(t), \quad (2.1c)$$

where D , L , and M denote the drag force, lift force, and pitching moment, and s , b , and ae are the subscripts for the time-averaged static, buffeting, and aeroelastic forces. The static forces for a unit length, and characteristic dimension B , are:

$$D_s = \rho U^2 C_D B / 2, \quad (2.2a)$$

$$L_s = \rho U^2 C_L B / 2, \quad (2.2b)$$

and,

$$M_s = \rho U^2 C_M B^2 / 2 \quad (2.2c)$$

where ρ is the air mass density; U , representing $U(z)$, and denotes the time-averaged mean wind velocity at the elevation of the bridge deck z (m); C_D , C_L , C_M , and α are the set of coefficients and the incidence wind angle of attack. The buffeting forces are defined as (see Chen et al. (2009)),

$$D_b(t) = D_s \times \left[\frac{2u(t)}{U} + \frac{C'_D - C_L}{C_D} \times \frac{w(t)}{U} \right], \quad (2.3a)$$

$$L_b(t) = L_s \times \left[\frac{2u(t)}{U} + \frac{C'_L + C_D}{C_L} \times \frac{w(t)}{U} \right], \quad (2.3b)$$

and,

$$M_s(t) = -M_s \times \left[\frac{2u(t)}{U} + \frac{C'_M}{C_M} \times \frac{w(t)}{U} \right], \quad (2.3c)$$

where $u(t)$ and $w(t)$ are the fluctuating wind speeds along the mean wind direction and perpendicular to the mean wind direction; C'_D , C'_L and C'_M are used as short notations for the derivatives of C_D , C_L , and C_M with respect to α . Further, based on the quasi-steady theory (Davenport 1966) (see also Chen et al. (2009)), the aeroelastic forces per unit span in the global axes can be written as,

$$D_{ae}(t) = \frac{1}{2}\rho U^2 B \left[-C_D \frac{\dot{p}(t)}{U} - (C'_D - C_L) \frac{\dot{h}(t)}{U} + \eta B (C'_D - C_L) \frac{\dot{\alpha}}{U} - C'_D \alpha \right] \quad (2.4a)$$

$$L_{ae}(t) = \frac{1}{2}\rho U^2 B \left[-C_L \frac{\dot{p}(t)}{U} - (C'_L + C_D) \frac{\dot{h}(t)}{U} + \eta B (C'_L + C_D) \frac{\dot{\alpha}}{U} - C'_L \alpha \right] \quad (2.4b)$$

and,

$$M_{ae}(t) = \frac{1}{2}\rho U^2 B^2 \left[C_M \frac{\dot{p}(t)}{U} + C'_M \frac{\dot{h}(t)}{U} - \eta B C'_M \frac{\dot{\alpha}}{U} + C'_M \alpha \right] \quad (2.4c)$$

where $\dot{p}(t)$, $\dot{h}(t)$, $\dot{\alpha}$ are the deck velocities in the horizontal, vertical, and rotational directions, respectively, and η is the coefficient that specifies as a fraction of the girder width, the distance between the aerodynamic and shear center.

To evaluate the bridge responses to wind, it is considered that the bridge can be adequately represented by the simplified 3D-FE model, and the equation of motion is expressed by,

$$M\ddot{X} + C\dot{X} + KX = F_s + F_b + F_{ae} \quad (2.5)$$

where \mathbf{M} , \mathbf{C} , and \mathbf{K} are the global mass, damping, and stiffness matrices; \mathbf{X} , $\dot{\mathbf{X}}$ and $\ddot{\mathbf{X}}$ are the nodal displacement, velocity, and acceleration vectors; \mathbf{F} with the subscripts s , b , and ae are the static, buffeting, and aeroelastic forces, respectively. The aeroelastic forces in the global axes can be expressed in the following matrix form,

$$F_{ae} = K_{ae}X + C_{ae}\dot{X} \quad (2.6)$$

By substituting Eq. (2.6) into Eq. (2.5) and re-arrange terms, the equation of motion is,

$$M\ddot{X} + (C - C_{ae})\dot{X} + (K - K_{ae})X = F_s + F_b \quad (2.7)$$

Note that for the analysis, it is considered that Rayleigh damping is applicable, and \mathbf{C} and \mathbf{C}_{ae} are replaced by $\bar{\mathbf{C}} = \alpha_{Damping}M + \beta_{Damping}(K - K_{ae})$ and $\bar{\mathbf{C}}_{ae} = \mathbf{C}_{ae} - \beta_{Damping}K_{ae}$, where $\alpha_{Damping}$ and $\beta_{Damping}$ are the proportionality coefficients for Rayleigh damping. Eq. (2.7) indicates that the system could be nonlinear if \mathbf{K}_{ae} and \mathbf{C}_{ae} are functions of displacement and velocity. However, if \mathbf{K}_{ae} and \mathbf{C}_{ae} are assumed to be constant, the system is linear. For simplicity, this approximation is considered for the numerical analysis in the following. Moreover, it is considered that one could estimate the static responses by considering the time-averaged mean wind speed and the gravity load. This allows one to apply these two forces to the structure first and to obtain the static equilibrium. The buffeting force and aeroelastic force are then considered to obtain the dynamic responses by solving,

$$M\ddot{X} + (\bar{\mathbf{C}} - \bar{\mathbf{C}}_{ae})\dot{X} + (K - K_{ae})X = F_b \quad (2.8)$$

It must be emphasized that the responses obtained based on Eq. (2.8) are the responses with the static load and mean wind effect removed. In this chapter, the statistics of the peak responses due to buffeting and aerodynamic forces (i.e., solution of Eq. (2.8)) are evaluated based on the frequency-domain approach (Simiu and Scanlan 1996; Chen et al. 2009; Strømmen 2010). The details on the evaluation of the buffeting and aerodynamic forces on the bridge, as well as the use of the frequency-domain procedure, are described in the following sections.

2.2.2 Characteristics of wind and Buffeting force

As shown in Eq. (2.3), the buffeting force is due to the fluctuating wind which is a stochastic process and is often characterized using the concept of the power spectral density function (Simiu and Scanlan 1996). One of the commonly used PSD functions is the one proposed by Kaimal et al. (1972). The Kaimal PSD functions of $u(t)$ and $w(t)$ can be written as (Simiu and Scanlan 1996),

$$\frac{f S_u(z, f)}{u_*^2} = \frac{200\zeta}{(1+50\zeta)^{5/3}}, \quad (2.9a)$$

and

$$\frac{f S_w(z, f)}{u_*^2} = \frac{3.36 \zeta}{1 + 10 \zeta^{5/3}} \quad (2.9b)$$

where $\zeta (= fz/U)$ is the Monin coordinate or reduced frequency, f the frequency in Hz; z the height above the ground surface, and u_* the shear friction velocity. The use of these equations results in that the standard deviation of $u(t)$, σ_u , equals $\sqrt{6}u_*$, and the standard deviation of $w(t)$, σ_w , equals $\sqrt{1.67}u_*$. By definition, σ_u is the product of the along-wind turbulence intensity (i.e., coefficient of variation) and the mean wind speed.

The fluctuating wind speed varies in time and space. The cross power spectral density (XPSD) function of $u(t)$ and $w(t)$ at two points \mathbf{p}_i and \mathbf{p}_j along the bridge deck can be used to describe such a spatial correlation of $u(t)$ and of $w(t)$ along the bridge deck. The XPSD function can be expressed as (Davenport, 1968),

$$S_{uu}(p_i, p_j, f) = \sqrt{S_u(z_i, f)S_u(z_j, f)} \exp\left(-\frac{f}{\bar{U}}\left(C_y^2(y_i - y_j)^2 + C_z^2(z_i - z_j)^2\right)^{\frac{1}{2}}\right), \quad (2.10a)$$

and,

$$S_{ww}(p_i, p_j, f) = \sqrt{S_w(z_i, f)S_w(z_j, f)} \exp\left(-\frac{f}{\bar{U}}C_w|y_i - y_j|\right), \quad (2.10b)$$

where y_i and y_j , z_i and z_j are the coordinates of two points \mathbf{p}_i and \mathbf{p}_j ; C_y and C_z are the exponential decay coefficients for the coherence of along-wind in the directions of y -axis and z -axis, respectively; C_w is the exponential decay coefficient for the spanwise coherence of cross-wind; \bar{U} are the average of the mean wind speed between \mathbf{p}_i and \mathbf{p}_j . For the numerical analysis to be presented, $C_y=16$, $C_z=10$, and $C_w=8$ are considered (Simiu and Yeo, 2019). For the finite element modelling, since the deck element is small, $\sqrt{S_u(z_i, f)S_u(z_j, f)}$ and $\sqrt{S_w(z_i, f)S_w(z_j, f)}$ could be approximated by $S_u(\bar{z}, f)$ and $S_w(\bar{z}, f)$, respectively, where \bar{z} equals the average value of z_i and z_j . Similar to many applications (Simiu and Scanlan 1996; Strømmen 2010), the coherence between $u(t)$ and $w(t)$ is neglected in the present study.

The mean wind speed at a spatial point is required in defining the PSD functions. If a constant mean wind speed is considered for the entire bridge, the wind field is a homogeneous random field. However, because of the along height varying wind speed, as well as the topographic effect, the mean wind speed experienced by the bridge may not be treated as a constant value. In such cases, the spatially-varying mean wind speed leads to the wind field being a nonhomogeneous random field.

To obtain the buffeting force on the nodes of elements of the FE model, the mean wind speed profile of the bridge needs to be defined. For the Baluarte Bridge, the horizontal wind speed, which varies in the longitudinal direction of the bridge at the main deck height, was reported in King and Kong (2010). This variation is considered in the present study to define the spatially varying time-averaged mean wind speed. In order to define a spatially-varying mean wind speed, considering that the horizontally varying mean wind speed for the Baluarte bridge is significantly affected by the topography, it is considered that the power-law model (Davenport 1965) can be adopted. The along height mean wind speed is considered to be calculated using,

$$U(x, z) = U(x, z_{deck}(x)) \times \left(\frac{z}{z_{deck}(x)} \right)^{\alpha(x)} \quad (2.11)$$

where $U(x, z_{deck}(x))$ represents the wind speed at a reference height (i.e., at the deck height $z_{deck}(x)$), which depends on the coordinate x , x is measured from the left pylon to the right pylon at the deck height (see Figures 2.2 and 2.11), $\alpha(x)$ is the power-law coefficient that depends on the upstream terrain condition, usually taken equal to 0.16 for open country terrain (NRC 2010). Based on the wind tunnel test results, regression analysis results indicate that $\alpha(0)$ equal to 0.180 and $\alpha(520)$ equal to 0.198 could be adequate. It was assumed that the power-law exponent at the point near the middle of the two pylons (i.e., at the point where the depth from the deck to the bottom of the canyon equals 390 m (see Figures 2.2 and 2.11) equals 0.15 (i.e., $\alpha(260) = 0.15$)). To determine $U(x, z_{deck}(x))$, the mean wind speed profile along the bridge deck determined from the wind tunnel test and normalized with respect to U_{mid} was employed, where this normalized wind profile represented by $r_U(x, z_{deck}(x)) = U(x, z_{deck}(x))/U_{mid}$ with $U_{mid} =$

$U_{mid}(260, z_{deck}(260))$ is also shown in Figure 2.11 and U_{mid} represents the reference hourly-mean wind speed at the “middle” span. A mean wind speed surface based on the above by assuming $U_{mid} = 30$ m/s is illustrated in Figure 2.11 as well.

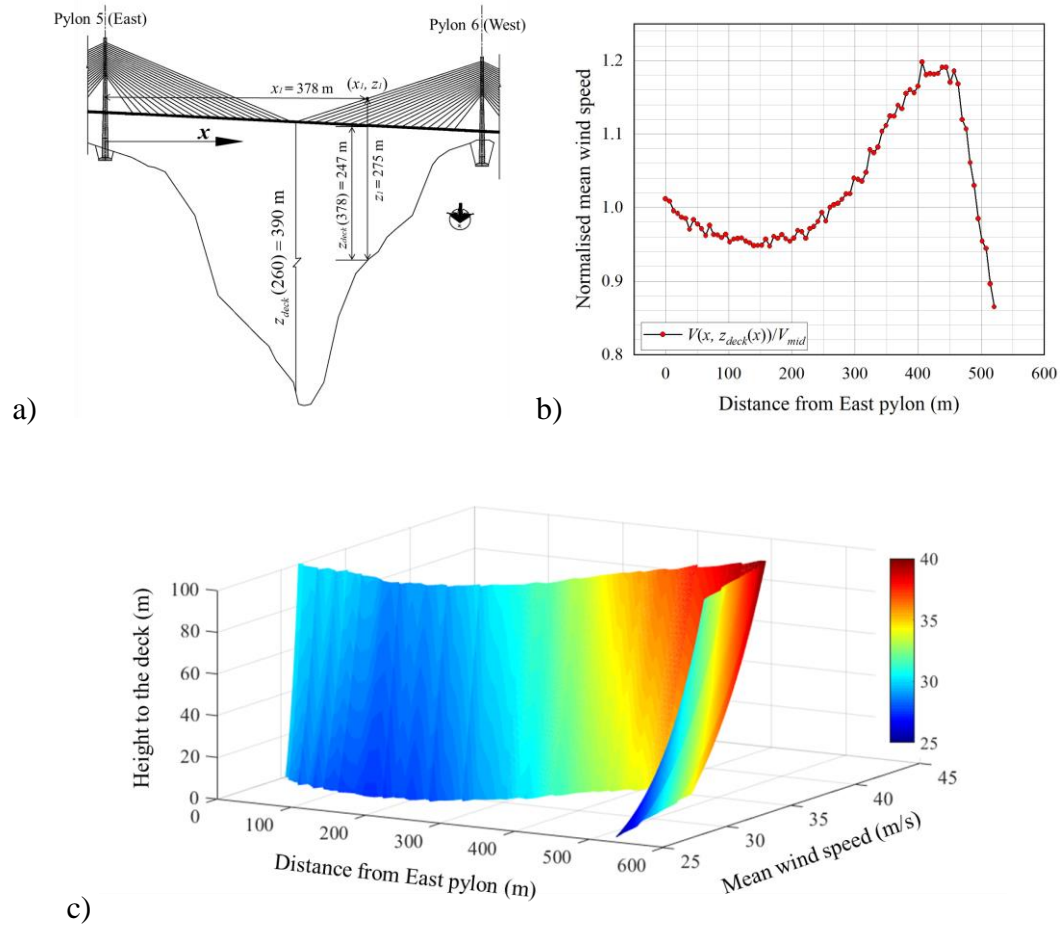


Figure 2.11 Coordinates and the mean wind profile for Baluarte bridge: a). Defined coordinates; b) Horizontal mean wind speed profile $r_U(x, z_{deck}(x))$ along the deck; c) Mean wind speed surface.

To take into account the buffeting forces acting on the bridge deck, consider that the bridge deck can be modelled using the 2-node beam elements (i.e., 3-D 2-node line element with rotational degrees of freedom in ANSYS) as shown in Figure 2.12. It is considered that the distributed buffeting force acting along the length of the element in the direction of the bridge spanning can be approximated by the equivalent nodal forces, as shown in

Figure 2.12. By assuming that the pressure coefficients and the fluctuating wind velocities within an element can be represented by their values at the midpoint of the element, these forces can be expressed as (Hua et al. 2007; Hu 2009),

$$F_b^e = E_b^e q^e \quad (2.12)$$

where F_b^e denotes the nodal forces on the deck, $q^e = [u^e(t), w^e(t)]^T$ denotes the fluctuating along and crosswind velocities at the midpoint of the deck element, and E_b^e is given by (Sun et al. 1999),

$$E_b^e = \begin{bmatrix} 0 & C_1 C_D \frac{l}{U} & C_1 C_L \frac{l}{U} & C_2 C_M \frac{l}{U} & -\frac{C_1 C_L l^2}{6 U} & \frac{C_1 C_D l}{6 U} \\ 0 & \frac{C_1 C'_D l}{2 U} & \frac{C_1 (C'_L + C_D) l}{2 U} & \frac{C_2 C'_M l}{2 U} & -\frac{C_1 (C'_L + C_D) l^2}{12 U} & \frac{C_1 C'_D l^2}{12 U} \\ 0 & C_1 C_D \frac{l}{U} & C_1 C_L \frac{l}{U} & C_2 C_M \frac{l}{U} & \frac{C_1 C_L l^2}{6 U} & -\frac{C_1 C_D l}{6 U} \\ 0 & \frac{C_1 C'_D l}{2 U} & \frac{C_1 (C'_L + C_D) l}{2 U} & \frac{C_2 C'_M l}{2 U} & \frac{C_1 (C'_L + C_D) l^2}{12 U} & -\frac{C_1 C'_D l^2}{12 U} \end{bmatrix}^T \quad (2.13a)$$

where $C_1 = \rho U^2 B / 2$, $C_2 = \rho U^2 B^2 / 2$, and l is the length of the element.

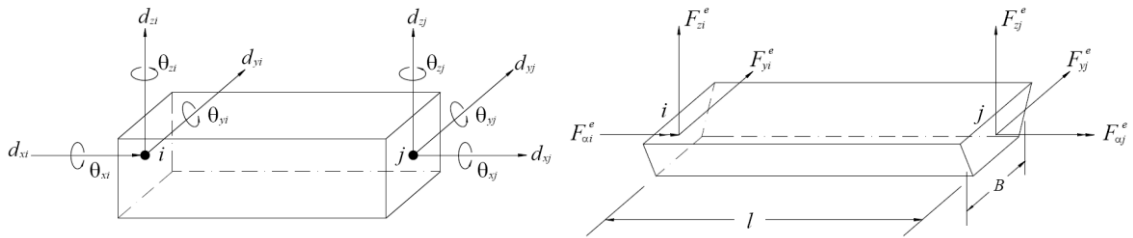


Figure 2.12 Illustration and adopted displacement notations for the two-node beam element, and the lumped forces on the beam element (after Hu 2009).

For the buffeting forces acting on the bridge pylon, consider that the 2-node beam elements used for modelling the deck can also be employed for modelling the vertical pylon. Notice that the wind angle of attack here is the angle of normal incident wind referring to the vertical plane of the pylon segment. By assuming that the aerostatic

coefficients are independent of the wind angle of attack, i.e., the derivatives of the coefficients equal to zero, E_b^e for the bridge pylon, denoted as $E_{b,p}^e$. can be derived as,

$$E_{b,p}^e = \begin{bmatrix} 0 & C_{1,p}C_{D,p} \frac{l}{U} & C_{1,p}C_{L,p} \frac{l}{U} & C_{2,p}C_{M,p} \frac{l}{U} & -\frac{C_{1,p}C_{L,p}l^2}{6U} & \frac{C_{1,p}C_{D,p}l}{6U} \\ 0 & 0 & \frac{C_{1,p}C_{D,p}l}{2U} & 0 & -\frac{C_{1,p}C_{D,p}l^2}{12U} & 0 \\ 0 & C_{1,p}C_{D,p} \frac{l}{U} & C_{1,p}C_{L,p} \frac{l}{U} & C_{2,p}C_{M,p} \frac{l}{U} & \frac{C_{1,p}C_{L,p}l^2}{6U} & -\frac{C_{1,p}C_{D,p}l}{6U} \\ 0 & 0 & \frac{C_{1,p}C_{D,p}l}{2U} & 0 & \frac{C_{1,p}C_{D,p}l^2}{12U} & 0 \end{bmatrix}^T \quad (2.13b)$$

where the subscript p is used to denote the coefficients for the pylon and l is the length of the vertical element.

Further, to take into account the buffeting forces acting on the bridge cables, which are modelled as a 2-node link element with three translational degrees of freedoms of each node, E_b^e for the bridge cable, termed as $E_{b,c}^e$, can be derived as,

$$E_{b,c}^e = \begin{bmatrix} 0 & C_{1,c}C_{D,c} \frac{l}{U} & C_{1,c}C_{L,c} \frac{l}{U} & 0 & C_{1,c}C_{D,c} \frac{l}{U} & C_{1,c}C_{L,c} \frac{l}{U} \end{bmatrix}^T \quad (2.13c)$$

where the subscript c is used to denote the coefficients for the cable and l is the length of the link element representing the cable. Note that for assembling the nodal force matrix, $E_{b,c}^e$ is to be extended into a 2×12 matrix by setting zeros to the elements corresponding to the rotational degrees of freedoms in the matrix.

The nodal forces given in the local coordinate for the elements representing deck, pylons and cables, denoted as F_b^e , are converted into the global coordinate system through the $6(n+1) \times 12$ coordinate transformation matrix T^e (n denotes the number of 2-noded elements with six degrees of freedoms at each node), and the forces in the global coordinate represented by $F_B^{e,s}$ are given by (Hua et al. 2007; Hu 2009; Hu et al. 2012),

$$F_B^{e,s} = T^e F_b^e \quad (2.14)$$

The transformation matrix T^e is derived as,

$$(\mathbf{T}^e)_{Element=k \rightarrow Node(i,j)} = \begin{bmatrix} \mathbf{0}_{6 \times 6} & \mathbf{0}_{6 \times 6} & \cdots & I_{6 \times 6(i)} & \cdots & \mathbf{0}_{6 \times 6(j)} & \cdots & \mathbf{0}_{6 \times 6} \\ \mathbf{0}_{6 \times 6} & \mathbf{0}_{6 \times 6} & \cdots & \mathbf{0}_{6 \times 6(i)} & \cdots & I_{6 \times 6(j)} & \cdots & \mathbf{0}_{6 \times 6} \end{bmatrix}^T \quad (2.15)$$

where $I_{6 \times 6}$ is the 6×6 identity matrix and the extra subscript denote the position of the submatrix, $\mathbf{0}_{6 \times 6}$ is the 6×6 zero matrix and the extra subscript denotes the position of the submatrix.

By assembling the buffeting force vector $\mathbf{F}_B^{e,S}$ for all the elements, the global buffeting force vector for the bridge deck, pylons, and cables \mathbf{F}_B is,

$$\mathbf{F}_B = \sum_{k=1}^n (\mathbf{T}^e \mathbf{F}_B^e)_k = \sum_{k=1}^n (\mathbf{T}^e \mathbf{E}_B^e \mathbf{q}^e)_k = \mathbf{T} \mathbf{P} \quad (2.16)$$

where $\mathbf{T} = [(\mathbf{T}^e)_1, (\mathbf{T}^e)_2, \dots, (\mathbf{T}^e)_k, \dots, (\mathbf{T}^e)_n]$,

$\mathbf{P}^T = [(\mathbf{E}_B^e \mathbf{q}^e)_1, (\mathbf{E}_B^e \mathbf{q}^e)_2, \dots, (\mathbf{E}_B^e \mathbf{q}^e)_k, \dots, (\mathbf{E}_B^e \mathbf{q}^e)_n]^T$, and the subscript k denotes the k -th element; \mathbf{E}_B^e is the element force matrix assembled by using \mathbf{E}_b^e , $\mathbf{E}_{b,p}^e$, and $\mathbf{E}_{b,c}^e$.

Since the displacements of the element $u^e(t)$ and $w^e(t)$ (i.e., $u(t)$ and $w(t)$ for the considered element) are stochastic processes that are characterized by their corresponding PSD functions, \mathbf{F}_b represents a vector of stochastic processes for given \mathbf{T}^e and \mathbf{E}_B^e . It can be shown that the spectral density function matrix of \mathbf{F}_B , $\mathbf{S}_{FF}(f)$, can be expressed as (Sun et al. 1999; Hua et al. 2007; Hu 2009) (note that the frequency in here is represented in Hz while that used in Hu (2009) is expressed in rad/s),

$$\mathbf{S}_{FF}(f) = \mathbf{T} \begin{bmatrix} \mathbf{S}_{P_1 P_1}^e(f) & \mathbf{S}_{P_1 P_2}^e(f) & \cdots & \mathbf{S}_{P_1 P_n}^e(f) \\ \mathbf{S}_{P_2 P_1}^e(f) & \mathbf{S}_{P_2 P_2}^e(f) & \cdots & \mathbf{S}_{P_2 P_n}^e(f) \\ \vdots & \vdots & \ddots & \vdots \\ \mathbf{S}_{P_n P_1}^e(f) & \mathbf{S}_{P_n P_2}^e(f) & \cdots & \mathbf{S}_{P_n P_n}^e(f) \end{bmatrix} \mathbf{T}^T \quad (2.17)$$

where the submatrix $\mathbf{S}_{P_i P_j}^e(f)$ representing the 12×12 cross-spectral density function matrix of the nodal forces on the i -th element and the j -th element, and is given by

$$\mathbf{S}_{P_i P_j}^e(f) = (\mathbf{E}_B^e)_i \mathbf{S}_{q_i q_j}^e(f) [(\mathbf{E}_B^e)_j]^T \quad (2.18)$$

in which,

$$\mathbf{S}_{q_i q_j}^e(f) = \begin{bmatrix} S_{uu}(p_i, p_j, f) & S_{uw}(p_i, p_j, f) \\ S_{wu}(p_i, p_j, f) & S_{ww}(p_i, p_j, f) \end{bmatrix} \quad (2.19)$$

where \mathbf{p}_i and \mathbf{p}_j are the midpoints of the i -th and j -th elements; $S_{uu}(p_i, p_j, f)$, and $S_{ww}(p_i, p_j, f)$ are defined in Eqs. (2.10). As mentioned earlier $S_{uw}(p_i, p_j, f)$ and $S_{wu}(p_i, p_j, f)$ are assumed to be zero.

2.2.3 Modelling aeroelastic forces and analysis procedure

To take into account the aeroelastic forces in the deck, the 2-node matrix element MATRIX27 in ANSYS is employed for assembling the global aeroelastic stiffness and damping matrices as indicated in Eq. (2.7) and (2.8). The coordinate system of the element used to assemble the matrices is illustrated in Fig 2.13. Following Chen et al. (2009), element E2 is employed to model aerodynamic stiffness, and element E3 to model aerodynamic damping. The nodes I and J are the shared nodes for the beam element and the two matrix elements.

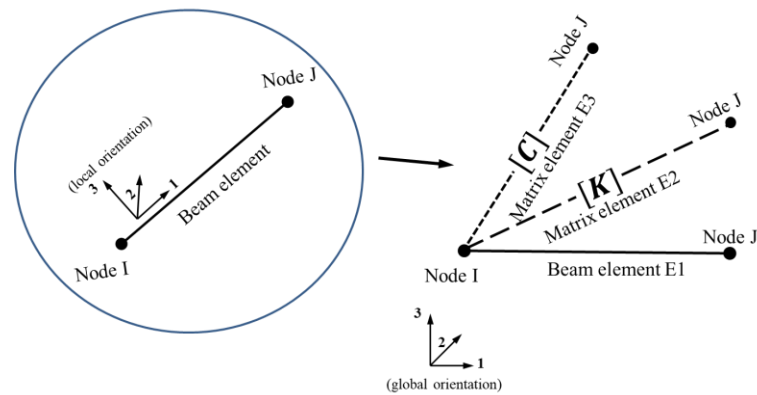


Figure 2.8 Schematic of the modelling matrix element.

The constructed aerodynamic stiffness and damping matrices for the element are (Chen et al. 2009),

$$K_{ae}^e = \frac{1}{2}\rho UBL \begin{bmatrix} 0 & 0 & 0 & 0 & 0 & 0 & 0 & 0 & 0 & 0 & 0 & 0 \\ 0 & 0 & 0 & \frac{7}{20}a & 0 & 0 & 0 & 0 & 0 & \frac{3}{20}a & 0 & 0 \\ 0 & 0 & 0 & \frac{7}{20}b & 0 & 0 & 0 & 0 & 0 & \frac{3}{20}b & 0 & 0 \\ 0 & 0 & 0 & \frac{B}{3}c & 0 & 0 & 0 & 0 & 0 & \frac{B}{6}c & 0 & 0 \\ 0 & 0 & 0 & \frac{L}{20}b & 0 & 0 & 0 & 0 & 0 & \frac{L}{30}b & 0 & 0 \\ 0 & 0 & 0 & \frac{L}{20}a & 0 & 0 & 0 & 0 & 0 & \frac{L}{30}a & 0 & 0 \\ 0 & 0 & 0 & 0 & 0 & 0 & 0 & 0 & 0 & 0 & 0 & 0 \\ 0 & 0 & 0 & \frac{3}{20}a & 0 & 0 & 0 & 0 & 0 & \frac{7}{20}a & 0 & 0 \\ 0 & 0 & 0 & \frac{3}{20}a & 0 & 0 & 0 & 0 & 0 & \frac{7}{20}b & 0 & 0 \\ 0 & 0 & 0 & \frac{B}{6}c & 0 & 0 & 0 & 0 & 0 & \frac{B}{3}c & 0 & 0 \\ 0 & 0 & 0 & \frac{-L}{30}b & 0 & 0 & 0 & 0 & 0 & \frac{-L}{20}b & 0 & 0 \\ 0 & 0 & 0 & \frac{-L}{30}a & 0 & 0 & 0 & 0 & 0 & \frac{-L}{20}a & 0 & 0 \end{bmatrix} \quad (2.20)$$

$$C_{ae}^e = \frac{1}{2}\rho UBL \begin{bmatrix} 0 & 0 & 0 & 0 & 0 & 0 & 0 & 0 & 0 & 0 & 0 & 0 \\ 0 & \frac{13}{35}d & \frac{13}{35}g & \frac{7}{20}j & \frac{11L}{210}g & \frac{11L}{210}d & 0 & \frac{9}{70}d & \frac{9}{70}g & \frac{3}{20}j & \frac{-13L}{420}g & \frac{-13L}{420}d \\ 0 & \frac{13}{35}e & \frac{13}{35}h & \frac{7}{20}k & \frac{11L}{210}h & \frac{11L}{210}e & 0 & \frac{9}{70}e & \frac{9}{70}h & \frac{3}{20}k & \frac{-13L}{420}h & \frac{-13L}{420}e \\ 0 & \frac{7B}{20}f & \frac{7B}{20}i & \frac{B}{3}m & \frac{BL}{20}i & \frac{BL}{20}f & 0 & \frac{3B}{20}f & \frac{3B}{20}i & \frac{B}{6}m & \frac{-LB}{30}i & \frac{-LB}{30}f \\ 0 & \frac{11L}{210}e & \frac{11L}{210}h & \frac{L}{20}k & \frac{L^2}{105}h & \frac{L^2}{105}e & 0 & \frac{13L}{420}e & \frac{13L}{420}h & \frac{L}{30}k & \frac{-L^2}{140}h & \frac{-L^2}{140}e \\ 0 & \frac{11L}{210}d & \frac{11L}{210}g & \frac{L}{20}j & \frac{L^2}{105}g & \frac{L^2}{105}d & 0 & \frac{13L}{420}d & \frac{13L}{420}g & \frac{L}{30}j & \frac{-L^2}{140}g & \frac{-L^2}{140}d \\ 0 & 0 & 0 & 0 & 0 & 0 & 0 & 0 & 0 & 0 & 0 & 0 \\ 0 & \frac{9}{70}d & \frac{9}{70}g & \frac{3}{20}j & \frac{13L}{420}g & \frac{13L}{420}d & 0 & \frac{13}{35}d & \frac{13}{35}g & \frac{7}{20}j & \frac{-11L}{210}g & \frac{-11L}{210}d \\ 0 & \frac{9}{70}e & \frac{9}{70}h & \frac{3}{20}k & \frac{13L}{420}h & \frac{13L}{420}e & 0 & \frac{13}{35}e & \frac{13}{35}h & \frac{7}{20}k & \frac{-11L}{210}h & \frac{-11L}{210}e \\ 0 & \frac{3B}{20}f & \frac{3B}{20}i & \frac{B}{6}m & \frac{BL}{30}i & \frac{BL}{30}f & 0 & \frac{7B}{20}f & \frac{7B}{20}i & \frac{B}{3}m & \frac{-BL}{20}i & \frac{-BL}{20}f \\ 0 & \frac{-13L}{420}e & \frac{-13L}{420}h & \frac{-L}{30}j & \frac{-L^2}{140}h & \frac{-L^2}{140}e & 0 & \frac{-11L}{210}e & \frac{-11L}{210}h & \frac{-L}{20}k & \frac{L^2}{105}h & \frac{L^2}{105}e \\ 0 & \frac{-13L}{420}d & \frac{-13L}{420}g & \frac{-L}{30}j & \frac{-L^2}{140}g & \frac{-L^2}{140}d & 0 & \frac{-11L}{210}d & \frac{-11L}{210}g & \frac{-L}{20}j & \frac{L^2}{105}g & \frac{L^2}{105}d \end{bmatrix} \quad (2.21)$$

where $a = -C'_D$; $b = -C'_L$; $c = C'_M$; $d = -2C_D$; $e = -2C_L$; $f = 2C_M$; $g = -(C'_D - C_L)$; $h = -(C'_L + C_D)$; $i = -C'_M$; $j = -\eta B(C'_D - C_L)$; $k = -\eta B(C'_L + C_D)$; $m = -\eta BC'_M$.

Based on the assembled stiffness matrix and damping matrix, including the stiffness and damping matrices due to aeroelastic force, and the wind load due to buffeting force, Eq. (2.8) is completely defined. To solve Eq. (2.8) based on the frequency-domain approach, it is noted that the spectral density matrix of the buffeting force $\mathbf{S}_{FF}(f)$ can be decomposed as,

$$\mathbf{S}_{FF}(f) = \mathbf{L}^*(f)\mathbf{D}(f)\mathbf{L}^T(f) \quad (2.22a)$$

where $\mathbf{L}(f)$ is a decomposed matrix obtained by using Cholesky decomposition or eigenvalue decomposition (if Cholesky decomposition is used $\mathbf{L}(f)$ is a low triangular matrix; if the eigenvalue decomposition is used $\mathbf{L}(f)$ contains orthonormal vectors), $\mathbf{D}(f)$ is a diagonal matrix, and the superscript $*$ denotes the complex conjugate. Note that since some of the degrees of freedom are restrained, they do not take loads. The matrix $\mathbf{S}_{FF}(f)$ contains rows and columns of zeros associated with those degrees of freedom. In such a case, the rows and columns with zeros need to be removed to decompose the matrix. Once the decomposition is completed, the matrices should be re-arranged such that Eq. (2.22a) holds.

Let $\mathbf{L}_k(f)$ denote the k -th column of $\mathbf{L}(f)$ and $d_k(f)$ denote the k -th diagonal element of $\mathbf{D}(f)$. $\mathbf{S}_{FF}(f)$ shown in Eq. (2.17) can be re-written as,

$$\mathbf{S}_{FF}(f) = \sum_{k=1}^m d_k(f) \mathbf{L}_k^*(f) \mathbf{L}_k^T(f) \quad (2.22b)$$

where m is the size of the matrix $\mathbf{D}(f)$. Then the spectral density function of the response \mathbf{X} , $\mathbf{S}_{XX}(f)$, is given by (Sun et al. 1999),

$$\mathbf{S}_{XX}(f) = \sum_{k=1}^m d_k(f) X_k^*(f) X_k^T(f) \quad (2.23)$$

where $X_k(f) = \mathbf{H}(if) \mathbf{f}_k(f)$, $\mathbf{H}(if) = [-(2\pi f)^2 \mathbf{M} + i(2\pi f)(\bar{\mathbf{C}} - \bar{\mathbf{C}}_{ae}) + (\mathbf{K} - \mathbf{K}_{ae})]^{-1}$ is the transfer function for the bridge system obtained based on Eq. (2.8), and $\mathbf{f}_k(f, t) = \mathbf{L}_k(f) \exp(i2\pi ft)$ for $k=1, 2, \dots, m$. The stochastic response \mathbf{X} is then completely characterized by its PSD matrix (including the cross-terms).

In summary, the steps to determine the PSD function of the responses \mathbf{X} are:

- 1) Evaluate the static response due to gravity load and the mean wind speed;
- 2) Assemble the global aeroelastic stiffness and damping matrices (see Eqs. (2.20) and (2.21)) and include them in defining the stiffness and damping coefficient matrix (see Eq. (2.8));
- 2) Establish the PSD matrix for the buffeting force by considering the elements used to model the structure (most importantly, elements used to model the deck and the cables)

(see Eq. (2.22a). Decompose the PSD matrix of the buffeting force for a series of frequencies ranging from a lower bound to an upper bound frequency bound (e.g., 0.003 to 0.6 Hz) with an increment of 0.005 Hz (see Eq. (2.22b));

- 3) For each considered frequency of the buffeting load, carry out structural analysis subjected to $\mathbf{f}_k(f, t) = \mathbf{L}_k(f) \exp(i2\pi ft)$ (i.e., subjected to harmonic excitations) and evaluate the PSD matrix of \mathbf{X} , $\mathbf{S}_{XX}(f)$ (see Eq. (2.23)).

Consider a response of interest r such as the bridge midspan horizontal, vertical or torsional displacement. The PSD function of r , denoted as $S_r(f)$, can be identified from $\mathbf{S}_{XX}(f)$. The obtained $S_r(f)$ can then be used to evaluate the statistics of peak response or mean peak response of r due to the mean and fluctuating winds. According to Davenport (1964), the probability distribution of peak response of r over a duration T (s), $F(\eta_p)$, can be approximated by the Gumbel probability distribution,

$$F(\eta_p) = \exp\left(-\exp\left(-\frac{\sqrt{2 \ln(v_0^+ T)}}{\sigma_r}(\eta_p - \bar{r} - \sigma_r \sqrt{2 \ln(v_0^+ T)})\right)\right) \quad (2.24)$$

where \bar{r} is the response due to mean wind speed, η_p is the peak response, $v_0^+ = \sigma_{\dot{r}}/\sigma_r$ the zero up-crossing rate, σ_r and $\sigma_{\dot{r}}$ are the standard deviations of r and of its temporal derivative, respectively. σ_r and $\sigma_{\dot{r}}$ can be calculated using,

$$\sigma_r^2 = \int_0^\infty S_r(f) df, \quad (2.25a)$$

and,

$$\sigma_{\dot{r}}^2 = \int_0^\infty (2\pi f)^2 S_r(f) df. \quad (2.25b)$$

The mean peak response (i.e., the mean of η_p), m_η , based on the Gumbel probability distribution shown in Eq. (2.23) is,

$$m_\eta = \bar{r} + g_p \sigma_r, \quad (2.26)$$

where $g_p = \sqrt{2 \ln(v_0^+ T)} + 0.577 / \sqrt{2 \ln(v_0^+ T)}$ is known as the peak factor, and $G_T = 1 + v_r g_p$ is known as the gust factor, in which v_r equals σ_r / \bar{r} , representing the coefficient of variation of the response.

2.3 Numerical analysis results and comparison

For the analysis, ρ is considered equal to 1.2929 kg/m^3 . This value is used for Canadian codified structural design. It is acknowledged that this value could be high for Mexico in general, but could be a conservative assumption for wind load. The values of C_D , C_L and C_M for the steel deck and concrete deck are already shown in Table 2.2. For the pylons, $C_{D,p} = 1.4$ suggested by Canadian Highway and Bridge Design Code (Can/CSA S16-19 2019) is adopted for the analysis, and it is assumed that the buffeting effects due to lifting and bending of the pylons on the response of the main span are negligible. For the cables, $C_{D,c} = 1.2$ and $C_{L,c} = 0.2$ are employed based on the discussion given in the previous sections. The turbulence intensity is considered to be equal to 0.15, which agrees with that considered for carrying out the wind tunnel test, as mentioned earlier.

The values of C'_D , C'_L and C'_M are also given in Table 3.2 for the steel deck and concrete deck. The width of the concrete deck and the width of the steel deck are taken as 22.06 m and 19.76 m, respectively. It is assumed that the wind loads on the side-spans can be neglected. Static analysis is carried out for $U_{mid} = 30$ and 40 m/s , and the corresponding displacements for the mean wind component are shown in Table 2.6. These two values of the mean wind speed were also used by King et al. (2011) for the tests on the BLWTL at UWO. Also shown in Table 2.6 is the displacement obtained based on the wind tunnel tests (King and Kong 2010; King et al. 2010).

The results of the lateral displacement and the vertical displacement at the midspan obtained from the static analysis are compared with the wind tunnel test results (Table 2.6). For the static analysis, first, the gravity load is applied to the bridge, and then the wind load due to mean wind speed is used with the option for large deformation in ANSYS. The comparison indicates that the horizontal displacement obtained by using the simple 3D-FE model developed in the present study compares well to the results from the BLWT.

However, the calculated vertical response differs from that measured from the aeroelastic model in the wind tunnel, especially for $U_{mid} = 40$ m/s. However, since the magnitude of the vertical displacement is so small, no additional adjustment to the developed finite element model is made. This successful comparison validates the FE model at least for the static loads.

Table 2.6 Mean response of the bridge considering static wind loading condition.

U_{mid}	Midspan lateral displacement (m)		Midspan vertical displacement (m)	
	BLWT test	FE model	BLWT test	FE model
30 m/s	0.212	0.237	0.02	0.023
40 m/s	0.364	0.421	0.01	0.009

Based on the above considerations and by using the 3D-FE model, first, the frequency-domain analysis described extensively in the previous sections is carried out for the Baluarte bridge by considering the buffeting force but neglecting the aeroelastic effect. For the analysis, again, first, the gravity load is applied to obtain a deformed structure by considering large deformation. Using the deformed structure, a new bridge configuration and finite element model are defined. For this newly defined bridge, the harmonic analysis option in ANSYS is used to carry out the analysis. This harmonic analysis is repeated by including the fluctuating wind load defined by $\mathbf{L}_k(f)$. The harmonic analysis provides the response (i.e., $X_k(f)$) due to fluctuating wind defined by $\mathbf{L}_k(f)$. Note that the harmonic analysis implicitly assumes that the structure response is linear elastic. $X_k(f)$ is used to obtain the PSD function of the responses, as shown in Eqs. (2.22) and (2.23) for a frequency equal to 0.01 to 0.7 with a frequency increment of 0.02 Hz for the frequency within 0.01 to 0.21 or within 0.5 to 0.7, and 0.01 Hz for frequency within 0.21 to 0.50, respectively.

The obtained PSD functions of the horizontal and vertical displacements at the midspan are shown in Figure 2.14 for $U_{mid} = 30$ m/s and $U_{mid} = 40$ m/s. These PSD functions show a clear peak near the first and second vibration frequencies of the bridge. They have similar looks to the multiplication of the mechanic admittance function and the power spectral density function of the wind force due to fluctuating winds that can be obtained analytically for a linear elastic single-degree-of-freedom system (Simiu and Scanlan 1996). This is surprising, considering that the excitation considered is nonuniform in space (i.e., the mean

wind speed is spatially varying), the fluctuating wind is not fully coherent, and the considered bridge system consists of more than 1500 nodes with many dynamic degrees of freedom. For the horizontal displacement, the peak occurred near 0.25 Hz which is associated with the first vibration modes for the horizontal displacement (see Table 2.1). The PSD function for the vertical displacement exhibits a large peak at 0.30 Hz, which is associated with the first vertical vibration mode (see Table 2.1). The results in Figure 2.14 are shown in the semi-logarithmic paper. This point will be discussed further in terms of the root mean square (RMS) response, shortly.

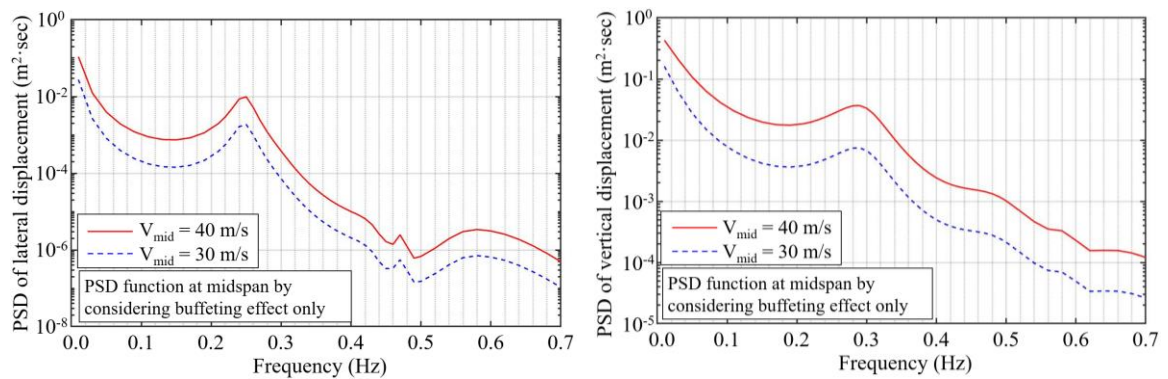


Figure 2.9 PSD functions of the horizontal displacement and vertical displacement at midspan by considering the buffeting effect.

The analysis that is carried out by considering the buffeting alone with the results shown in Figure 2.14 is repeated but considers both the aeroelastic and buffeting effects. The obtained results are presented in Figure 2.15. A comparison of the results presented in Figures 2.14 and 2.15 indicates that the PSD functions for the responses are comparable, and the frequencies where the peak values of PSD functions occur are shifted to a lower frequency, especially for the horizontal displacement. This shift can be explained by noting that the stiffness matrix is modified by considering the aeroelastic effect (see Eq. (2.19)).

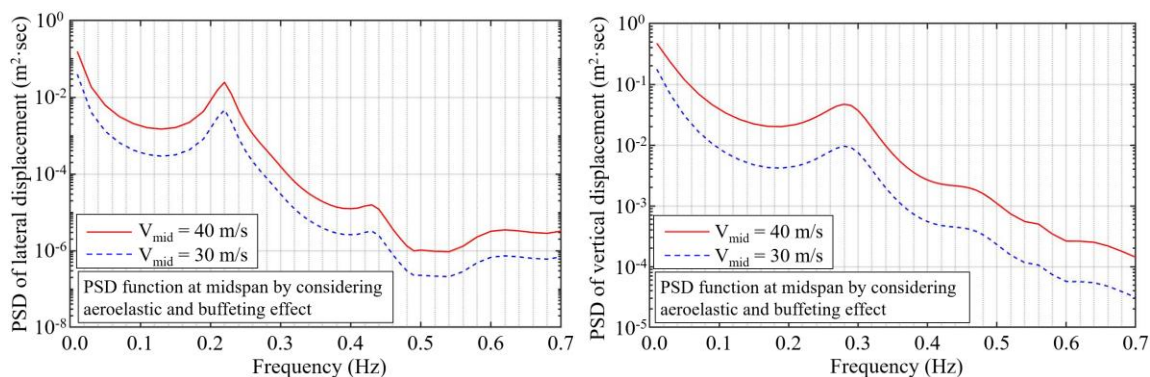


Figure 2.10 PSD function of the horizontal displacement and vertical displacement at midspan by considering the aeroelastic and buffeting effect.

Based on the obtained PSD function shown in Figures 2.14 and 2.15, and Eqs. (2.23) and (2.25), the RMS responses (i.e., horizontal displacement and vertical displacement) at the mid-span are calculated, and the obtained results are compared to the BLWT test results (Table 2.7). The RMS responses obtained by considering the buffeting force alone, are lower than those obtained from the wind tunnel test. The predicted RMS displacements for both horizontal and vertical directions range from 70% to 84% of that obtained from the full aeroelastic model BLWT if a mean wind speed of 30 m/s is considered. The ratios become 79% to 98% for the horizontal displacement and 66% to 71% for the vertical displacement if the mean wind speed of 40 m/s is considered.

An effort is made to find the cause of the discrepancy between the calculated and full aeroelastic model test results. It is possible that the strip assumption, which is the basis of the quasi-steady theory, can underestimate the gust wind response. Chen et al. (2000a) emphasized the importance of unsteady characteristics derived from experimentally measured spanwise coherence of aerodynamic forces. Similarly, Larose and Mann (1998) showed that the pressure field throughout the bridge deck has a higher spanwise correlation than that one derived from wind speeds, and the consideration of the Strip assumption. Some aspects of the study of wind coherence would be treated in Chapter 3 in the time-domain analysis. However, the study of force coherence by carrying out new wind tunnel tests is beyond the scope of this investigation.

As part of a parametric investigation, additional analysis is carried out by varying U_{mid}

from 20 to 45 m/s. The obtained RMS of horizontal and vertical displacements at mid-span is presented in Figure 2.16. The results presented in the figure indicate that as U_{mid} increases, the difference between the calculated and test RMS horizontal displacement remains almost constant. In contrast, the difference between the calculated and test RMS vertical displacement increases with an increase in wind speed. The consideration of buffeting and aeroelastic forces leads to the RMS responses always that are greater than those obtained by considering the buffeting forces alone.

Table 2.7 RMS displacements due to fluctuating wind component.

U_{mid} (m/s)	Lateral displacement (m)			Vertical displacement (m)		
	BLWT test results	FE model Buffeting	FE model Buffeting & aeroelastic	BLWT test results	FE Model Buffeting	FE model Buffeting & aeroelastic
30	0.053	0.037	0.045	0.162	0.112	0.119
40	0.095	0.075	0.093	0.314	0.208	0.224

Note: * The RMS results from the wind tunnel test are obtained by considering the peak responses, and a peak factor g_T is 3.5 (King and Kong 2010).

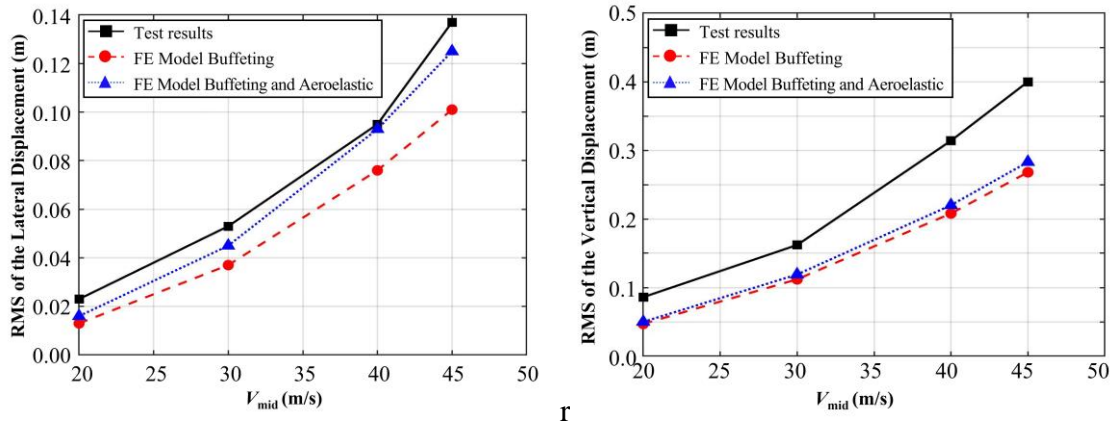


Figure 2.11 RMS of the horizontal displacement and vertical displacement at midspan for a range of U_{mid} values.

Finally, it is noted that the frequency domain approach is based on linear elastic assumption. Therefore, the RMS responses for a turbulence intensity other than 0.15 can be obtained by simply scaling the RMS responses obtained for the turbulence intensity

equal to 0.15. For example, the scaled RMS responses for turbulence intensity equal to 0.10, 0.15, and 0.20 are shown in Figure 2.17. That is, the RMS responses for turbulence intensity equal to 0.10, 0.15, and 0.20 are equal to the 0.1/0.15, 0.15/0.15, and 0.20/0.15 times the RMS response for turbulence intensity equal to 0.15. To validate this scaling, the response analysis by using the frequency approach is carried out for $U_{\text{mid}} = 30$ m/s and the turbulence intensity $I_u = 0.10$ and 0.20. The obtained RMS responses are shown in Figure 2.17, verifying the adequacy of the scaling.

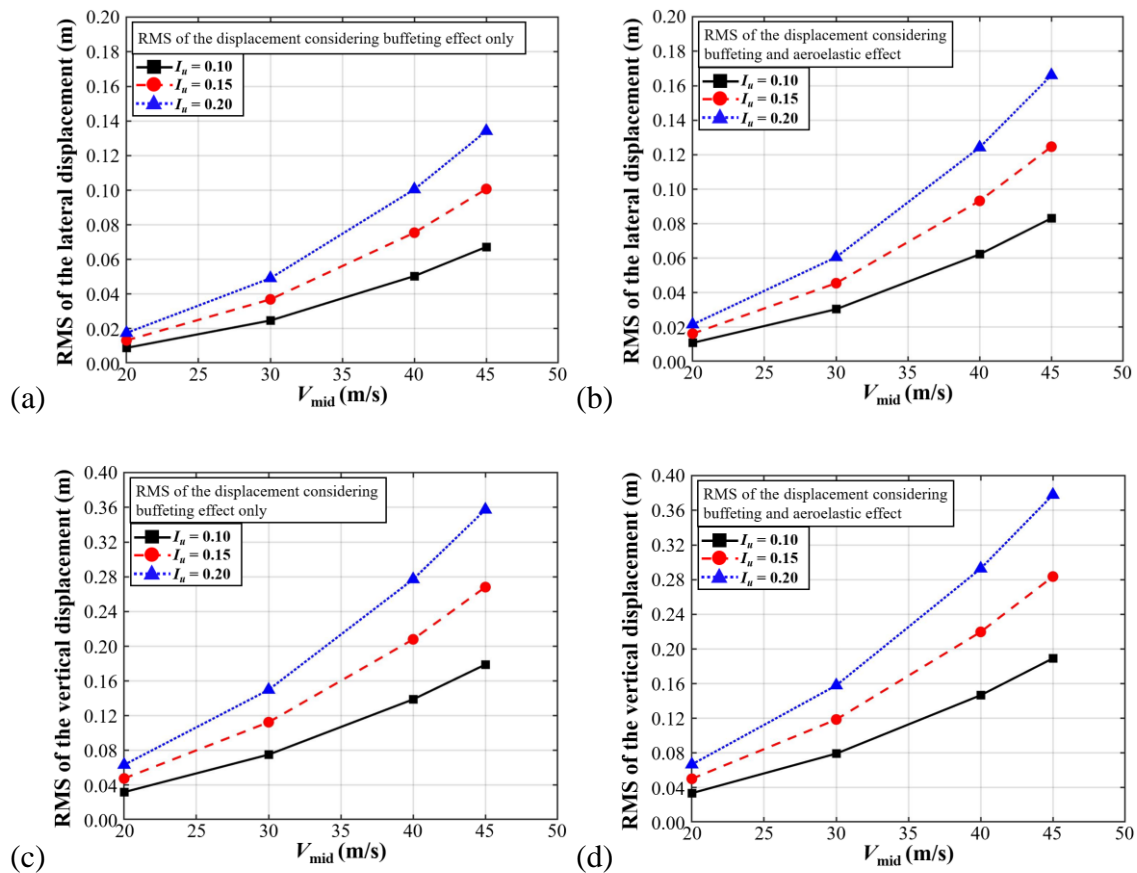


Figure 2.12 Influence of turbulence intensity on the RMS of the horizontal displacement and vertical displacement at midspan for a range of U_{mid} values.

2.4 Conclusions

The wind and bridge interaction is complex, and the light and flexible long-span bridges are highly susceptible to wind excitations. Two finite element (FE) models of the Baluarte bridge, a sophisticated FE model and a simple FE model, are developed and implemented in commercial software. The sophisticated FE model is developed by mimicking the designed structure and the full aeroelastic model. Since the number of nodes for the sophisticated FE model is too large for the buffeting and aeroelastic analysis, a simplified FE is developed using equivalent structural component properties derived from the sophisticated model.

A comparison of the dynamic characteristics of the developed FE models and of the full aeroelastic model indicates that both the identified frequencies of the first few modes of the FE models agree well with the full aeroelastic model. Based on a simple FE model, bridge responses are calculated by considering the nonhomogeneous mean wind speed, the buffeting force alone, and the buffeting and aeroelastic forces. The obtained static analysis results indicate that the calculated horizontal and vertical displacements at the mid-span of the bridge by using the simple FE model match those obtained from the wind tunnel test.

Numerical analysis of the bridge subjected to buffeting load alone, and buffeting and aeroelastic load is carried out. A comparison of the RMS responses to those obtained from the full aeroelastic model indicates that the RMS for lateral displacement is on average 30% below those obtained from the full aeroelastic model when only the buffeting force are considered. An increase in displacement is observed when buffeting and aeroelastic forces are considered. In this case the difference is 15% below from those observed in the tests. In the case of the vertical RMS, the values from the numerical model are on average 30% below those from the experimental tests.

It is possible that the strip assumption, which is the basis of the quasi-steady theory could underestimate the gust wind response. Several authors have stated the importance of unsteady characteristics derived from experimentally measured spanwise coherence of aerodynamic forces. Yet, from the full bridge aeroelastic model tests under the wind tunnel, no information related to force coherence is available now. Therefore, the study of force

coherence was beyond the scope of the present investigation. However, a recognition of the importance of a sensitivity analysis in regards to the decay parameter that defines the amount of coherence based on experimental evidence is made in the next chapter. The variability of this parameter has a big influence in the estimated bridge responses, and in particular for the vertical directions.

Chapter 3

3 Response of Baluarte bridge subjected to wind loading – an application of the time-domain approach

3.1 Introduction

In general, the wind load acted on a bridge could be classified as (Salvatori and Borri 2007): (i) a mean wind steady load, (ii) a fluctuating wind dependent buffeting load, and (iii) an aeroelastic self-excited load depending on the motion of the cross-section. The self-excited load could be further grouped as the steady and unsteady loads, where the unsteady self-excited forces are associated with aerodynamic derivatives (Scanlan and Tomko 1971). The self-excitation load for bridges is due to the aerodynamic wind-bridge interaction, which is a key issue to evaluate the bridge response and bridge stability. The interaction described by the frequency-dependent aerodynamic derivatives could also be expressed in terms of convolution integrals of the aerodynamic indicial functions (Scanlan et al. 1974). The computational efficiency could be gained by representing the aerodynamic forces using the auxiliary state-space variables and the first order differential equations (Boonyapinyo et al. 1999; Chen et al. 2000a,b).

In many practical cases, the experimental results required to determine the aerodynamic derivatives are unavailable. In this case, one could resort to the quasi-steady linear theory (Davenport 1961, 1982) to approximate the aerodynamic forces based on the steady aerodynamic coefficients and their derivatives with respect to wind attack angle. According to Chen et al. (2009), such an approach could lead to adequate results. This simplifies the evaluation of the bridge response to wind load significantly since it does not require the consideration of the frequency-dependent aerodynamic forces or solving an additional set of differential equations to determine the self-excited forces. In such a case, the estimation of the bridge responses to buffeting and aerodynamic forces could be carried out in the frequency domain, as shown in Chapter 2. Alternatively, one could also carry out the time domain analysis (Boonyapinyo et al. 1999; Chen et al., 2000a,b) by using

commercially available software such as ANSYS and simulated wind field as shown in Chen et al. (2009).

The simulation of the fluctuating wind component could be carried out in several ways. Perhaps, the most popular technique to simulate the turbulent or fluctuating wind field is the so-called spectral representation method (SRM) (Shinozuka and Jan 1972; Deodatis and Shinozuka 1989; Shinozuka and Deodatis 1996; Liang et al. 2007; Kareem, 2008). This approach is directly related to the definition of the stationary stochastic process presented by Cramer (1942) and of the evolutionary process presented in Priestley (1965). Other techniques to simulate random fields include those that are based on the Karhunen–Loève expansion (Phoon et al. 2002; Ghanem and Spanos 2003; Spanos et al. 2007), polynomial chaos (Dai et al. 2019), autoregressive moving average (Mignolet and Spanos 1992; Spanos and Zeldin 1998). Some of these methods could also be used to generate the non-Gaussian and nonstationary fields. In general, the use of these models is associated with more sophisticated mathematical concepts and is less efficient. Since the PSD function of fluctuating wind velocity depends on the mean wind velocity (Simiu and Scanlan 1996), the PSD function becomes dependent on both the frequency and time if the mean wind speed is spatiotemporally-varying. To simplify the task of simulating the nonstationary fluctuating wind, Hong (2016) proposed the use of a uniformly amplitude modulated and frequency modulated (AM/FM) process to model nonstationary fluctuating wind. This consists of applying the time transformation concept (Yeh and Wen, 1990). The nonstationary fluctuating wind is then represented by amplitude modulating a process that is nonlinearly time transformed from a stationary process. The modeling of the fluctuating winds as the stationary inhomogeneous process (i.e., fluctuating winds that are stationary in time and spatially varying mean wind speed) and as the AM/FM process are considered in this chapter.

It is noted that the full aeroelastic model tests, including the topographic effect, in the wind tunnel, as well as the numerical modelling of the bridge, are frequently carried out in wind engineering. Diana et al. (1995, 2013) presented such a comparison for the proposed bridge over Stretto di Messina, aiming at verifying the aerodynamic behaviour of the bridge in smooth and turbulent flow and the threshold wind speed for the flutter instability. The

development of the FE model and the theoretical model for the wind forces are developed by Politecnico de Milano (Falco et al. 1992). The study of the full bridge aeroelastic model was conducted at the Martin Jensen Wind tunnel for a 1:250 scale between the model and prototype.

In the present chapter, we consider the Baluarte bridge – the largest cable-stayed bridge in Mexico. The construction of the bridge at the site was carried out under the supervision of the Institute of Engineering at UNAM (Universidad Nacional Autónoma de México, in Spanish). A full bridge aerodynamic model test was carried out at the Boundary Layer Wind Tunnel (BLWT) at the University of Western Ontario (UWO) before its construction. The model was constructed and tested in a topographic flow condition similar to the one expected at the bridge site. The test results were made available for the present study (King and Kong 2010; King et al. 2011), providing a unique opportunity to investigate the difference between measured bridge responses obtained from the full aeroelastic model and calculated responses from finite element modelling. Such an analysis was carried out already, based on the frequency domain approach (see Chapter 2). However, there are limitations to the frequency-domain approach. For example, its use is difficult in dealing with the nonstationary wind field (i.e., wind field with time-varying mean wind speed and time-varying frequency content).

The main objective of the present chapter is to evaluate the response of the Baluarte bridge to wind load based on the time domain approach, and to compare the estimated response to those obtained from the full aeroelastic model and calculated based on the frequency domain. Similar to Chapter 2, it is acknowledged that some of the aerodynamic derivatives for the section model of the bridge were available for the Baluarte bridge (Costa et al. 2007), but the consideration of these coefficients for the unsteady self-excited forces is outside of the scope of this study.

3.2 Recapitulation of results from the frequency domain approach

An aeroelastic model for the whole bridge with a geometric scale of 1:250 was tested at the BLWTL at UWO (King and Kong 2010; King et al. 2011). The design of the full

aeroelastic model preserved the Froude number, the Cauchy number scaling, and the density ratio (King et al. 2011). A scaled model of the topography surrounding the bridge was modelled as well in the wind tunnel test (see Chapter 2). Some of the test results for the aeroelastic model, the dynamic characteristics of the model as well as the frequency domain analysis results are summarized in Tables 3.1 to 3.3 (for completeness and easy reference).

Two finite element (FE) models, a sophisticated model with 13765 elements and a simplified model with 1565 elements, were developed and described in Chapter 2. Both models matched the dynamic characteristics of the full aeroelastic model well. The sophisticated model is used as the basis to assign the section properties for the simplified model. It was indicated, in Chapter 2 that the use of the sophisticated FE model is computing time-consuming and that the use of the simplified three-dimensional FE (3D-FE) model provides sufficient accurate representation for the Baluarte bridge wind response. This simplified 3D-FE model, which is shown in Figure 3.1, is used in this chapter to evaluate the dynamic responses of the bridge subjected to wind forces determined based on the quasi-steady theory, and the time domain approach. Figure 3.1 also shows the first four vibration modes. For more details on the FE modelling, the reader is referred to Chapter 2.

Table 3.1 Dynamic characteristics of the bridge.

Mode shape	Test (BLWTL)	Sophisticated 3D-FE model		Simplified FE model	
		FE analysis	Relative difference		
	Frequency (Hz)				
Lateral vibration	0.251	0.251	< 0.1%	0.251	< 0.1%
Vertical vibration	0.299	0.299	< 0.1%	0.309	3.4%
2 nd lateral vibration	0.388	0.405	4.2%	0.397	2.4%
Torsion	0.434	0.437	0.6%	0.435	0.2%

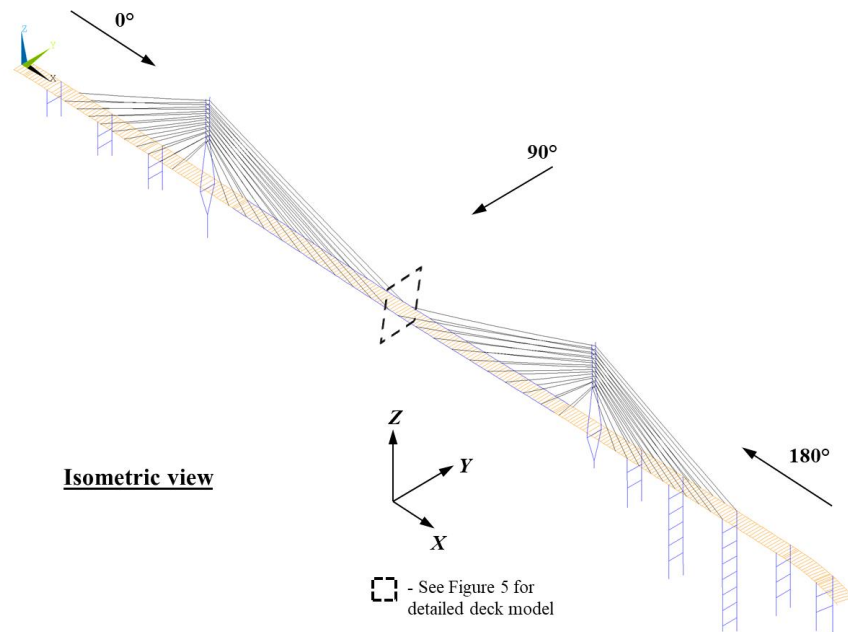
Table 3.2 Mean response of the bridge.

U_{mid}	Midspan lateral displacement (m)		Midspan vertical displacement (m)	
	BLWT test	FE model	BLWT test	FE model
30 m/s	0.212	0.237	0.02	0.023
40 m/s	0.364	0.421	0.01	0.097

Table 3.3 RMS displacements due to fluctuating wind component.

U_{mid} (m/s)	Lateral displacement (m)			Vertical displacement (m)		
	BLWT test results	FE model Buffeting	FE model Buffeting & aeroelastic	BLWT test results	FE Model Buffeting	FE model Buffeting & aeroelastic
30	0.053	0.037	0.045	0.162	0.112	0.119
40	0.095	0.075	0.093	0.314	0.207	0.220

Note: * The RMS results from the wind tunnel test are obtained based on the peak responses and a peak factor g_T of 3.5 (King and Kong 2010).



a)

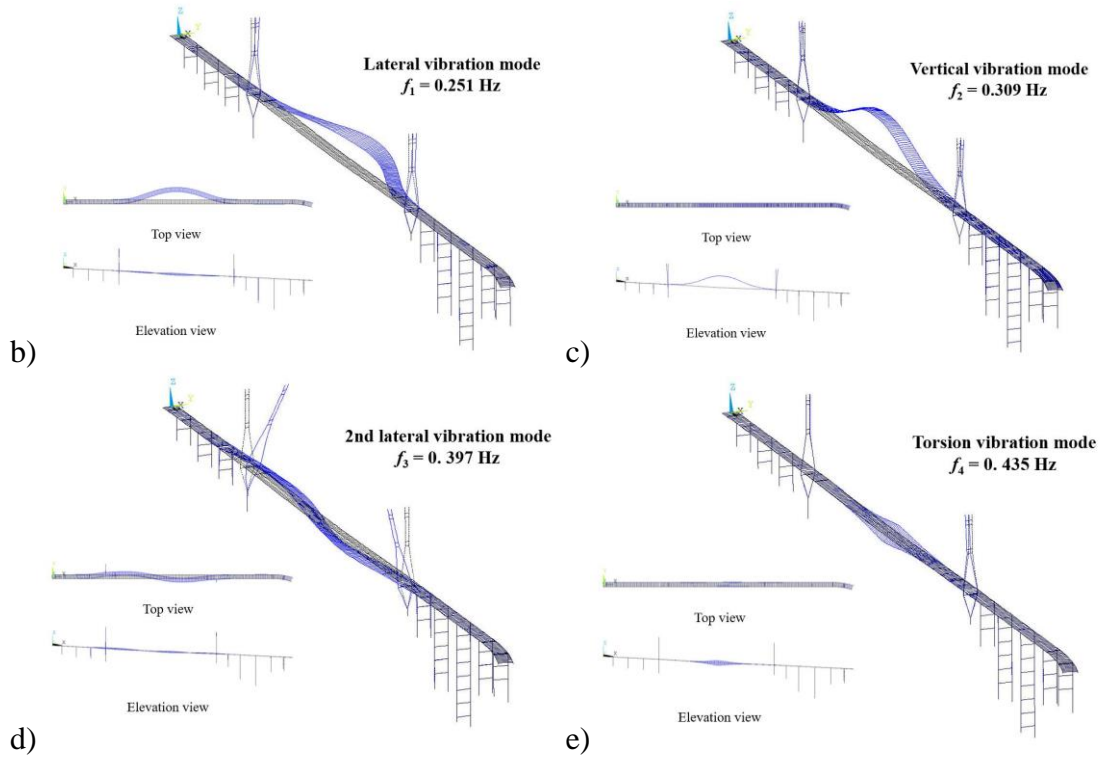


Figure 3.1 Isometric view of a simplified 3D-FE model of Baluarte Bridge and the four selected vibration modes.

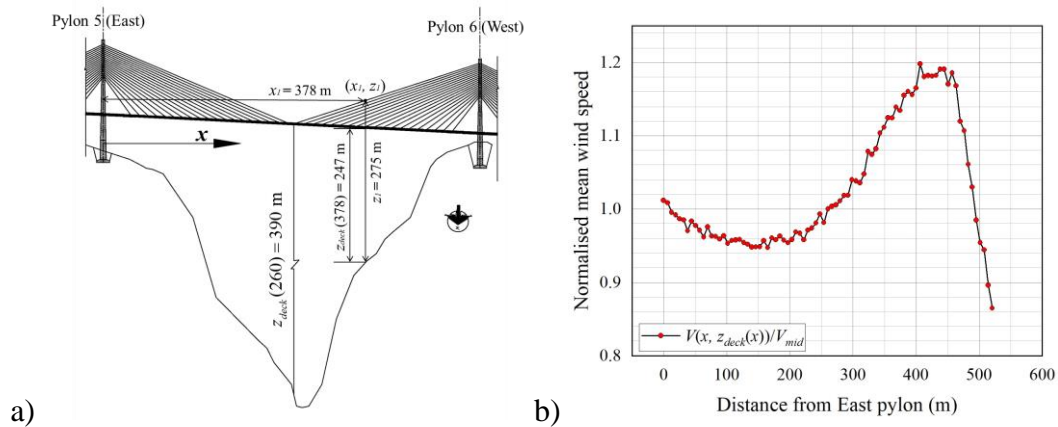
3.3 Modelling and simulation of wind speed field acted on the bridge

3.3.1 Mean wind profiles at the Baluarte bridge site

For the Baluarte Bridge, the horizontal mean wind speed at the main deck height was measured at the BLWT at the UWO. Also, the vertical wind profiles along the height at two particular locations (two principal pylons) were measured at the Wind tunnel. By considering that spatially-varying mean wind speed could be modeled by using the power-law model (Davenport 1965), and throughout a spatial interpolation, it is suggested that the horizontally varying mean wind speed is significantly affected by the topography. In this case, the along height mean wind speed is considered to be,

$$U(x, z) = r_U(x, z_{deck}(x)) \times \left(\frac{z}{z_{deck}(x)} \right)^{\alpha(x)} U_{mid} \quad (3.1)$$

where $r_U(x, z_{deck}(x)) = U(x, z_{deck}(x))/U_{mid}$, represents the along the deck wind profile normalized with respect to $U_{mid} = U_{mid}(260, z_{deck}(260))$, which depends on the coordinate x , and x is measured from the left pylon to the right pylon at the deck height (see Figures 3.2), $\alpha(x)$ is the power-law coefficient that depends on upstream terrain conditions usually taken equal to 0.16 for open country terrain (NRC 2010). Based on the wind tunnel test results, it was concluded that $\alpha(0)$ equal to 0.18 and $\alpha(520)$ equal to 0.20 could be adequate. Also, it was assumed that the power-law exponent at the point near the middle of the two pylons (i.e., at the point where the depth from the deck to the bottom of the canyon equals 390 m (see Figures 3.2) equals 0.15 (i.e., $\alpha(260) = 0.15$). The mean wind speed profile along the bridge deck $U(x, z_{deck}(x))$ is considered to be equal to the one determined from the wind tunnel test and normalized with respect to U_{mid} , where U_{mid} represents the reference hourly-mean wind speed at the “middle” span. A mean wind speed surface based on the above, by assuming $U_{mid} = 30$ m/s is illustrated in Figure 3.2b also.



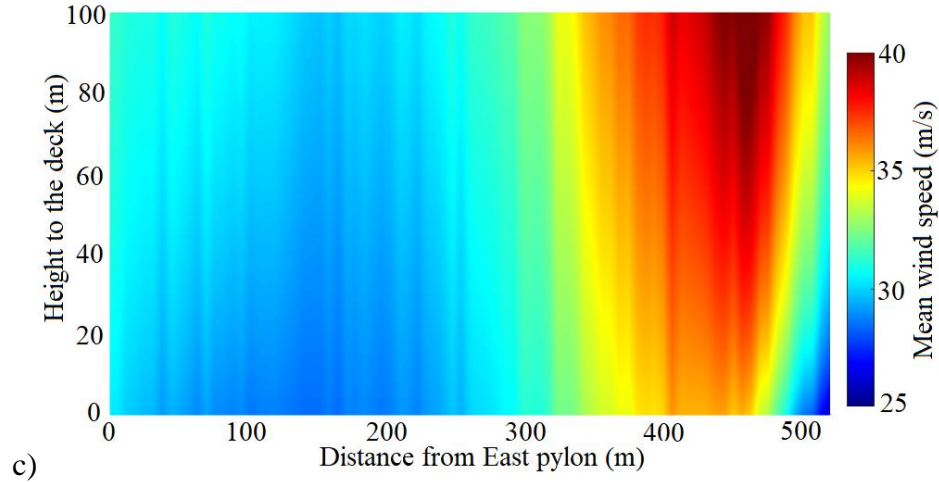


Figure 3.2 Coordinates and the mean wind profile for Baluarte bridge: a) Defined coordinates; b) Horizontal mean wind speed profile, $\mathbf{r}_U(\mathbf{x}, \mathbf{z}_{deck}(\mathbf{x})) = \mathbf{U}(\mathbf{x}, \mathbf{z}_{deck}(\mathbf{x})) / U_{mid}$; and c) Mean wind speed surface.

3.3.2 Characterization of the fluctuating wind field and its simulation

The fluctuating wind at a point \mathbf{p} (with coordinates y and z) can be characterized using the power spectral density function (Simiu and Scanlan 1996). If the Kaimal PSD function is adopted, the PSD function of the fluctuating wind along the mean wind direction $u(p, t)$ and the fluctuating wind perpendicular to the mean wind direction $w(p, t)$ at \mathbf{p} can be written as (Simiu and Scanlan 1996),

$$\frac{f(z, f)}{u_*^2} = \frac{200\zeta}{(1+50\zeta)^{5/3}}, \quad (3.2a)$$

and,

$$\frac{fS_w(z, f)}{u_*^2} = \frac{3.36\zeta}{1+10\zeta^{5/3}}, \quad (3.2b)$$

where $\zeta (= fz/U(z))$ is the Monin coordinate or reduced frequency, f the frequency in Hz; z is the height above the ground surface, and u_* the shear friction velocity. The use of these equations results in the standard deviation of $u(p, t)$, $\sigma_u(z)$, that equals $\sqrt{6}u_*$, and the standard deviation of $w(p, t)$, $\sigma_w(z)$, that equals $\sqrt{1.67}u_*$.

The fluctuating wind speed varies in time and space. The cross power spectral density (XPSD) function of $u(p, t)$ and of $w(p, t)$ at two points \mathbf{p}_i and \mathbf{p}_j , denoted as $S_{uu}(p_i, p_j, f)$ and $S_{ww}(p_i, p_j, f)$, can be expressed as Davenport (1968),

$$S_{uu}(p_j, p_k, f) = \sqrt{S_u(z_j, f)S_u(z_k, f)} \exp\left(-\frac{f}{\bar{u}_{j,k}}\left(C_y^2(y_j - y_k)^2 + C_z^2(z_j - z_k)^2\right)^{1/2}\right), \quad (3.3a)$$

and,

$$S_{ww}(p_j, p_k, f) = \sqrt{S_w(z_j, f)S_w(z_k, f)} \exp\left(-\frac{f}{\bar{u}_{j,k}}C_w|y_j - y_k|\right), \quad (3.3b)$$

where (y_j, z_j) and (y_k, z_k) are the coordinates of the points \mathbf{p}_j and \mathbf{p}_k ; C_y and C_z are the exponential decay coefficients for the coherence of along-wind in the directions of y -axis and z -axis; C_w is the exponential decay coefficient for the spanwise coherence of cross-wind; $\bar{u}_{j,k}$ is the average of the mean wind speed between points \mathbf{p}_j and \mathbf{p}_k . Similar to many applications (Simiu and Scanlan 1996; Strømme 2010), the coherence between $u(p, t)$ and $w(p, t)$ is neglected in this study.

By adopting the fluctuating wind models given in Eqs. (2.6) and (2.8) and considering the process as Gaussian, the simulation of the fluctuating winds at m points can be carried out based on the spectral representation method (SRM) (Shinozuka and Jan 1972). This involves assembling the power spectral density matrix or coherence matrix, decomposing the matrix by applying the Cholesky decomposition technique, and introducing random phases to sample the wind time histories that match the prescribed power spectral density function and coherence function. The power spectral density matrix, $S(f)$, is formed by the (j,k) -th element defined by Eq. (3.3a) if the fluctuating wind in the alongwind direction is considered and by Eq. (3.3b) if the fluctuating wind in the crosswind direction is considered. The matrix can be re-written as,

$$S(f) = L_\gamma(f)D(f)L_\gamma(f)^T \quad (3.4)$$

where $D(f)$ is the diagonal matrix with the i -th diagonal element equal to $S_u(z_i, f)$, and $L_\gamma(f)$ represents the matrix obtained by decomposing the coherence matrix, which is formed by the (p,q) -th element $S_{uu}(p_j, p_k, f)/\sqrt{S_u(z_j, f)S_u(z_k, f)}$. Instead of obtaining

the lower triangle matrix by applying Cholesky decomposition, $L_\gamma(f)$ could also be represented by the matrix with orthonormal vectors that are obtained based on eigenvalue decomposition. The application of SRM results in that the sampled vector of fluctuating winds is given by,

$$u(p_j, t) = \sum_{k=1}^N \sqrt{2S_u(z_j, f_k) \Delta f} \times (L_\gamma(f_k) C(f_k, t))_{diag-j} \quad (3.5)$$

where $f_k = (k - 1)\Delta f$, Δf is the increment of the frequency, and the (p, q) -th elements of the matrix $C(f, t)$ are formed by,

$$C_{pq,j} = \cos \left(2\pi f_j t + \tan^{-1} \left[\Im \left(l_{\gamma,pq}(f_j) \right) / \Re \left(l_{\gamma,pq}(f_j) \right) \right] + \phi_{q,j} \right), \quad (3.6)$$

in which $p, q = 1, \dots, m$; $\Im()$ and $\Re()$ represent the imaginary and real part of their arguments; $l_{\gamma,pq}(\zeta_j)$ is the (p, q) -th element in $L_\gamma(f)$, $\phi_{q,j}$ are the independent and identically uniformly distributed phase angles, between 0 to 2π . The subscript *diag-j* to a matrix denotes the j -th diagonal element of the matrix, in which $p, q = 1, \dots, m$. Note that since $L_\gamma(f)$ is real, the phase due to $l_{\gamma,pq}(\zeta_j)$ equals zero. For the numerical analysis to be presented in this section, $C_y = 16$, $C_z = 10$ and $C_w = 8$ are considered (Simiu and Yeo 2019). An example of the simulated winds and their characteristics is shown in Figures 3.3 to 3.5.

Figure 3.3 illustrates typical sampled fluctuating winds in the alongwind direction at four locations on the main deck of the bridge. The locations are identified as L1, L2, L3, and L4 with x equal to 250, 258, 266, and 314 m, respectively (see Figure 3.2). For the simulation, $U_{mid} = 45$ m/s, the time increment 0.05 seconds, and turbulence intensity of 0.15. Figure 3.4 shows the estimated average of the power spectral density functions from 25 sampled records. The figure indicates that the average matches its corresponding target, in relation to the corresponding PSD function. Also, the estimated average values of the coherence obtained from 25 pairs of simulated samples are presented in Figure 3.5. These last results indicate that the coherence between different stations matches the corresponding target.

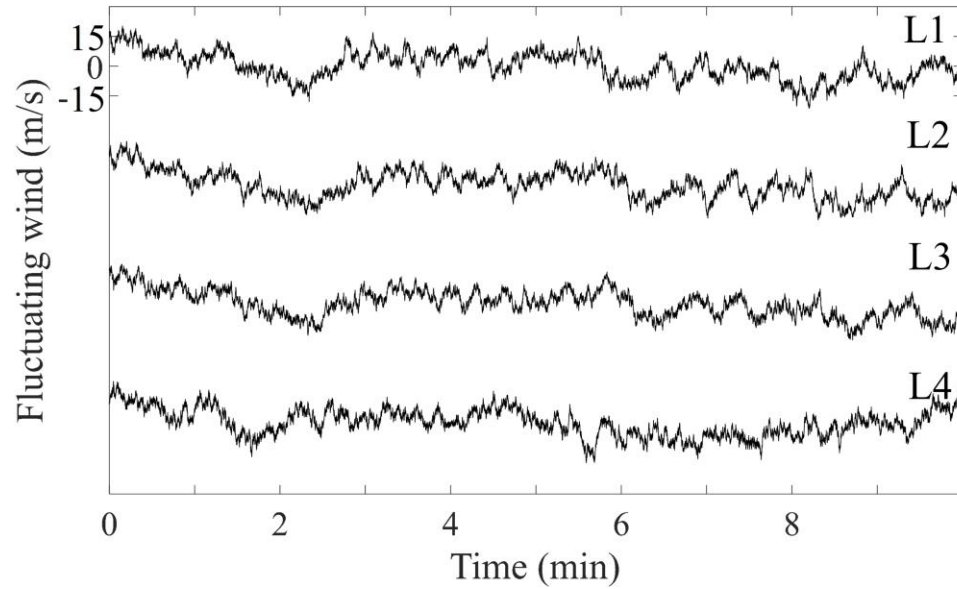


Figure 3.3 Illustration of the typical sampled records at four locations by using SRM.

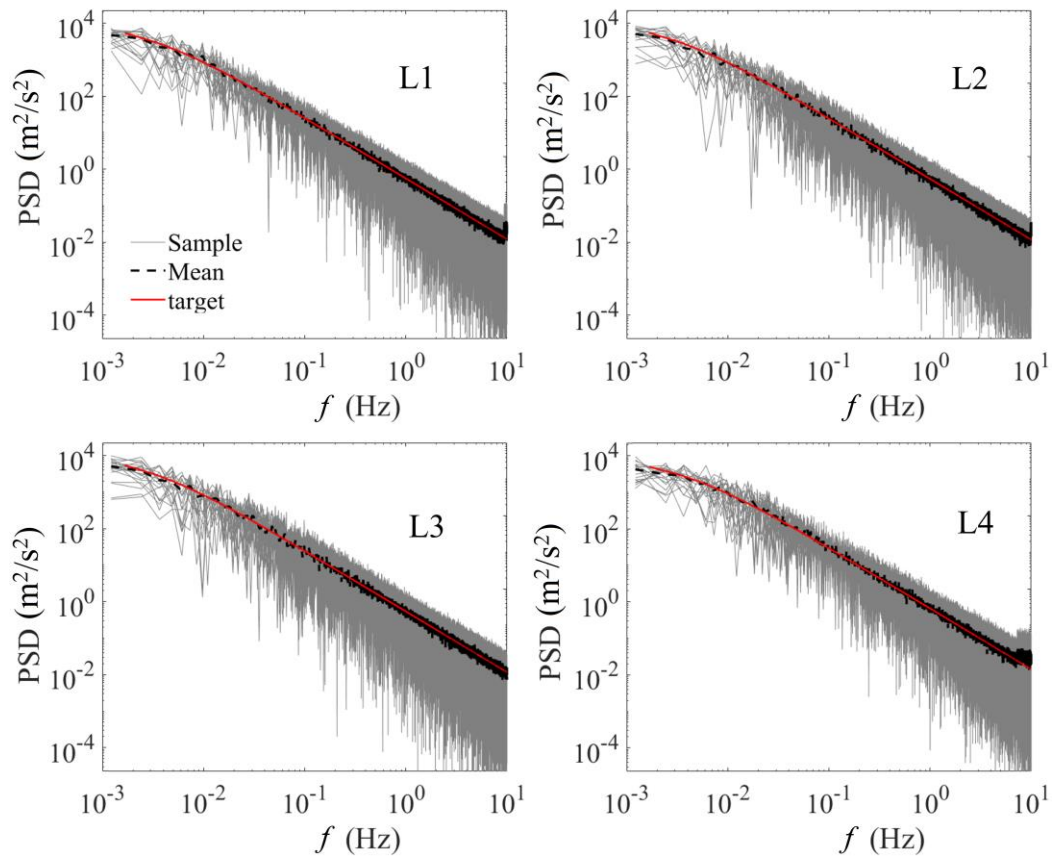


Figure 3.4 Comparison of the average of the PSD function estimated from the sampled records to its target.

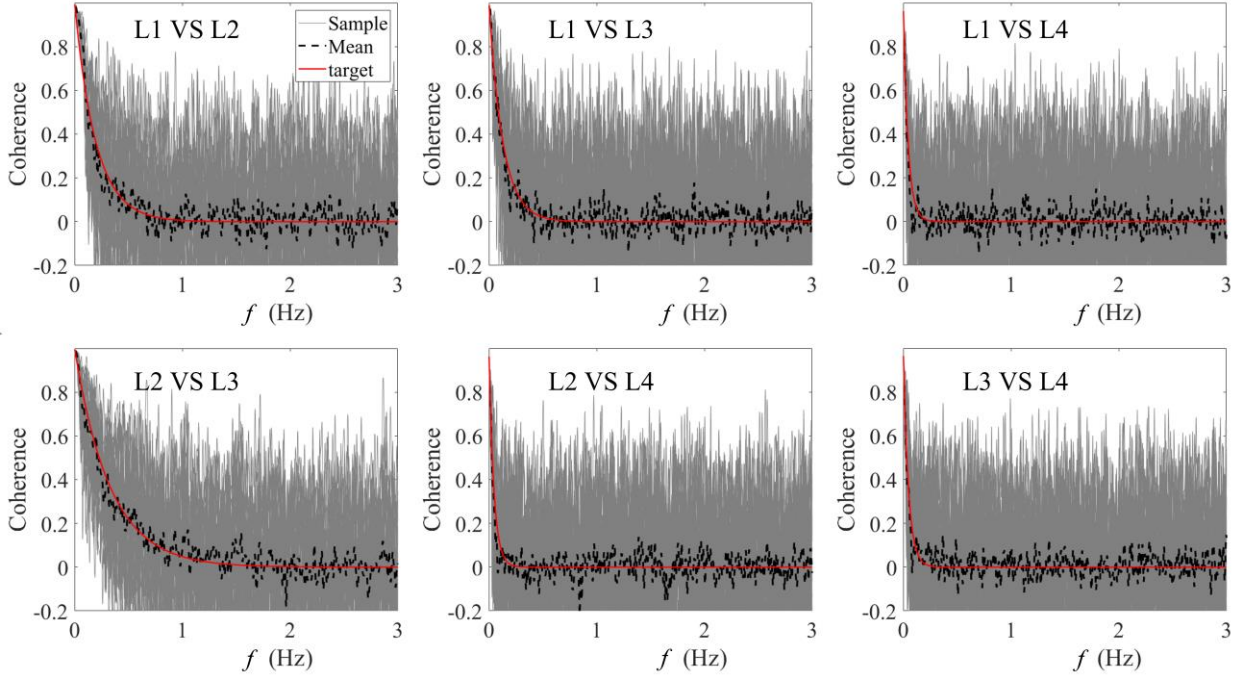


Figure 3.5 Comparison of the average of the coherence functions estimated from the sampled records to its target.

It is noted that in considering winds with time-varying mean wind speed $U(t)$, the fluctuating wind may be assumed to be an amplitude modulated process (Chen and Letchford 2005, 2007; Chay et al. 2006; Kwon and Kareem 2009),

$$u(t) = \sigma(z, t) \times \frac{u_0(t)}{\sigma_0(z)}, \quad (3.7)$$

where $u_0(t)$ denotes the fluctuating winds with standard deviation equal to $\sigma_0(z)$ and mean wind speed equal to $U_0(z)$. The time-varying standard deviation $\sigma(z, t)$ equals $U(t)$ multiplying the turbulence intensity. The samples of the process could also be simulated by using SRM. In particular, if $u(p_j, t) = (\sigma(p_j, t)/\sigma_0(z_j)) \times u_0(p_j, t)$, $j = 1, \dots, m$, where $u_0(p_j, t)$ represents a stationary process with a mean wind speed of U_{0j} , the samples of the process $u(p_j, t)$ could be obtained by applying Eq. (3.5) to simulate $u_0(p_j, t)$ and

scale it by $\sigma(p_j, t)/\sigma_0(z_j)$. For example, if the mean wind speed U_{0j} is selected to be the same as those shown in Figure 3.2 and $\sigma(z, t)/\sigma_0(z)$ is assumed to be equal to 1 if $t \leq 60$ s, $1 + \sin(\pi(t - 60)/180)$ if $60 < t \leq 240$, and 1 if $t > 240$, the sampled records shown in Figure 3.3 become those presented in Figure 3.6. However, it must be emphasized that the guidelines and justifications to select U_{0j} for this type of model are unclear.

Note that by considering the time-varying mean wind speed and Eqs. (3.2) to (3.4) that are applicable, the resulting coherence is time and frequency-varying. In such a case, the application of Eq. (3.5) requires the decomposition of the coherence function to be carried out for combinations of t and f . This is a time-consuming computing proposition, especially if the time increment of the sampled record is small (e.g., 0.01 to 0.1 s) and the duration of the record is long (e.g., for the wind loads applied at 250 nodes, with frequency to be considered ranging from 0 to 5 with an increment of 0.01 and a duration of wind of 30 minutes with a time increment of 0.05 Hz, the algorithm requires to decompose 250×250 matrix $(5/0.01) \times (30*60/0.1) = 9 \times 10^6$ times).

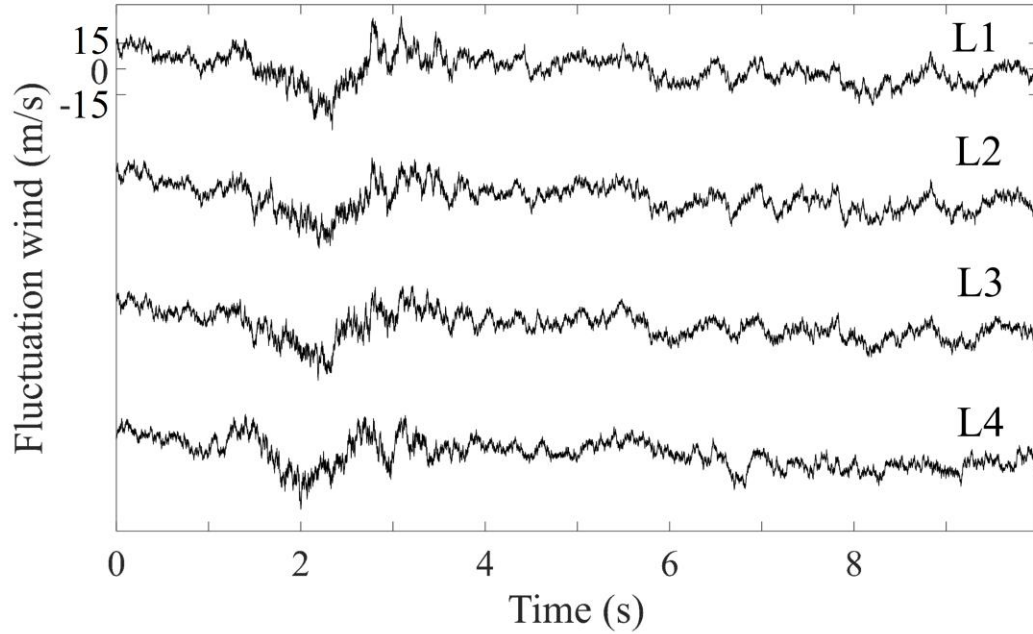


Figure 3.6 Illustration of the typical nonstationary sampled records at four locations by considering nonstationary effects.

Rather than using the model shown in Eq. (3.7), one could consider the use of the amplitude modulated and frequency modulated (AM/FM) processes to model the nonstationary fluctuating wind. In such a case and for multiple processes, instead of using the average of the mean wind speed at \mathbf{p}_j and \mathbf{p}_k , $\bar{U}_{j,k}$, in Eqs. (3.3a) and (3.3b) to evaluate the coherence function, one may use the weighted average mean $\bar{U}_{j,k} = (U(z_j)/z_j + U(z_k)/z_k)/(1/z_j + 1/z_k)$. The implication of using this suggested weighted average mean was discussed in the context of the amplitude modulated and frequency modulated process (Hong 2016). More specifically, as the mean wind speed varies vertically and horizontally, according to the measurements obtained from the wind tunnel test (see Figure 3.2) for the Baluarte bridge, the wind field is inhomogeneous. Let $\tilde{u}(\mathbf{p}, \tau) = u(\mathbf{p}, t)/\sigma_u(z)$ and the non-dimensional time $\tau = U(z)t/z$ (note that $U(z)$ depends on \mathbf{p}) if the mean wind speed is time-invariant. It can be shown that the PSD of $\tilde{u}(\mathbf{p}, \tau)$ which is a function in the τ domain, $S_{\tilde{u}}(\zeta)$,

$$S_{\tilde{u}}(\zeta) = (U(z)/z) \times S_u(z, f)/\sigma_u^2(z) = \frac{u_*^2}{\sigma_u^2(z)} \frac{200}{(1+50\zeta)^{5/3}} = \frac{2}{3} \frac{50}{(1+50\zeta)^{5/3}}, \quad (3.8)$$

and cross-PSD (XPSD) function of $\tilde{u}(\tau)$ at two points \mathbf{p}_i and \mathbf{p}_j , $S_{\tilde{u},jk}(\zeta)$, is given by,

$$S_{\tilde{u},jk}(\zeta) = (S_{\tilde{u},j}(\zeta)S_{\tilde{u},k}(\zeta))^{1/2} \times \gamma_{\tilde{u},jk}(\zeta, \mathbf{p}_j, \mathbf{p}_k) = S_{\tilde{u}}(\zeta) \times \gamma_{\tilde{u},jk}(\zeta, \mathbf{p}_j, \mathbf{p}_k) \quad (3.9a)$$

where $\zeta = fz/U(z)$,

$$\gamma_{\tilde{u},jk}(\zeta, \mathbf{p}_j, \mathbf{p}_k) = \exp(-\zeta \times h_{\tilde{u}}(\mathbf{p}_j, \mathbf{p}_k)), \quad (3.9b)$$

and,

$$h_{\tilde{u}}(\mathbf{p}_j, \mathbf{p}_k) = [C_z^2 \times (z_j - z_k)^2 + C_y^2 \times (y_j - y_k)^2]^{1/2} / [2/(1/z_j + 1/z_k)], \quad (3.9c)$$

The relation between the XPSD function of $u(p, t)$, $S_{u,jk}(f, t)$, and $S_{\tilde{u},jk}(\zeta)$ is given by (Hong 2016),

$$S_{u,jk}(f, t) = \frac{\sigma(p_j, t)\sigma(p_k, t)}{\tau'_{jk}(t)} \exp\left(-i2\pi n \frac{\tau_j(t) - \tau_k(t)}{\tau'_{jk}(t)}\right) S_{\tilde{u},jk}\left(\frac{f}{\tau'_{jk}(t)}\right) \quad (3.10)$$

where $\tau'_{jk}(t) = (\tau'_j(t) + \tau'_k(t))/2$. For constant mean wind speed case (i.e., $\tau_j = (U(p_j)/z_j)t$, $\tau'_j(t) = U(p_j)/z_j$ and $\tau'_{jk}(t) = (U(p_j)/z_j + U(p_k)/z_k)/2$). It is seen from Eq. (3.9) that the use of the weighted (time-invariant) mean wind speeds at two points results in a consistent formulation of the coherence function in the original and nondimensional time domain. However, a time-dependent phase was introduced,

Following the same procedure, one can show that the PSD of $\tilde{w}(p, \tau) = \tilde{w}(p, t)/\sigma_u(z)$, $S_{\tilde{w}}(\zeta)$,

$$S_{\tilde{w}}(\zeta) = (U(z)/z) \times S_w(z, f)/\sigma_w^2(z) = \frac{u_*^2}{\sigma_w^2(z)} \frac{3.36}{1+10\zeta^{5/3}} = \frac{2}{10} \frac{10}{1+10\zeta^{5/3}}, \quad (3.11)$$

and the XPSD function of $\tilde{w}(\tau)$ at two points \mathbf{p}_i and \mathbf{p}_j , $S_{\tilde{w},jk}(\zeta)$, is given by,

$$S_{\tilde{w},jk}(\zeta) = (S_{\tilde{w},j}(\zeta)S_{\tilde{w},k}(\zeta))^{1/2} \times \gamma_{\tilde{w},jk}(\zeta, \mathbf{p}_j, \mathbf{p}_k) = S_{\tilde{w}}(\zeta) \times \gamma_{\tilde{w},jk}(\zeta, \mathbf{p}_j, \mathbf{p}_k), \quad (3.12)$$

where $\gamma_{\tilde{w},jk}(\zeta, \mathbf{p}_j, \mathbf{p}_k) = \exp(-\zeta \times h_{\tilde{w}}(\mathbf{p}_j, \mathbf{p}_k))$ and $h_{\tilde{w}}(\mathbf{p}_j, \mathbf{p}_k) = C_w |y_i - y_j| / [2/(1/$

$z_j + 1/z_k) \Big]$.

For the case when the mean wind speed at \mathbf{p} is time-varying (i.e., $U(z, t)$), the non-dimensional time at \mathbf{p} , τ , is given by (Hong 2016),

$$\tau = \tau(t, \mathbf{p}) = \frac{1}{z} \int_0^t U(z, \hat{t}) d\hat{t}, \quad (3.13)$$

where z is the height above the ground surface that corresponds to the point \mathbf{p} .

Based on the standardized fluctuating wind formulation, the equation to simulate the vector of fluctuating wind at m points was given in Hong (2016). This is done by first simulating m stationary processes using the SRM (Shinozuka and Jan 1972) in the τ -domain based on the $m \times m$ PSD matrix of the processes, $S_{\tilde{u}}(\zeta)$, with its element defined by Eq. (3.8) or $S_{\tilde{w}}(\zeta)$ with its elements defined by Eq. (3.11). The $m \times 1$ vector of fluctuating winds $\mathbf{u}(\mathbf{p}, t)$, is then given by (Hong 2016),

$$\mathbf{u}(\mathbf{p}, t) = \Gamma(\mathbf{p}, t) \odot \tilde{\mathbf{u}}(\mathbf{p}, \tau) = \Gamma(\mathbf{p}, t) \odot \sum_{j=1}^N \sqrt{2\Delta\zeta} \times LC_j(\zeta_j, \tau) \quad (3.14)$$

where $\Gamma(\mathbf{p}, t)$ is an $m \times 1$ vector with the j -th element $\sigma(\mathbf{p}_j, t)$; \odot denotes the element-to-element multiplication of two vectors; $\tilde{\mathbf{u}}(\mathbf{p}, \tau)$ is the $m \times 1$ vector of simulated incoherent stationary processes with the j -th element $\tilde{u}(\mathbf{p}_j, \tau)$ and $\tau = \tau_j(t)$. The $m \times 1$ vector $LC_j(\zeta_j, \tau)$ in Eq. (3.14) is formed by the diagonal element of $L(\zeta_j)[C_j(\tau)]^T$, where the subscript T denotes the transpose of a matrix, $\mathbf{L}(\zeta_j)$ denotes the lower triangle matrix obtained from the Cholesky decomposition of $S_{\tilde{u}}(\zeta_j)$, and the elements of the $m \times m$ matrix $\mathbf{C}_j(\tau)$ are given by,

$$C_{pq,j} = \cos\left(2\pi\zeta_j\tau + \tan^{-1}\left[\Im(l_{pq}(\zeta_j))/\Re(l_{pq}(\zeta_j))\right] + \phi_{q,j}\right), \quad (3.15)$$

in which $p, q = 1, \dots, m$; $l_{pq}(\zeta_j)$ is the row-column element in $\mathbf{L}(\zeta_j)$.

Based on this algorithm, simulated winds at a few selected nodes for the model of the Baluarte bridge are illustrated in Figures 3.7 to 3.9. Figure 3.7 illustrates typical sampled nonstationary (i.e., frequency modulation and spatially inhomogeneous) wind records for $U_{mid} = 45$ m/s. Figure 3.8 shows the samples of the average of the PSD function of 25 simulated wind records in frequency f (that corresponds to the original time domain t) as well as in nondimensional frequency ζ (that corresponds to nondimensional time τ). It

shows that the average of the PSD function agrees well with its target. The comparison of the coherence function estimated from the samples in terms of ζ is shown in Figure 3.9. The statistical variability presented in Figures 3.8 and 3.9 is consistent with that observed from the application of SRM for the stationary case.

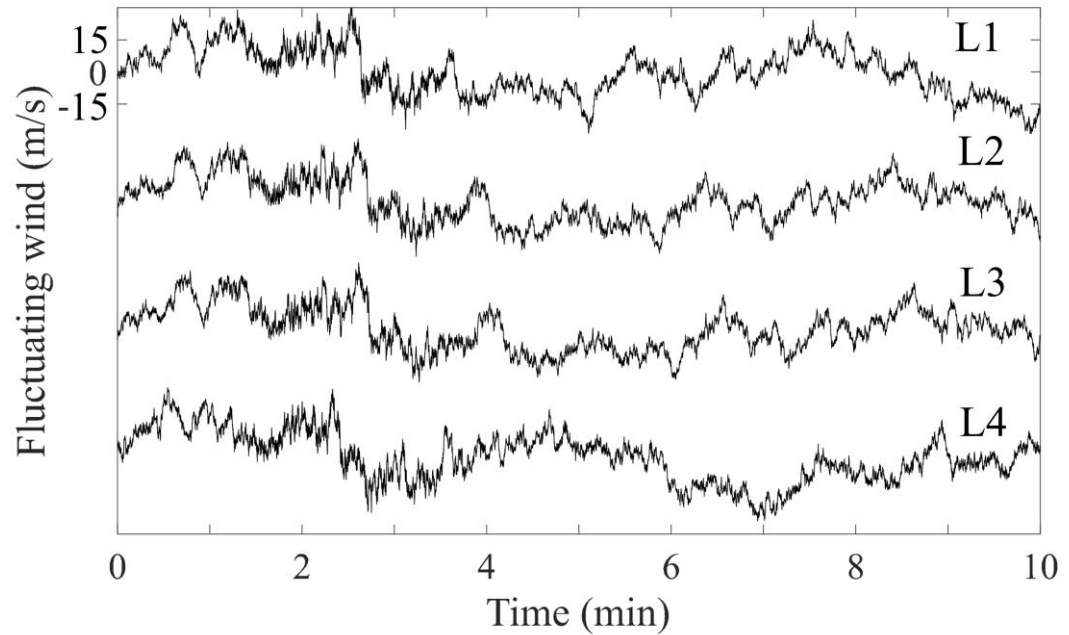
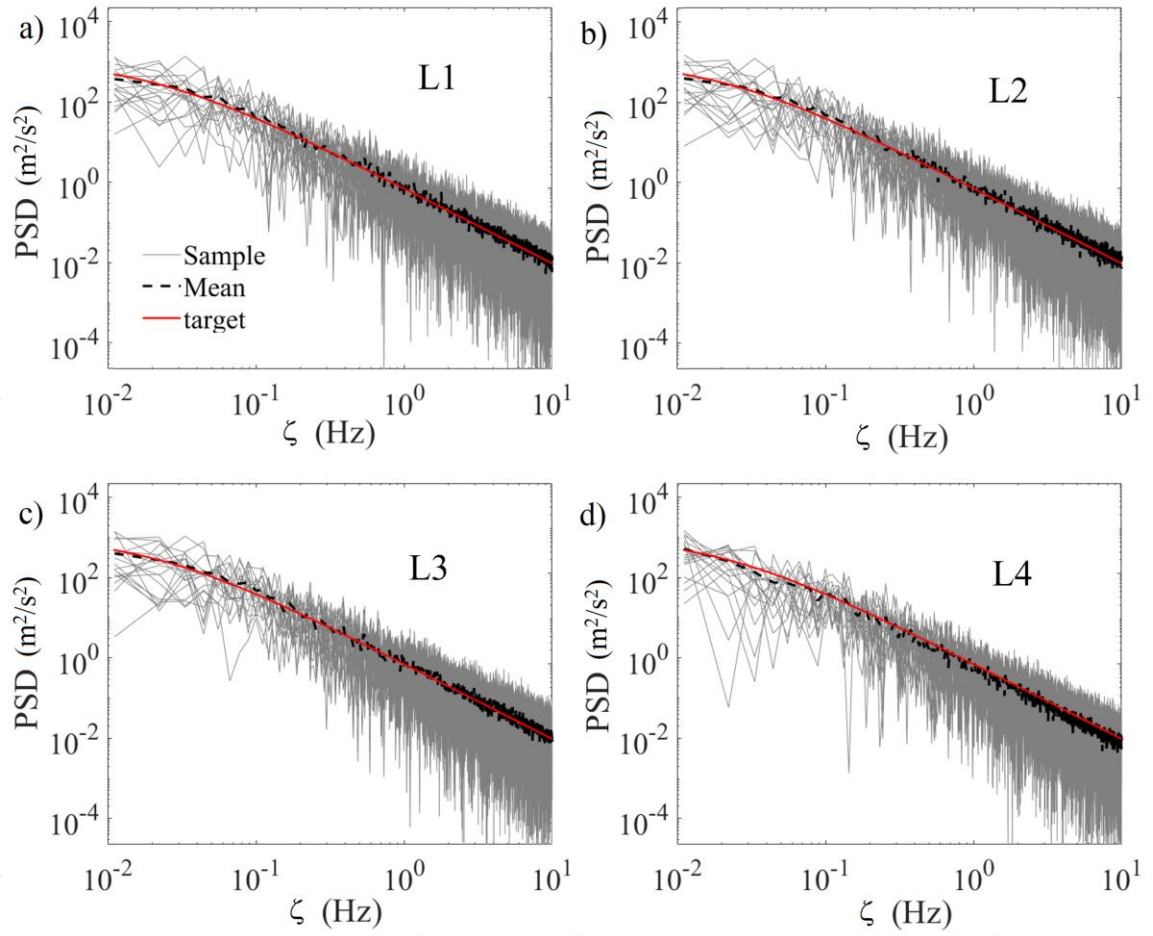


Figure 3.7 Illustration of the typical sampled records at four locations by considering nonstationary effects (amplitude modulation and frequency modulation).



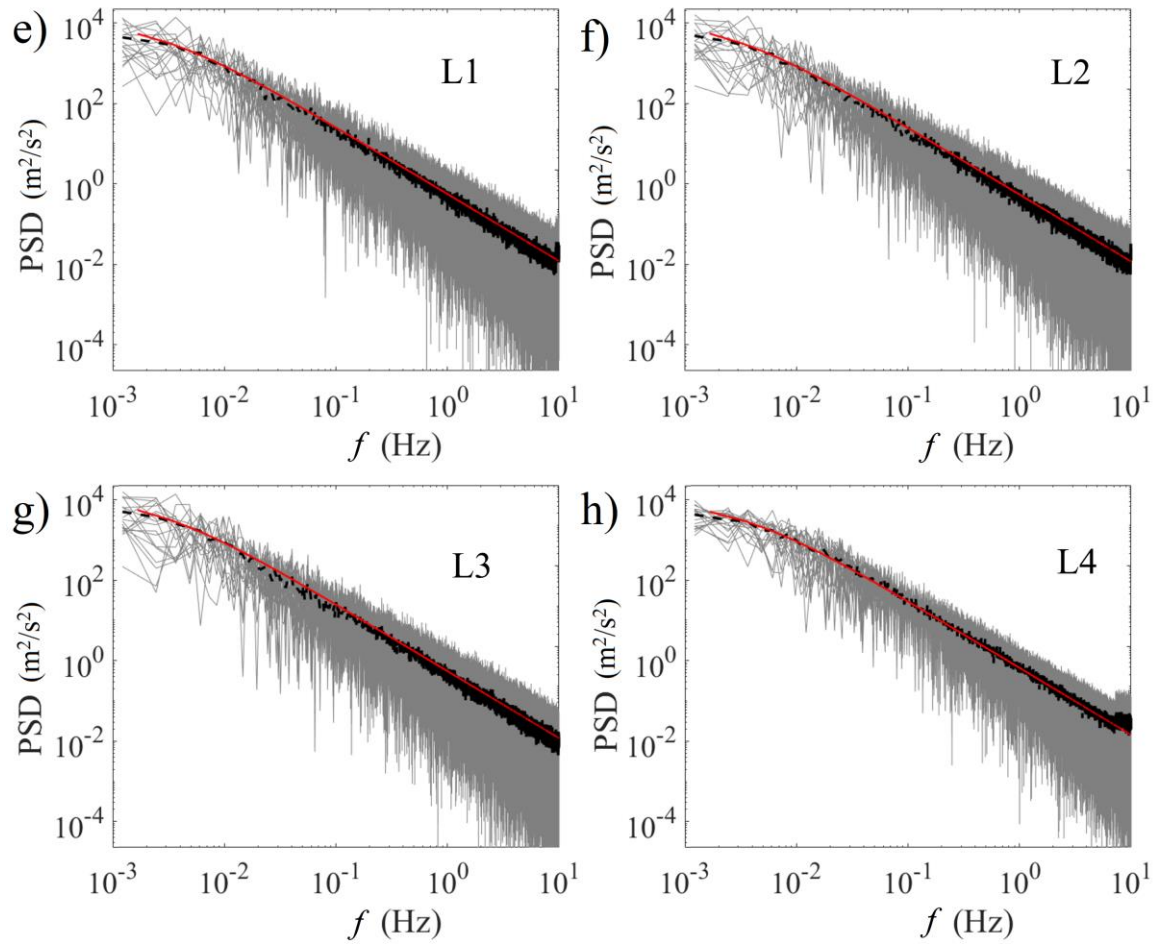


Figure 3.8 Comparison of the average of the PSD function estimated from the sampled records to its target: a) to d) Comparison at four locations in terms of ζ , e) to h) Comparison at four locations in terms of frequency.

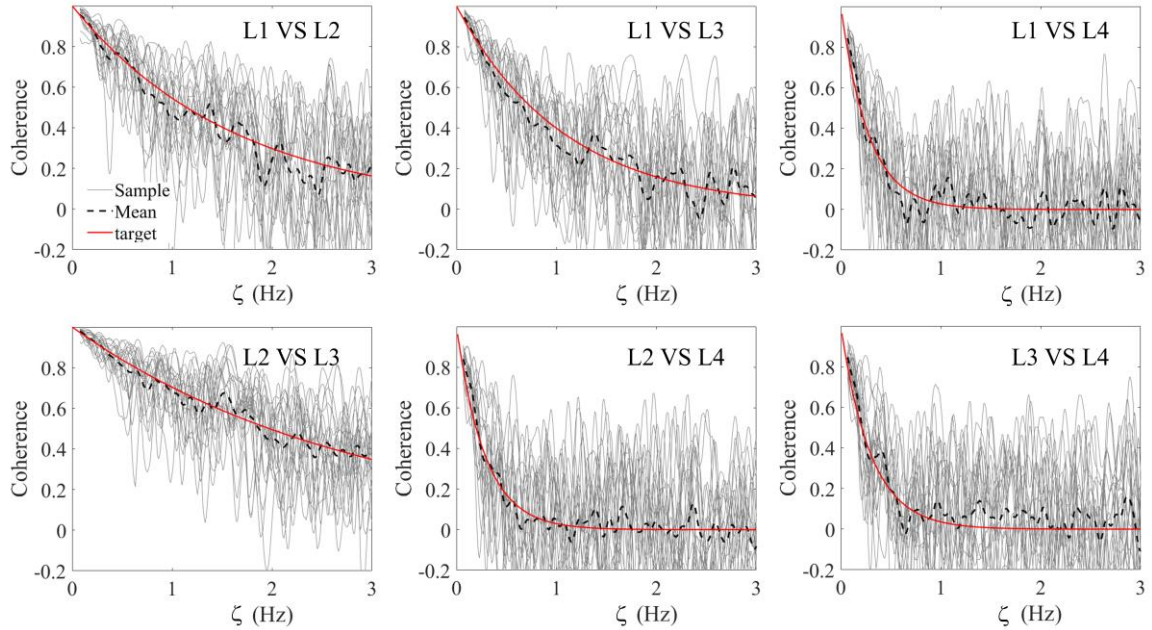


Figure 3.9 Comparison of the average of the coherence function estimated from the sampled records to its target in terms of ζ .

3.4 RMS of the responses by considering time-invariant mean wind speed

3.4.1 Time history responses at the midspan

By using the simulated vector of wind velocity at the nodal points of the finite element model of the Baluarte bridge and carrying out a time history analysis, the time history of the displacements at all points is obtained. For the analysis, first, the gravity load is applied to the structure. This is followed by the application of the wind load corresponding to the mean wind velocity. Then, the dynamic time history wind load due to 10 minutes of the fluctuating wind is applied to the bridge. The fluctuating winds are sampled with a time increment of 0.1 seconds and considering Δf equal to $1/300$. An illustration of the sampled horizontal and vertical fluctuating winds at $x = 250$ m at the deck height is shown in Figure 3.10. Typical time histories for the horizontal and vertical displacements of the bridge at midspan are presented in Figure 3.11 for a mean wind speed of 30 m/s and 40 m/s. For the analysis, the buffeting force and buffeting combined with the self-excited forces are

considered. By comparing Figures 3.10 with 3.11, we can observe that the time histories of the displacements do not match those of the fluctuating wind. This is to be expected since the wind field is inhomogeneous and incoherent and since the displacements are controlled not only by the background response but also by the resonant responses and the natural frequency of the principal mode shapes.

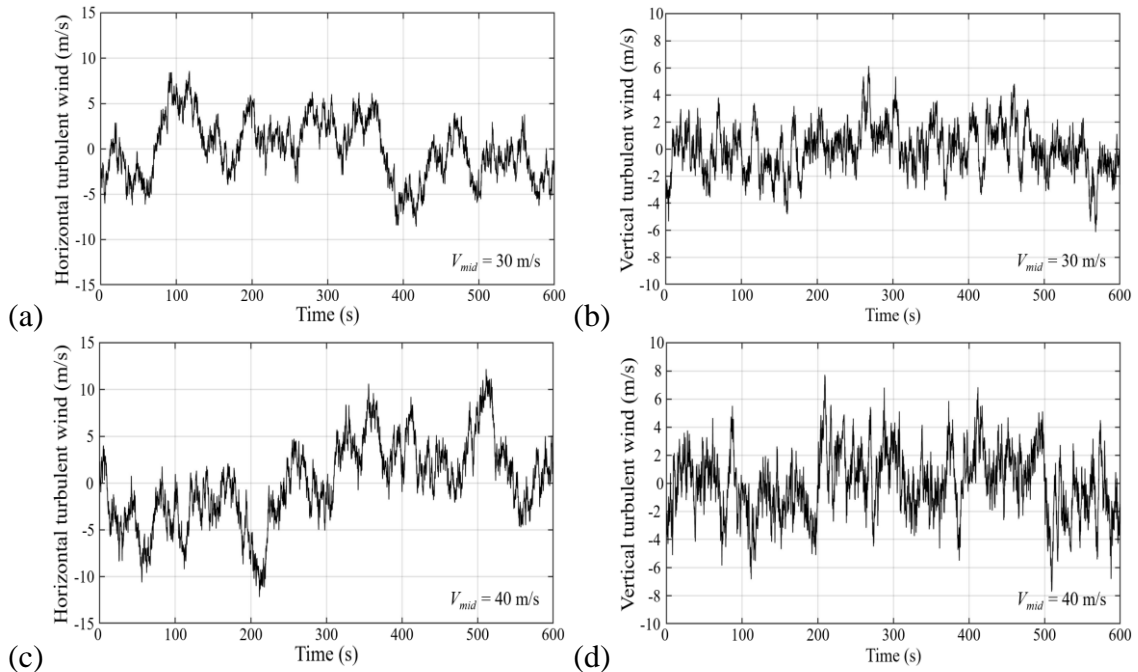
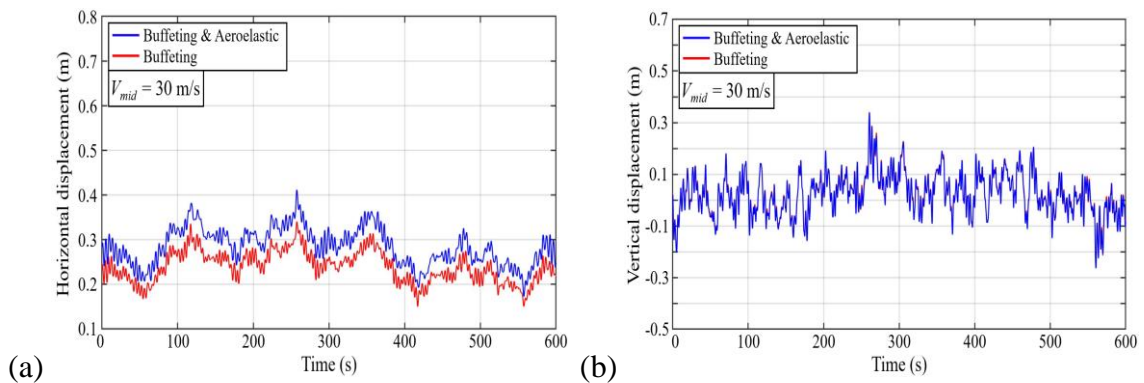


Figure 3.10 Sampled wind at midspan ($x = 250$ m, see Figure 3.2): The first row for $U_{mid} = 30$ m/s, and the second row for $U_{mid} = 40$ m/s.



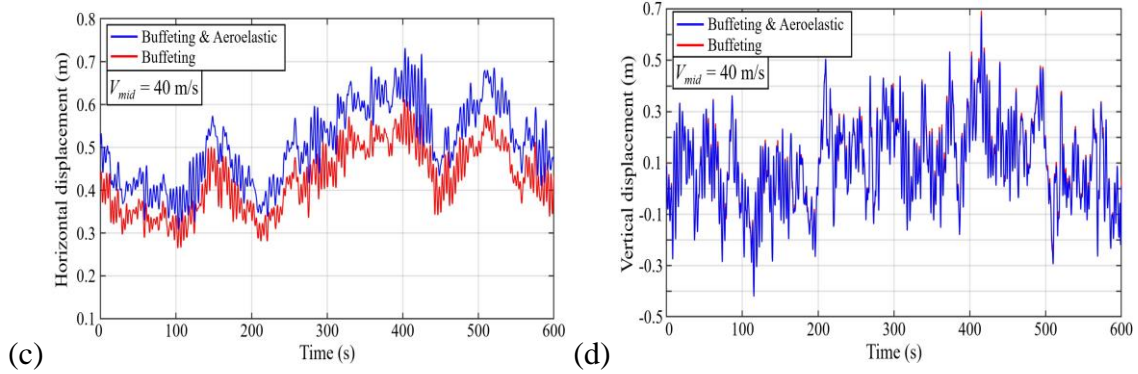


Figure 3.11 Typical horizontal and vertical displacements at the midspan ($x = 250$ m, see Figure 3.2) due to wind load. The displacements are related to their static equilibrium position, including the large deformation effect. The first row for $U_{mid} = 30$ m/s, and the second row for $U_{mid} = 40$ m/s.

The RMS of the displacements calculated based on the time histories is also calculated. This calculation process is repeated for each of the considered mean wind velocities. The obtained RMS based on 25 runs for $U_{mid} = 30$ m/s, each with 10 minutes time history, is calculated and is equal to 0.054 m for the horizontal displacement and 0.107 m for the vertical displacement if only the buffeting forces are considered. These RMS values become 0.055 m and 0.112 m if both the buffeting and the aeroelastic forces based on quasi-steady theory are considered. Similarly, by considering $U_{mid} = 40$ m/s instead of 30 m/s, the obtained RMS responses are presented in Table 3.4 and Table 3.5. Besides, the horizontal and vertical displacements for $U_{mid} = 30$ m/s and $U_{mid} = 40$ m/s are also compared to the results obtained from the full aeroelastic model test and the frequency domain analysis, obtained in the previous chapter.

The comparison presented in the table indicates that the RMS of the horizontal displacement obtained from the time domain analysis is about 35% higher than those obtained based on the frequency domain analysis. One of the reasons for the observed differences between horizontal displacement could be due to that in using harmonic analysis in the frequency domain approach the large deformation could not be considered. However, for the vertical displacement, the RMS response for the time and frequency domain are more similar. The discrepancies are found between displacements from the numerical model and the BLWT test results.

Table 3.4 Comparison of the RMS horizontal displacements dues to fluctuating wind component.

U_{mid} (m/s)	Lateral displacement (m)				
	BLWT test results	Frequency domain approach		Time domain approach	
		FE model Buffeting	FE model Buffeting & aeroelastic	FE model Buffeting	FE model Buffeting & aeroelastic
30	0.053	0.038	0.045	0.060	0.061
40	0.095	0.078	0.093	0.108	0.113

Table 3.5 Comparison of the RMS vertical displacements dues to fluctuating wind component.

U_{mid} (m/s)	Vertical displacement (m)				
	BLWT test results	Frequency approach		Time approach	
		FE model Buffeting	FE model Buffeting & aeroelastic	FE model Buffeting	FE model Buffeting & aeroelastic
30	0.162	0.112	0.119	0.106	0.111
40	0.314	0.207	0.224	0.219	0.231

Note: * The RMS results from the wind tunnel test are obtained based on the peak responses and a peak factor G_T of 3.5 (King and Kong 2010).

It is possible that the strip assumption, which is the basis of the quasi-steady theory, can underestimate the gust wind response. Jakobsen et al. (1997) showed that the spanwise correlation of buffeting forces is considerably stronger than the structure of the oncoming turbulence. Larose and Mann (1998), and Chen et al. (2009), also found that the pressure field throughout the bridge deck has a higher spanwise correlation than that one of the wind field which is considered under the strip assumption.

3.4.2 Influence of mean wind speed and the exponential decay coefficients for the coherence on the responses

To assess the influence of the mean wind speed on the RMS of the displacement, the analysis that is carried out in the previous sections is repeated by considering U_{mid} ranging from 10 to 45 m/s. The obtained RMS for horizontal and vertical displacements at the mid-

span are presented in Figure 3.12 and compared with those obtained based on the frequency approach obtained in Chapter 2. The differences between the obtained results based on the time history analysis and the frequency approach are consistent with those discussed in the previous section. The consideration of buffeting and aeroelastic forces leads to a slight increase in the RMS responses, when compared to the buffeting forces alone.

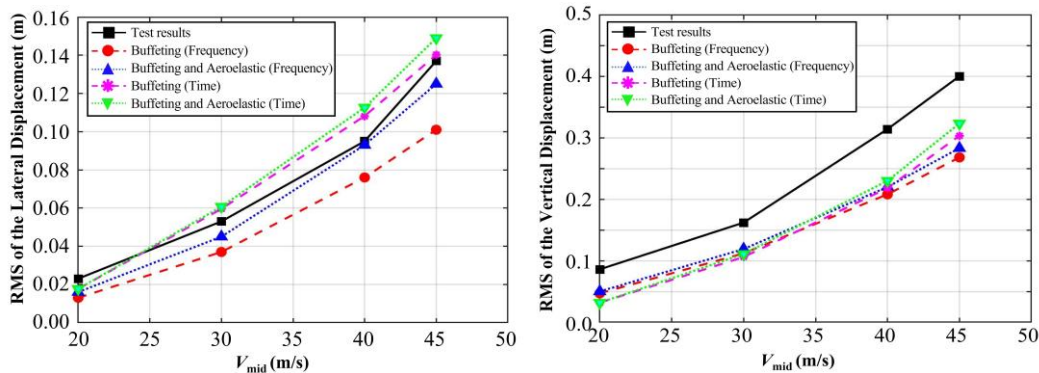


Figure 3.12 RMS of the horizontal displacement and vertical displacement at midspan for a range of U_{mid} values and comparison of RMS obtained based on time-domain and frequency domain approach.

There are differences between the obtained responses based on the time-domain approach and frequency approach. The differences are more obvious in the case of the lateral RMS. Part of these differences could be attributed to the consideration of larger deformation in the time domain approach. To assess and compare the effect of considering and neglecting the large deformation, the analysis that is carried out with larger deformation for the mean wind speed equal to 30 m/s and considering the buffeting and aeroelastic forces is repeated but neglects the larger deformation. This is done by setting the initial state of the bridge equal to that determined based on the gravity load under the large deformation. Then, the option of the larger deformation in ANSYS is switched-off, and the analysis in the time domain is carried out. The obtained average of the RMS of the horizontal and vertical displacements equals 0.0271 and 2.411, respectively. Such results are entirely unreasonable. This may be explained by noting that the initial deformed configuration, which is set equal to that determined by the gravity load under large deformation is immediately bounced to the deformed configuration that is associated with

neglecting the large deformation once the time-history analysis starts. The deformed state without large deformation is likely to release some of the prestress associated with large deformation. In short, such an analysis is not advisable. A comparison of these values to those shown in Tables 3.4 and 3.5 indicates that indeed the horizontal RMS response is reduced by neglecting the large deformation. It suggests that the consideration of large deformation in defining the initial bridge state is important for the analysis of bridge responses to wind load.

In addition, it is expected that the exponential decay coefficients for the coherence can impact the calculated responses. As no measured wind records in the boundary layer wind tunnel test or at the bridge site can be used to assess such coefficients, a parametric analysis was carried out by varying the exponential decay coefficients. The obtained results are shown in Tables 3.6 and 3.7. The results show that the RMS of the vertical displacement is very sensitive to the assigned C_w but insensitive to C_x and C_y . In contrast, the RMS of the horizontal displacement depends on the assigned C_x and C_y but is insensitive to C_w .

Table 3.6 Effect of the assigned coherence and turbulence intensity on the estimated RMS responses (sensitivity to the decay coefficient C_w for $C_x = 16$ and $C_y = 10$).

Value of C_w	$I = 0.11$		$I = 0.15$		Test	
	Vertical	Lateral	Vertical	Lateral	Lateral	Vertical
2	0.1061	0.0449	0.1449	0.0613	0.0530	0.1620
5	0.0892	0.0449	0.1219	0.0609		
8	0.0812	0.0444	0.1109	0.0607		
11	0.0761	0.0444	0.1039	0.0606		
14	0.0724	0.0443	0.0989	0.0606		

Table 3.7 Effect of the assigned coherence and turbulence intensity on the estimated RMS responses (sensitivity to the decay coefficient C_x and C_y for $C_w = 8$)

C_x	C_y	$I = 0.11$		$I = 0.15$		Test	
		Vertical	Lateral	Vertical	Lateral	Lateral	Vertical
16	10	0.0812	0.0444	0.1109	0.0607	0.0530	0.1620
12	10	0.0813	0.0464	0.1111	0.0634		
16	6	0.0812	0.0456	0.1109	0.0624		

3.5 Conclusions

In this chapter, a review of fluctuating wind modeled as a stochastic process is first presented. This is followed by a brief explanation of using the spectral representation method used to simulate an inhomogeneous wind field. Simulated winds are used to evaluate the response of the Baluarte bridge by using the time history analysis. The obtained RMS displacements of the bridge based on the time domain approach are compared with those obtained based on the frequency domain approach and the full aeroelastic model test results. The major observations from the analysis results and comparison are:

- 1) The RMS of the horizontal displacement at bridge midspan obtained from the time domain analysis are almost identical to the displacements obtained from the Wind tunnel tests. In the case of the vertical RMS, the results of the time domain analysis are more similar to those obtained from the frequency domain analysis. However, for very high wind speeds the time domain analysis approximates better the target results from the Wind tunnel. One of the reasons for the observed differences between time and frequency domain could be due to the fact, that in using harmonic analysis in the frequency domain approach, the large deformation could not be considered.
- 2) The time domain analysis could be used to evaluate the bridge responses subjected to wind loading by considering the large deformation effect. This is advantageous, although multiple runs could be time-consuming. The obtained results, in this case, approximate better the responses obtained from the full model scale wind tunnel test results.
- 3) There are some differences between the numerically calculated and wind tunnel tests for vertical displacement. While an effort is made to find out the reason for the discrepancy, the actual reason for the discrepancy could not be pinpointed. This is because the actual wind records from the wind tunnel or at the bridge site are unavailable for assessing the exponential decay coefficient of the coherence, and such a coefficient can influence significantly the estimated bridge responses in the horizontal and vertical directions. In fact, as the sensitivity analysis shows that

depending on the assigned exponential decay coefficient of the coherence, the estimated RMS horizontal and vertical directions can be made close to aeroelastic model test results from the BLWTL.

- 4) The applicability and advantages of the time domain approach to evaluate the bridge responses of nonstationary inhomogeneous winds is illustrated. Once the fluctuating winds are simulated (Gaussian or non-Gaussian), the time domain approach can be employed. The concept of amplitude modulation and frequency modulation are able to incorporate the variability of the amplitude and the frequency into the spatially incoherent simulated time history. However, due to the unavailability of the actual measurements of the nonstationary winds at the bridge site. The analysis for realistic scenario wind events could not be carried out. It is suggested that such an exercise could be carried out in a future study.

Chapter 4

4 Summary, conclusions, and potential future works

4.1 Summary and conclusions

This study is focused on comparing the responses of the Baluarte bridge obtained based on full aeroelastic model test results obtained from BLWT and those calculated from a finite element model. The estimation of the responses due to mean wind velocity is straightforward. However, the evaluation of the responses for the fluctuating component of the wind that is modeled as a stochastic process is much more involved.

Two finite element (FE) models of the Baluarte bridge, a sophisticated FE model and a simple FE model, are developed and implemented in ANSYS. The sophisticated FE model is developed by mimicking the designed structure and the full aeroelastic model. Since the number of nodes for the sophisticated FE model is too large for the buffeting and aeroelastic analysis, a simplified FE is developed by using equivalent structural component properties derived from the sophisticated model. A comparison of the dynamic characteristics of the developed FE models and of the full aeroelastic model indicates that the models have a good agreement with the model tests.

Both the frequency domain approach and the time domain approach are used to evaluate the root-mean-square (RMS) responses due to the fluctuating horizontal and vertical winds. When using the frequency approach with the commercially available ANSYS, the harmonic analysis option is employed. However, for the harmonic analysis, it was observed that the large deformation option could not be implemented. Consequently, the large deformation of the cable could not be taken into account.

When considering the frequency domain approach, the lateral RMS is on average 15% to 30% below the RMS measured on the aeroelastic scaled model from the wind tunnel tests for a mean wind speed of 30 m/s. In the case of the RMS of the vertical displacement, the difference is about 30%. For both RMS of the horizontal and vertical displacement, similar results are found when buffeting and aeroelastic forces are considered. The observed differences depend on the considered mean wind speed.

The estimation of the bridge responses analysis is also carried out based on the time domain approach. In this case, the large deformation effect was taken into account, since the dynamic analysis option is used in ANSYS, instead of the harmonic analysis. From the time domain analysis, it is observed that the RMS of the horizontal lateral displacements are close to those obtained from the full aeroelastic model tests. In this case, the consideration of the large deformation is made. This allows for fully prestressed cables on the FE model.

It should be noted that wind records from the wind tunnel test or at the bridge site are unavailable for assessing the decay coefficients of the coherence. The analysis was carried out using the typical decay coefficient suggested in the literature. However, a parametric investigation was carried out by varying the decay coefficients for the coherence in three orthogonal directions. It was shown that the decay coefficient for the coherence has a significant impact on the estimated RMS responses. Therefore, a more convincing comparative study should be carried out once the wind records (with subsecond sampling interval) become available and the actual exponential decay coefficient of the coherence could be assigned.

Apart from the formulation of non-homogeneous wind, the simulation of nonstationary fluctuating winds at multiple points is also explored. In this case, the simulated processes are discussed in terms of the amplitude modulation and frequency modulation, which seems a better representation of the continuous changing nature of wind processes throughout the evolution of time.

4.2 Potential future research works

Several potential future research topics could be valuable, based on this study.

- 1). Further extends the analysis by considering unsteady self-excitation forces and the study of flutter. Comparison of the unsteady model via flutter derivatives against the quasi-steady model with static coefficients.
- 2). Although the application of nonstationary inhomogeneous wind is illustrated by considering the Baluarte bridge, the actual nonstationary characteristics of the winds at the Baluarte bridge site are unknown. If wind measurements are available in the near

future, the statistical properties of these winds can be implemented into the finite element model.

- 3). The hurricane winds and thunderstorm winds may not be Gaussian. The non-Gaussian effect on the peak response of the Baluarte bridge would be unknown. This topic represents an innovative and attractive study for future research.
- 4). It would be desirable to secure funding to carry out full scale instrumentation of the Baluarte bridge and to measure the bridge responses to the wind. Moreover, a comparison of responses from the fullscale measurements, numerical modeling, and scaled full aeroelastic model test results is highly desirable to compare the pros and cons of each different approach.
- 5). A detailed wind hazard modeling and reliability assessment of the bridge is highly desirable for emergency preparedness planning.

4.2.1 Assessment of time history responses with nonstationary mean winds

An advantage of using the time domain approach is that it can cope with possible time-varying mean wind. In other words, it can be used to evaluate the responses of structures subjected to the nonstationary and non-homogenous wind field. To illustrate this, we consider that,

$$U_{mid} = \begin{cases} U_{mid0} & t < 60 \\ U_{mid0} + U_{mid1} \sin\left(\pi \frac{t-60}{180}\right) & 60 < t < 240, \\ U_{mid0} & 240 < t \end{cases} \quad (4.1)$$

where U_{mid0} and U_{mid1} are model parameters and t is in seconds.

A set of samples of the simulated time history at four points are shown in Figure 4.1 for $U_{mid0} = 10$ m/s and $U_{mid1} = 50$ m/s. By considering the sampled winds applied to the bridge, a time history analysis is carried out. The obtained time histories of the horizontal and vertical displacements at the midspan for the simulated winds (i.e., mean and fluctuating winds) are shown in Figure 4.1. For comparison purposes, the response obtained by considering the time-varying mean wind speed is also calculated and shown in Figure 4.2. The plots show that the displacements by including the fluctuating winds are greater than

those obtained by excluding the fluctuating nonstationary winds. The difference is most significant for the vertical displacement. It must be emphasized that this analysis is used for illustration purposes since the nonstationary winds that are applicable to the site are unknown. The numerical example is used to highlight the usefulness of the time-domain analysis in evaluating the bridge responses to nonstationary non-homogeneous winds.

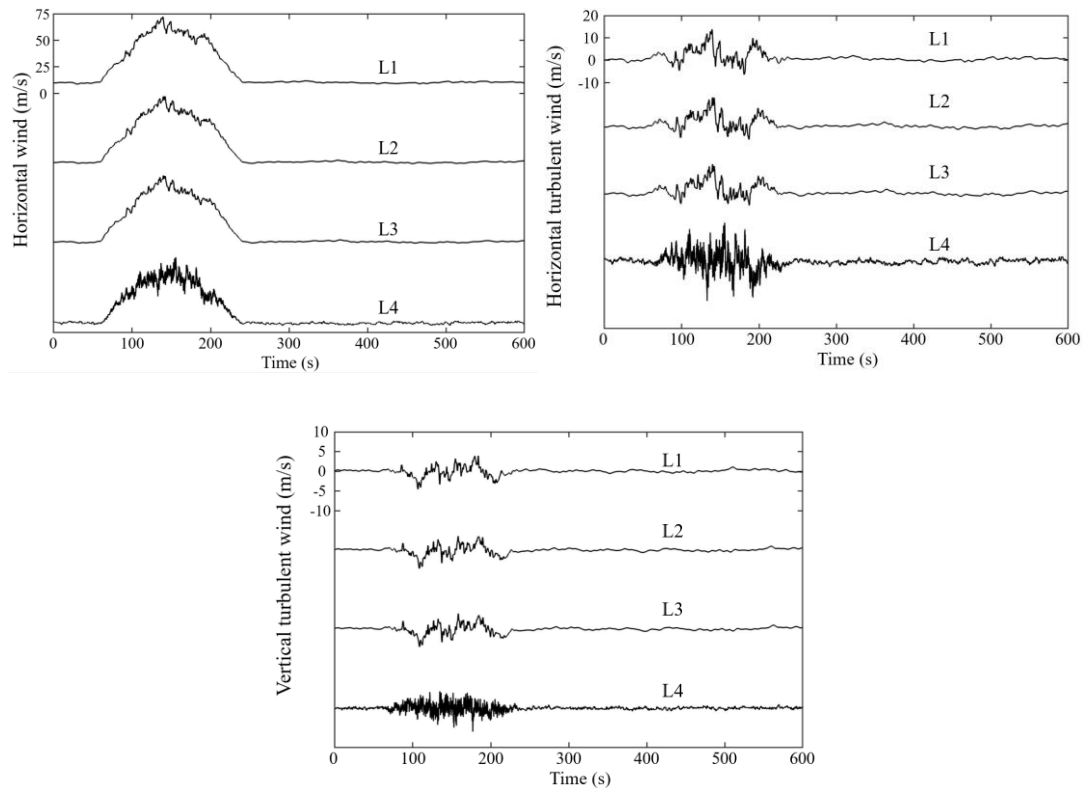


Figure 4.1 Samples nonstationary winds at a few selected locations: a) Mean and fluctuating wind, b) fluctuating horizontal wind, and c) fluctuating vertical wind.

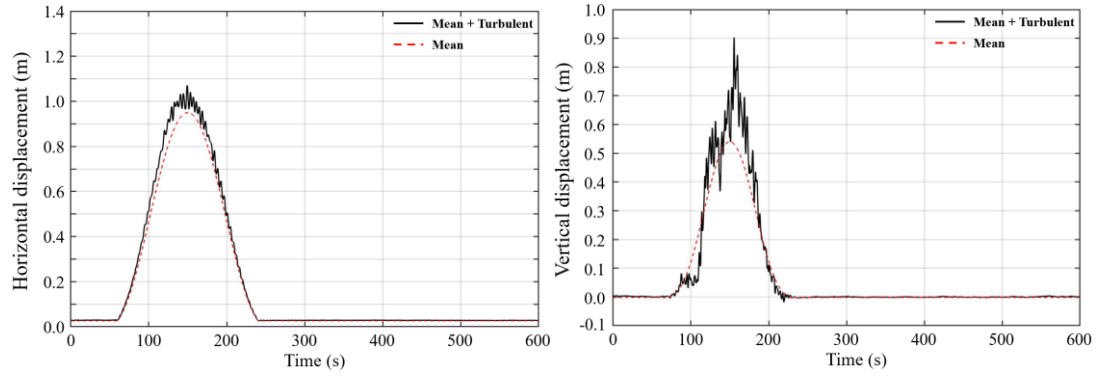


Figure 4.2 Calculated time histories of the displacements at midspan: a) horizontal displacement and b) vertical displacement.

5 Bibliography

- Aboshosha, H., Elshaer, A., Bitsuamlak, G.T. and El Damatty, A. (2015). Consistent inflow turbulence generator for LES evaluation of wind-induced responses for tall buildings. *Journal of Wind Engineering and Industrial Aerodynamics*, 142, 198-216.
- Amman, O. H., von Kármán, T., & Woodruff, G. B. (1941). The failure of the Tacoma Narrows bridge.
- ANSYS (2017). ANSYS multiphysics version 14.5. Ansys Inc., Canonsburg, PA.
- Barba, L.A., Leonard, A. and Allen, C.B. (2005). Advances in viscous vortex methods—meshless spatial adaption based on radial basis function interpolation. *International Journal for Numerical methods in Fluids*, 47,387-421.
- Beatke, F. and Werner, H. (1990). Numerical Simulation of Turbulent Flow over Surface-Mounted Obstacles with Sharp Edges and Corners. *Journal of Wind Engineering and Industrial Aerodynamics*, 35, 129-147.
- Billah, K. Y., & Scanlan, R. H. (1991). Resonance, Tacoma Narrows bridge failure, and undergraduate physics textbooks. *American Journal of Physics*, 59(2), 118-124.
- Boonyapinyo, V., Miyata, T., & Yamada, H. (1999). Advanced aerodynamic analysis of suspension bridges by state-space approach. *Journal of Structural Engineering*, 125(12), 1357-1366.
- Canadian Standards Association. (2019). *Canadian Highway Bridge Design Code (CAN/CSA S6-6)*, Toronto.
- Canadian Standards Association. (2014). *Canadian Highway Bridge Design Code (CAN/CSA S16-14)*, Toronto.
- Cao, Y., Xiang, H. and Zhou, Y. (2000). Simulation of Stochastic Wind Velocity Field on Long-Span Bridges. *Journal of Engineering Mechanics*, 126(1),1-6.
- Caracoglia, L. & Jones, N.P. (2003). Time domain vs. frequency domain characterization of aeroelastic forces for bridge deck sections. *J Wind Eng Ind Aerodyn*;91:371–402.
- Cermak, J. E. (1987). Advances in physical modeling for wind engineering. *Journal of Engineering Mechanics*, 113(5),737-756.

- Cermak, J. E. (1975). Application of fluid mechanics to wind engineering -A Freeman scholar lecture, *Journal of Fluids Engineering* -transactions of the ASME, 97(1),9-38.
- Cermak, J. E. (2003). Wind-tunnel development and trends in applications to civil engineering. *Journal of wind engineering and industrial aerodynamics*, 91(3), 355-370.
- Cermak, J.E., Sandborn, V.A., Plate, E.J., Binder, G.H., Chuang, H., Meroney, R.N., & Ito. S. (1966). Simulation of atmospheric motion by wind-tunnel flows. Colorado State University, Colorado, U.S.A.
- Chen, L., Letchford, C.W. (2007). Numerical simulation of extreme winds from thunderstorm downbursts. *Journal of Wind Engineering and Industrial Aerodynamics*, 95, 977-990.
- Chay, M.T., Albermani,F. and Wilson, R. (2006). Numerical and analytical simulation of downburst wind loads. *Engineering Structures*, 28, 240–254.
- Chen, X., Matsumoto, M., & Kareem, A. (2000a). Time domain flutter and buffeting response analysis of bridges. *Journal of Engineering Mechanics*, 126(1), 7-16.
- Chen, X., Matsumoto, M., Kareem, A., (2000b). Aerodynamic coupling effects on flutter and buffeting of bridges. *J. Eng. Mech.* 126, 17–26.
- Chen, X. and Kareem, A. (2002) Advances in modeling aerodynamic forces on bridge decks. *J Eng Mech, ASCE* 2002;128(11):1193–205.
- Chen, X. and Kareem, A. (2003). Aeroelastic Analysis of Bridges: Effects of Turbulence and Aerodynamic Nonlinearities. *Journal of Engineering Mechanics*, 129(8),:885-895.
- Chen, Z. Q., Han, Y., Hua, X. G., & Luo, Y. Z. (2009). Investigation on influence factors of buffeting response of bridges and its aeroelastic model verification for Xiaoguan Bridge. *Engineering Structures*, 31(2), 417-431.
- Chowdhury, A.G., & Sarkar, P.P. (2003) A new technique for identification of eighteen flutter derivatives using a three-degree-of-freedom section model. *Eng Struct*; 25(14):1763–72.
- Costa, C., Borri, C., Flaman, O., & Grillaud, G. (2007). Time-domain buffeting simulations for wind–bridge interaction. *Journal of Wind Engineering and Industrial Aerodynamics*, 95(9-11), 991-1006.
- Cramer, H. (1942). On harmonic analysis in certain functional spaces, *Arkiv Mat. Astron. Fysik*, 28B.

- Dagnew, A.K. and Bitsuamlak, G.T. (2013). Computational evaluation of wind loads on buildings: a review. *Wind and Structures*, 16(6), 629-660.
- Dai, H., Zheng, Z., & Ma, H. (2019). An explicit method for simulating non-Gaussian and non-stationary stochastic processes by Karhunen-Loève and polynomial chaos expansion. *Mechanical Systems and Signal Processing*, 115, 1-13.
- Davenport, A. G. (1962). Buffeting of a suspension bridge by storm winds. *Journal of the Structural Division*, 88(3), 233-270.
- Davenport, A.G. (1964). The buffeting of large superficial structures by atmospheric turbulence. *New York Acad Sci*, 116(2), 135–159.
- Davenport, A. F. (1965). The relationship of wind structure to wind loading. In *Proc. Conf. on Wind Effects on Buildings & Structures*, HMSO (Vol. 54).
- Davenport, A.G. (1966). The Action of Wind on Suspension Bridges A.G. Keynote Paper, *Intl. Symp. Suspension Bridges*, 1–39.
- Davenport, A. G. (1968). The Dependence of Wind Load on Meteorological Parameter. *Wind effects on building and structures*, 19-82.
- Davenport, A. G. (1983). Relationship of reliability to wind loading. *Journal of Wind Engineering and Industrial Aerodynamics*, 13(1–3), 3–27.
- Davenport A.G. (1981). Reliability of long span bridges under wind loading, *Proceedings of ICOSSAR*, Trondheim, Norway.
- Davenport, A.G., and Isyumov, N. (1967). The application of the boundary layer wind tunnel to the prediction of wind loads. *Proc. Intl. Sem. Wind effects on bldgs. and structs*, 1 (1), 201-230.
- Davenport, A.G., Isyumov, N., King, J.P.C., Novak, M., Surry, D., & B.J. & Vickery, (1985). BLWT II: The design and performance of a new boundary layer wind tunnel, in: *Proceedings of the Fifth US National Conference on Wind Engineering*, Texas Tech University, Lubbock, TX 1985, 2A35—39.
- Deodatis, G., & Shinozuka, M. (1989). Simulation of seismic ground motion using stochastic waves. *Journal of engineering mechanics*, 115(12), 2723-2737.
- Diana, G., Fiammenghi, G., Belloli, M., & Rocchi, D. (2013). Wind tunnel tests and numerical approach for long span bridges: The Messina bridge. *Journal of Wind Engineering and Industrial Aerodynamics*, 122, 38-49.

- Diana, G., Falco, M., Bruni, S., Cigada, A., Larose, G.L., Damsgaard, A. and Collina, A. (1995). Comparison between wind tunnel tests on a full aeroelastic model of the proposed bridge over Stretto di Messina and numerical results. *Journal of Wind Engineering and Industrial Aerodynamics*, (54/55),101-113.
- Diana, G., Cheli, F., Zasso, A., Collina, A. and Brownjohn, J. (1992). Suspension bridge parameter identification in full scale test. *Journal of Wind Engineering and Industrial Aerodynamics*, (41-44), 165-176.
- Di Paola, M. (1998). Digital simulation of wind field velocity. *Journal of wind engineering and industrial aerodynamics*, (74-76), 91-109.
- Falco, M., Curami, A. and Zasso, A. (1992). Nonlinear effects in sectional model aeroelastic parameters identification. *Journal of Wind Engineering and Industrial Aerodynamics*, (41/44),1321-1332.
- Flamand, O. (2003) Wind Tunnel Tests on the Baluarte Bridge. EN-CAPE 03-121 – V0, Centre Scientifique et technique du Bâtiment, CSTB, Nantes.
- Frandsen, J.B. (2004). Numerical bridge deck studies using finite elements. Part I: flutter. *Journal of Fluids and Structures*, 19, 171–191.
- Ghanem, R.G., & Spanos, P.D. (2003). *Stochastic finite elements: a spectral approach*. Courier Corporation.
- Grigoriu, M., Ruiz, S.E. and Rosenblueth, E. (1988, July 15). Nonstationary Models of Seismic Ground Acceleration. NCEER-88-0043.
- Grinderslev, C., Lubek, M. and Zhang, Z. (2018). Nonlinear fluid-structure interaction of bridge deck: CFD analysis and semi-analytical modeling. *Wind and Structures*, 1-23.
- Gu, M., Zhang, R.X., & Xiang, H.F. (2001) Parametric study on flutter derivatives of bridge decks. *Eng Struct*;23(12):1607–13.
- Hangan, H. (2014). The wind engineering energy and environment (WindEEE) dome at Western University, Canada. *Wind Engineers, JAWWE*, 39(4), 350-351.
- Hu, Z. (2009). Gust responses of bridges to spatially varying wind excitations and calibration of wind load factors. Master thesis, The University of Western Ontario, London, ON, Canada.

- Hu, Z., Hong, H. P., & King, J. P. C. (2011). Sensitivity of gust responses of bridges to spatio-temporal varying wind excitations. *Canadian Journal of Civil Engineering*, 38(9), 963-973.
- Hua, X. G., Chen, Z. Q., Ni, Y. Q., & Ko, J. M. (2007). Flutter analysis of long-span bridges using ANSYS. *Wind and Structures*, 10(1), 61-82.
- Huang, G., & Chen, X. (2009). Wavelets-based estimation of multivariate evolutionary spectra and its application to nonstationary downburst winds. *Engineering Structures*, 31(4), 976-989.
- Huang, S.H., Li, Q.S. and Wu, J.R. (2010). A general inflow turbulence generator for large eddy simulation. *Journal of Wind Engineering and Industrial Aerodynamics* , 98, 600-617.
- Hui, M. C., & Michael C.H. and Hui, D. (2010). The Aerodynamic Behaviour of the Deck of Stonecutters Bridge, Hong Kong. *Structural Engineering International*, 79-90.
- Hui, M.C.H. (2013). Full-bridge aeroelastic model wind tunnel tests for the Stonecutters Bridge. *HKIE Transactions*, 20:2, 109-123.
- Hong, H. P. (2016). Modeling of Nonstationary Winds and Its Applications. *Journal of Engineering Mechanics*, 142(4),1-11.
- Jain, A., Jones, N. P., & Scanlan, R. H. (1998). Effect of modal damping on bridge aeroelasticity. *Journal of Wind Engineering and Industrial Aerodynamics*, 77, 421-430.
- Jain, A., Jones, N.P. and Scanlan, R.H. (1996). Coupled flutter and buffeting analysis of long-span bridges. *Journal of Structural Engineering*, 122(7), 716-725.
- Jakobsen, J.B. (1997). Span-wise structure of lift and overturning moment on a motionless bridge girder. *Journal of Wind Engineering and Industrial Aerodynamics* , (69-71), 795-805.
- Kaimal, J. C., Wyngaard, J. C. J., Izumi, Y., & Coté, O. R. (1972). Spectral characteristics of surface-layer turbulence. *Quarterly Journal of the Royal Meteorological Society*, 98(417), 563-589.
- Kareem, A. (2008). Numerical simulation of wind effects: a probabilistic perspective. *Journal of wind engineering and insdustrial aerodynamics*, 96,1472-1497.

- Katsuchi, H., Jones, N.P., Scanlan, R.H. and Akiyama, H. (1998). A Study of Mode Coupling in Flutter and Buffeting of the Akashi-Kaikyo Bridge. *J. Struct. Mech. Earthquake Eng.*, No. 598,1-44.
- Kavrakov, I., Legatiuk, D., Gürlebeck, K., & Morgenthal, G. (2019). A categorical perspective towards aerodynamic models for aeroelastic analyses of bridge decks. *Royal Society Open Science*, 6(3).
- Katsuchi, H. (1998). A study of mode coupling in flutter and buffeting of Akashi-Kaykyo bridge. *Structural Eng. /Earthquake Eng.*, JSCE, 15(2), 175-190.
- Kimura, K., Fujino, Y., Nakato, S. and Tamura, H. (1997). Characteristics of buffeting forces on fiat cylinders . *Journal of Wind Engineering and Industrial Aerodynamics*, (69-71),365-374.
- King, J. P. C. and Kong, L., 2010. A Study of wind effects for Baluarte Bridge, Mexico, The University of Western Ontario, Faculty of Engineering, Science Research Report, BLWT-SS5-2010.
- King, J. P. C., Kong, L., Gómez-Martínez, R., Pozos-Estrada, A., & Sánchez-García, R. (2011). Experimental and analytical evaluation of the aeroelastic behavior of the Baluarte bridge. In *Proceedings of the 13th International Conference on Wind Engineering*, July (pp. 10-15).
- Kuroda, S. (1997). Numerical simulation of flow around a box girder of a long span suspension bridge . *Journal of Wind Engineering and Industrial Aerodynamic*, 67&68, 239-252.
- Larose, G.L., Davenport, A.G. and King, J.P.C. (1992). Wind Effects on Long Span Bridges: Consistency of Wind Tunnel Results. *Journal of Wind Engineer:ng and Industrial Aerodynamic*, 41-44, 1191-1202.
- Larose, G.L. and Mann, J.(1998). Gust Loading on Streamlined Bridge Decks. *Journal of Fluids and Structures*, 12, 511-536.
- Larsen, A. (1993). Aerodynamic aspects of the final design of the 1624 m suspension bridge across the Great Belt. *Journal of Wind Engineering and Industrial Aerodynamics*, 48, 261-285.

- Larsen, A. and, Walther, J.H. (1997). Aeroelastic analysis of bridge girder sections based on discrete vortex simulations . *Journal of Wind Engineering and Industrial Aerodynamics*, 67&68, 253- 265 .
- Li, S., Li, M. and Larose, G.L. (2018). Aerodynamic admittance of streamlined bridge decks. *Journal of Fluids and Structures*, 78,1-23.
- Macdonald. J.H.G.(2003). Evaluation of buffeting predictions of a cable-stayed bridge from full-scale measurements. *Journal of Wind Engineering and Industrial Aerodynamics*, 1465–1483.
- Madsen, H. O., Krenk, S., & Lind, N. C. (2006). *Methods of structural safety*. Courier Corporation.
- Mignolet, M. P., & Spanos, P. D. (1992). Simulation of homogeneous two-dimensional random fields: Part I—AR and ARMA models.
- Miyata T, Yamada H, Boonyapinyo V, Santos JC. Analytical investigation on the response of a very long suspension bridge under gust wind. In: *Proceedings of ninth international conference on wind engineering*. 1995. p. 1006–17.
- Murakami, S. and, Mochida, A. (1995). On turbulent vortex shedding flow past 2D square cylinder predicted by CFD . *Journal of Wind Engineering and Industrial Aerodynamics*, 54/55, 191-211.
- Newland, D. E. (2012). *An introduction to random vibrations, spectral & wavelet analysis*. Courier Corporation.
- NRC (2010) *National Building Code of Canada*. Institute for Research in Construction, National Research Council of Canada, Ottawa
- Patrino, L. (2015). Accuracy of numerically evaluated flutter derivatives of bridge deck sections using RANS: Effects on the flutter onset velocity. *Engineering Structures*, 89, 49-65.
- Phoon, K.K., Huang, S.P., and Quek, S.T. (2002). Simulation of second-order processes using Karhunen–Loeve expansion. *Computers and Structures*, 80(12), 1049-1060.
- Pozos-Estrada, A., Flores, R., & Gómez, R. (2016). Parametric study of stay cables of a bridge under simulated spatially correlated turbulent wind. *Latin American Journal of Solids and Structures*, 13, 1450-1463.

- Priestley, M. B. (1965). Evolutionary spectra and non-stationary processes. *Journal of the Royal Statistical Society: Series B (Methodological)*, 27(2), 204-229.
- Priestley, M.B. (1967). Power Spectral Analysis of Non Stationary Random Processes. *Journal of Sound Vibration*, 6(1), 86-97.
- Salvatori, L., & Borri, C. (2007). Frequency-and time-domain methods for the numerical modeling of full-bridge aeroelasticity. *Computers & structures*, 85(11-14), 675-687.
- Sankaran. R. and Jancauskas, E.D. (1993). Measurements of cross-correlation in separated flows around bluff cylinders . *Journal of Wind Engineering and Industrial Aerodynamics*, 49, 279-288.
- Salvatori, L., & Borri, C. (2007). Frequency-and time-domain methods for the numerical modeling of full-bridge aeroelasticity. *Computers & structures*, 85(11-14), 675-687.
- Salvatori, L. & Spinelli, P. (2007). A discrete 3D model for bridge aerodynamics and aeroelasticity: nonlinearities and linearizations. *Meccanica*, (42), 31-46.
- Sarkar, P.P., Jones, N.P. and Scanlan, R.H. (1992). Identification of Aeroelastic Parameters of Flexible Bridges. *Journal of Engineering Mechanics*, 120(8),1718-1742.
- Sarrate, J., Huerta, A. and Donea, J. (2001). Arbitrary Lagrangian-Eularian formulation for fluid-rigid body interaction. *Computer methods in applied Mechanics and Engineering*, 190,1371-3188.
- Scanlan, R.H., (1983). Aeroelastic simulation of bridges. *Journal of Structural Engineering*, 109(12), 2829-2837.
- Scanlan, R. H. (1978). The action of flexible bridges under wind, I: flutter theory. *Journal of Sound and Vibration*, 60(2), 187-199.
- Scanlan, R. H., Béliveau, J. G., & Budlong, K. S. (1974). Indicial aerodynamic functions for bridge decks. *Journal of the Engineering Mechanics Division*, 100(4), 657-672.
- Scanlan RH, & Tomko A. (1971). Airfoil and bridge deck flutter derivatives. *J Eng Mech.;* 97:1717–37.
- Shields, M.D., & Deodtis, G. (2013). A simple and efficient methodology to approximate a general non-Gaussian stationary stochastic vector process by a translation process with applications in wind velocity simulation, *Engineering Mechanics*, 31, 19-29
- Shields, M.D., & Kim, H. (2017). Simulation of higher-order stochastic processes by spectral representation. *Probabilistic Engineering Mechanics*, 47, 1-15.

- Shinozuka, M. (1972). Monte Carlo solution of structural dynamics. *Computer & Structures*, 2, 855-874.
- Shinozuka, M., & Deodatis G. (1996). Simulation of multi-dimensional Gaussian stochastic fields by spectral representation. *Appl Mech Rev.*; 49(1):29–53.
- Shinozuka, M., & Jan, C. M. (1972). Digital simulation of random processes and its applications. *Journal of sound and vibration*, 25(1), 111-128.
- Simiu, E., & Scanlan, R.H. (1996). *Wind effects on structures,-Fundamentals and application to design*, John Wiley, New York.
- Simiu, E., & Yeo, D. (2019). *Wind effects on structures: Modern structural design for wind*. John Wiley & Sons.
- Solari., G. (1987). Turbulence modeling for gust loading. *Journal of Structural Engineering*, 1550-1569.
- Smirnov, A., Shi, S. and Celik, I. (2001). Random Flow Generation Technique for Large Eddy Simulations and Particle-Dynamics Modeling. *Journal of Fluids Engineering*, ASME, 123, 359-371.
- Song, Y., Chen, J., Peng, Y., Spanos, P.D. and Li, J.(2018). Simulation of nonhomogeneous fluctuating wind speed field in two-spatial dimensions via an evolutionary wavenumber-frequency joint power spectrum. *Journal of Wind Engineering & Industrial Aerodynamics*, 250-259.
- Spanos, P.D. and Zeldin, B.A. (1998). Monte Carlo treatment of random fields: A broad perspective . *American Society of Mechanical Engineers* , 51(3),219-237.
- Spanos, P. D., Beer, M., & Red-Horse, J. (2007). Karhunen–Loève expansion of stochastic processes with a modified exponential covariance kernel. *Journal of Engineering Mechanics*, 133(7), 773-779.
- Strømmen, E. (2010). *Theory of bridge aerodynamics*. Springer Science & Business Media.
- Sun, D. K., Xu, Y. L., Ko, J. M., & Lin, J. H. (1999). Fully coupled buffeting analysis of long-span cable-supported bridges: Formulation. *Journal of Sound and Vibration*, 228(3), 569–588.

- Tamura, Y. and Phuc, P.V. (2015) Development of CFD and applications: Monologue by a non-CFD-expert. *Journal of Wind Engineering and Industrial Aerodynamic*, 144, 3-13.
- Turkiyyah, G., R. Y. (1995). Fast vortex methods for predicting wind-induced pressures on buildings . *Journal of Wind Engineering and Industrial Aerodynamic*, 58, 51-79.
- Wardlaw, R. (1980). Sectional versus full model wind tunnel testing of bridge road decks. *Proceedings of the Indian Academy of Sciences Section (pp. 3, 177-198). India: Engineering Sciences.*
- Witting, L.E. and Sinha, A.K. (1975). Simulation of multicorrelated random processes using the FFT algorithm. *The Journal of the Acoustical Society of America*, 58 (3), 630-634.
- Xu, Y.L., Sun, D.K., Ko, J.M., & Lin, J.H. (1998) Buffeting analysis of long span bridges: A new algorithm. *Comput Struct*; 68(4):303–13.
- Yang, J.N. (1972). Simulation of Random Envelope Processes. *Journal of Sound and Vibration*, 73-85.
- Yang, W.W., Chang, T.Y.P. and Chang, C.C. (1997). An efficient wind field simulation technique for bridges. *Journal of Wind Engineering and Industrial Aerodynamics*, (67/68), 697-708.

Appendix A Preliminary analysis of the deck girder from the Baluarte bridge by CFD

The strip assumption considers that the span-wise structure of turbulence can represent the span-wise structure of the associated forces on a line-like structure, and that the wind coherence is equivalent to the coherence of wind forces. This simplification must be acknowledged, to gain a certain perspective associated with the possible drawbacks of the theory. A simple example for this purpose is presented in the following by means of the Commercial Computational fluid dynamics (CFD) package STAR-CCM+. The steady analysis of the flow is solved, and the instantaneous velocity field around the deck cross section of the Baluarte bridge is presented in Fig A.1. The velocity profile for the Reynolds-averaged Navier-Stokes (RANS) simulation is defined by a power law, with an α equal to 0.15, and a mean wind velocity at the height of the girders equal to 36.24 m/s. By only considering the steady component of the wind, a huge and complex variation in the velocity contours is observed. In this case, the wind speeds throughout the girder contour range from -8 to 45 m/s. The girder cross section in this case is the original bridge cross section without baffles and deflectors. The visualization of the flow highlights the complexities associated to the wind flow flowing throughout the girder contour. The visual inspection of the wind flow puts into perspective the complex structure associated to the wind forces. Further, if careful insight and evaluation are not considered the line-like structure concept used in the quasi-steady theory could misinterpret the complexities of the actual fluid flow complexity.

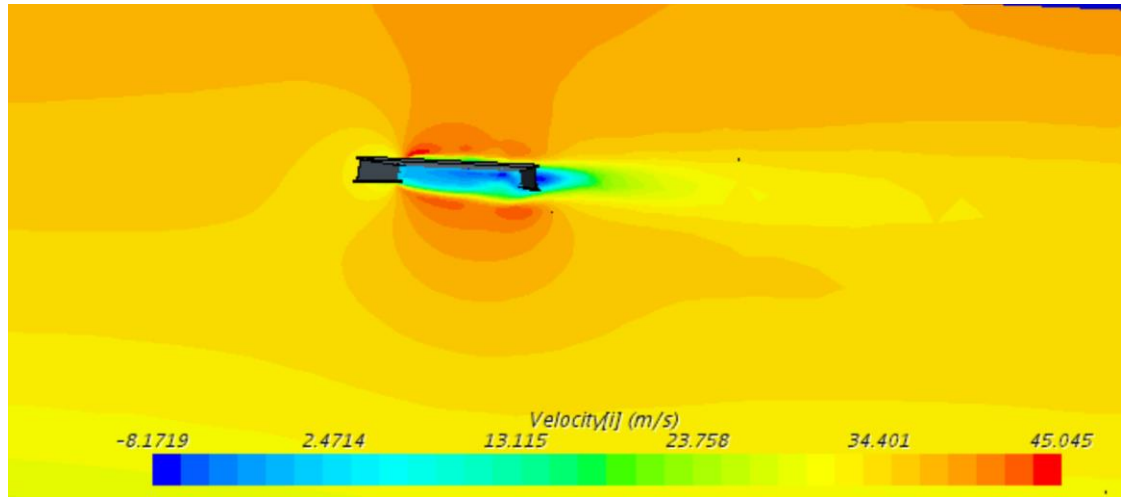


Figure A.1 RANS simulation for the mid-span cross section of the Baluarte bridge, for a mean wind velocity of 36.24 m/s.

The shape of the girder is an important aspect in the study of the aerodynamic behavior of the bridge. The strip assumption, which is considered under the line-like structure, is just a simplification of a complex problem that involves separation, reattachment, and recirculation of the wind flow. Even though this study is not particularly concerned with the study of a CFD model, it is important to consider its actual contribution that CFD is having on wind engineering.

Appendix B Preliminary analysis of the wind hazard for the country of Mexico

B.1 Introduction

The regional wind speeds could be defined as the most probable maximum wind velocities that are expected over a specific return period. For the development of regional maps, it is of common practice to define the characteristics of the wind as homogeneous conditions. Therefore, a standard roughness and a standard height of the anemometer are considered. The standard height of the anemometer is ten meters, while the standard roughness corresponds to open country exposure. The records are also classified by the number of years of measured data, the lapse of the average of the wind speed, and the quality of the wind records. Besides, the regional map of wind speeds for Mexico is presented as a three-second gust wind speed map. The wind speeds without roughness correction, and before being standardized as homogeneous conditions, are retarded on account of frictional forces near the ground surface.

The regional map of wind velocities for Mexican standards includes the analysis of synoptic type of wind and a combination of synoptic wind and hurricane for the coastal regions. For the analysis of hurricanes, the maximum wind speed is determined from the reconstruction of paths and intensities from the hurricane database. For the analysis of synoptic wind, the mean annual maximum wind speed is defined based on an extreme value analysis for a predefined return period. The return period is based on the range of importance of the structure and can vary significantly from a preliminary construction stage with a small return period, to a highly important category for service stage. In the last case, the damage of the structure can cause great economic or life losses.

Another important aspect in the development of regional maps is the inspection of the actual quality of the available data. The datasets are filtered in regards to different sources of error, that is associated to the quality of equipment in use. The main objective of the present study is to identify the different sources of errors within the meteorological database, and to incorporate a statistical extreme value analysis for the incorporation

of maximum wind speeds. For the extreme value analysis, the Gumbel and the Generalized extreme value (GEV) distribution (Gumbel, 2004) are used for the prediction of the mean annual maximum wind speed. In order to reduce an excessive amount of information within this study, only the 200-year mean annual maximum wind speed is considered for the investigation. Structures studied under this category, are structures considered under group A (CFE, 2008), by CFE (Comisión Federal de Electricidad) standards. The damage of such infrastructure can cause important life loss or exceptional cultural or cost losses, therefore these type of structures have a highly elevated level of security.

B.2 General background

Based on previous studies, in the year 1993 an update of the existing CFE Wind Design Handbook was conducted, incorporating new data and reviewing formulations and procedures of the wind design handbook (CFE, 2008). The statistical procedures for the analysis of wind speeds are described in López (1995). Originally, 57 meteorological stations are considered for the statistical analysis of gust wind speeds. The regional maps for the country of Mexico are updated and organized, and include both synoptic and hurricane type of winds. For the analysis of hurricanes, a fluid dynamic model (Aguirre, 1986) is used to determine hurricane wind speeds, on the Pacific coast, the Gulf of Mexico, and the Caribbean coast.

Based on the regional map from CFE (CFE, 2008), in Fig B 1 is reproduced the 200 year mean annual maximum wind speed. The isopleths within the regional map are divided into five different categories associated to the levels of risk. The homogeneous conditions considered within the regional map include the three-second maximum gust wind speed, ten meters height measurements and the standardization of the roughness into open country exposure. Within the CFE map, the highest risk level is observed near the coastal regions on the Pacific Coast and the Gulf of Mexico. Baja California Sur in the former case and Yucatan and Quintana Roo in the later. Both zones are highly susceptible to the constant landing of hurricanes, depicted by the red zones within the CFE map. Another highly

susceptible zone is located between the boarder of U.S.A and the states of Coahuila, Nuevo Leon, and Tamaulipas. Even though, the wind speeds are not as critical as those generated under the red zone, their values still oscillate between 160 and 195 km/h. This zone also include part of the coasts from the states of Tamaulipas, and Veracruz on the side of the Gulf of Mexico, and a small portion of land from Sinaloa , Michoacán and Colima from the Pacific Coast side.

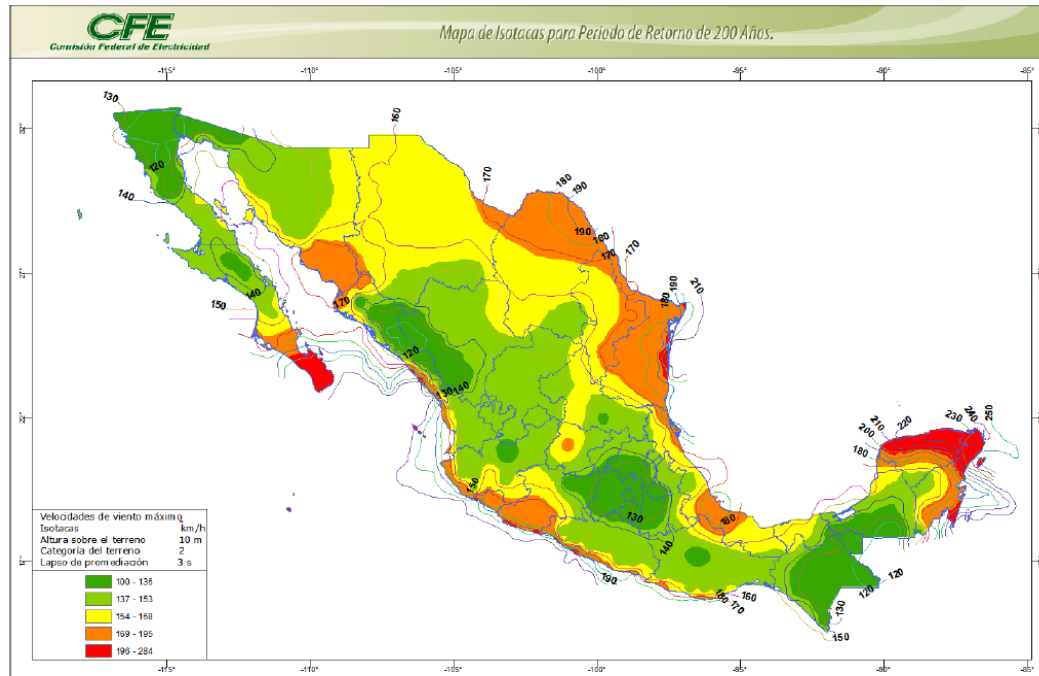


Figura 4.2.1 Mapa de isotacas para velocidades regionales con periodo de retorno de 200 años.

Figure B 1 Regional velocities from CFE-2008, $Tr=200$ years.

Another regional map apart from the one of CFE was proposed in the year 2015, by the institution's SEP and INIFED (Institution of Public Education and Educative Infrastructure, by their acronym in Spanish) (INIFED, 2015). Since the database has increased from 74 stations in the year 2003 to 172 stations in 2017 (Lopez et al. 2018), there is a considerable difference between the regional map presented by CFE (CFE, 2008) and that one presented by SEP and INIFED.

The shape of the isopleths and the mean annual maximum wind speed can differ from case to case depending on the number of stations used in the study, on the level of refinement and on the quality control of the study. One of the limitations of this study is

that no separation by wind direction or azimuthal bins are considered. If the direction of the wind is considered, a more precise prediction of maximum wind speeds can be expected. However, from the inspected datasets a great number of stations can be synthesised under homogeneous characteristics of topography, when in the periphery of the station a homogeneous terrain is presented.

B.3 Categorization of data and predicting models

A general overview of the procedure used to categorize wind speed records is presented. In this case, erroneous measurements are identified and extracted from the original record. The downloaded information consist of meteorological station with at least 20 years of available data. The records are found at the National Center of Environmental Information (NOAA), at the website: <https://gis.ncdc.noaa.gov/maps/ncei/cdo/hourly>. One of the most common errors found within the records is not enough continuity of records for a particular period (months or years), or for a particular lapse of time. For instance, a discontinuity related to the density of annual records between the years 1960-1990, is found for the station of Monclova, Coahuila (Fig B 2). In this case, in order to guarantee continuity within the the station, years prior to 1991 are extracted from the record. Thus, only years between 1991 and 2017 are considered.

763420	99999	MONCLOVA	INTL	1956	248	229	247	240	248	240	247	248	240	248	239	248
763420	99999	MONCLOVA	INTL	1957	248	224	248	240	247	239	248	247	240	248	240	248
763420	99999	MONCLOVA	INTL	1958	247	224	248	240	248	240	248	248	240	248	240	248
763420	99999	MONCLOVA	INTL	1959	248	224	248	240	248	240	248	248	240	248	240	248
763420	99999	MONCLOVA	INTL	1960	247	232	248	0	0	0	0	0	0	0	0	0
763420	99999	MONCLOVA	INTL	1973	166	91	129	91	33	39	38	47	46	44	49	50
763420	99999	MONCLOVA	INTL	1974	81	52	50	51	45	41	51	62	47	63	65	49
763420	99999	MONCLOVA	INTL	1975	66	56	60	53	41	68	72	55	72	72	81	80
763420	99999	MONCLOVA	INTL	1976	96	85	80	71	76	62	63	74	71	78	65	29
763420	99999	MONCLOVA	INTL	1977	66	68	69	71	68	81	71	70	69	70	72	66
763420	99999	MONCLOVA	INTL	1978	73	55	79	76	78	79	101	113	98	115	97	103
763420	99999	MONCLOVA	INTL	1979	111	91	114	82	100	101	109	88	92	99	94	91
763420	99999	MONCLOVA	INTL	1980	95	88	110	94	105	97	101	100	107	103	98	108
763420	99999	MONCLOVA	INTL	1981	103	96	111	94	78	75	102	113	97	105	99	91
763420	99999	MONCLOVA	INTL	1982	98	92	97	104	100	93	79	90	102	109	106	98
763420	99999	MONCLOVA	INTL	1983	87	94	103	100	106	109	97	89	97	106	95	102
763420	99999	MONCLOVA	INTL	1984	84	93	101	100	98	97	85	78	98	88	98	98
763420	99999	MONCLOVA	INTL	1985	88	88	105	98	99	91	101	90	66	27	71	41
763420	99999	MONCLOVA	INTL	1986	51	72	72	83	80	46	48	57	60	63	57	38
763420	99999	MONCLOVA	INTL	1987	49	36	46	39	39	35	54	67	49	59	50	54
763420	99999	MONCLOVA	INTL	1988	45	57	57	55	58	56	46	40	34	42	68	67
763420	99999	MONCLOVA	INTL	1989	46	51	134	79	104	86	91	127	59	112	63	37
763420	99999	MONCLOVA	INTL	1990	60	112	111	56	66	68	26	50	53	56	35	57
763420	99999	MONCLOVA	INTL	1991	143	124	149	135	149	79	153	145	138	123	136	131
763420	99999	MONCLOVA	INTL	1992	128	184	177	185	165	135	154	179	170	170	159	150
763420	99999	MONCLOVA	INTL	1993	138	151	194	192	215	197	203	202	179	169	180	166
763420	99999	MONCLOVA	INTL	1994	176	144	163	160	182	181	157	164	175	180	178	180
763420	99999	MONCLOVA	INTL	1995	186	202	225	218	229	214	193	194	339	331	442	333
763420	99999	MONCLOVA	INTL	1996	438	398	396	383	292	385	407	401	394	418	368	322
763420	99999	MONCLOVA	INTL	1997	385	355	413	340	330	307	320	315	365	435	455	450
763420	99999	MONCLOVA	INTL	1998	400	417	377	415	444	420	377	389	395	327	305	296
763420	99999	MONCLOVA	INTL	1999	420	460	553	492	494	479	493	506	472	487	507	518
763420	99999	MONCLOVA	INTL	2000	555	526	576	540	571	561	595	555	568	583	528	572
763420	99999	MONCLOVA	INTL	2001	586	531	541	533	517	526	547	544	538	557	540	554
763420	99999	MONCLOVA	INTL	2002	589	516	550	554	580	532	536	556	560	575	598	579
763420	99999	MONCLOVA	INTL	2003	580	441	559	551	612	575	598	552	561	577	541	531
763420	99999	MONCLOVA	INTL	2004	548	528	525	558	472	533	560	571	530	517	482	460
763420	99999	MONCLOVA	INTL	2005	463	439	516	488	503	502	472	449	473	481	481	501
763420	99999	MONCLOVA	INTL	2006	499	442	560	508	544	555	582	520	519	566	525	565
763420	99999	MONCLOVA	INTL	2007	552	505	576	558	559	539	538	565	555	569	571	563
763420	99999	MONCLOVA	INTL	2008	577	521	487	518	528	543	592	553	532	560	514	564
763420	99999	MONCLOVA	INTL	2009	557	520	532	529	510	510	492	581	562	572	548	560
763420	99999	MONCLOVA	INTL	2010	562	471	570	438	522	523	462	569	580	577	566	577
763420	99999	MONCLOVA	INTL	2011	617	562	582	567	568	453	566	596	567	588	516	502
763420	99999	MONCLOVA	INTL	2012	510	452	395	385	425	459	340	458	408	423	495	420
763420	99999	MONCLOVA	INTL	2013	487	443	523	505	473	506	526	513	490	507	494	499
763420	99999	MONCLOVA	INTL	2014	509	457	442	518	491	432	446	495	455	438	454	512
763420	99999	MONCLOVA	INTL	2015	487	455	505	489	468	456	449	415	394	439	436	343
763420	99999	MONCLOVA	INTL	2016	392	418	457	478	472	425	483	511	500	548	522	555
763420	99999	MONCLOVA	INTL	2017	519	469	516	490	532	478	470	500	532	546	506	504

Figure B 2 Monthly records from the year 1956 to 2017, for the station of Monclova, Coahuila.

A similar analysis is carried out for the daily registered records. In this case, in order to guarantee the continuity within the records, an individual measurement that is separated from the rest in more than 3 hours is extracted out of the records compiled on that day. Again, an example is presented for the station of Monclova, Coahuila in Fig. B 3. In this case, the records from the day 2017-05-15 registered at 0:00 and 3:00 hr are extracted from the measurements registered on that day. In contrast, the day 2017-05-16 did not present any anomaly.

Identification							WIND				
USAF	NCDC	Date	HrMn	I	Type	QCP	Dir	Q	I	Spd	Q
763420	99999	20170415	0000	4	FM-12		,090	1	N	3.0	1
763420	99999	20170415	0300	4	FM-12		,360	1	N	2.0	1
763420	99999	20170415	1140	4	FM-15		,120	1	N	4.1	1
763420	99999	20170415	1200	4	FM-12		,210	1	N	2.0	1
763420	99999	20170415	1240	4	FM-15		,120	1	N	4.1	1
763420	99999	20170415	1500	4	FM-12		,320	1	N	1.0	1
763420	99999	20170415	1740	4	FM-15		,090	1	N	3.1	1
763420	99999	20170415	1800	4	FM-12		,360	1	N	1.0	1
763420	99999	20170415	2100	4	FM-12		,360	1	N	1.0	1
763420	99999	20170416	0000	4	FM-12		,360	1	N	1.0	1
763420	99999	20170416	0300	4	FM-12		,200	1	N	3.0	1
763420	99999	20170416	0600	4	FM-12		,160	1	N	2.0	1
763420	99999	20170416	0900	4	FM-12		,210	1	N	1.0	1
763420	99999	20170416	1200	4	FM-12		,310	1	N	1.0	1
763420	99999	20170416	1244	4	FM-15		,080	1	N	2.6	1
763420	99999	20170416	1348	4	FM-15		,080	1	N	3.1	1
763420	99999	20170416	1440	4	FM-15		,080	1	N	3.1	1
763420	99999	20170416	1500	4	FM-12		,090	1	N	2.0	1
763420	99999	20170416	1640	4	FM-15		,999	9	C	0.0	1
763420	99999	20170416	1740	4	FM-15		,080	1	N	2.6	1
763420	99999	20170416	1800	4	FM-12		,010	1	N	2.0	1
763420	99999	20170416	1845	4	FM-15		,040	1	N	2.6	1
763420	99999	20170416	1940	4	FM-15		,040	1	N	2.6	1
763420	99999	20170416	2100	4	FM-12		,050	1	N	2.0	1
763420	99999	20170416	2146	4	FM-15		,010	1	N	8.2	1

Figure B 3 Wind speed records, for the days 15 and 16 of May 2017, from the station of Monclova, Coahuila.

Since only information related to synoptic wind is considered in the analysis of wind records, wind speeds above 120 km/h are extracted from the datasets. Considering that hurricanes are extremely rare events, and since it is hard to conceive that an anemometer can registering such an event, it is recommended to corroborate such an event with the actual hurricane database. The hurricane database is available at <https://www.nhc.noaa.gov/data/#hurdat>.

The original datasets for investigation consisted in stations with at least 20 years of available data obtained from the NOAA website. The first dataset was constituted by 115 stations from Mexico, 100 stations from U.S.A., 9 from Guatemala, and 2 from Belize. The location of all the meteorological stations of this first dataset is presented in Fig B 4, below.



Figure B 4 Downloaded datasets from NOAA (the download year: 2017).

From this first arrangement of stations, all the datasets were analysed and fitted into the Gumbel or the GEV distribution. The datasets that were able to best fit within any of the two types distributions were chosen and presented as best datasets(Fig. B 5). In this case, a total of 89 stations were considered for the extreme value analysis. From these stations, 56 stations are located in Mexico, 28 stations are located in U.S.A., 4 stations in Guatemala, and 1 in Belize. In the case of the stations from the U.S.A., the considered datasets belong to the automated surface observation system (ASOS), dataset 9956, available at the National Climatic Data Center (NCDC, 2006).



Figure B 5 Selected stations with the best datasets for the 200-year mean annual maximum wind speed.

First, the Gumbel distribution (Kimball, 1955) is used for the extreme value analysis. The Gumbel distribution (Martins, 2000), or extreme value distribution Type 1 is:

$$F_X(x) = \exp(-\exp(-y)) \quad (\text{B.1a})$$

$$y = \frac{(x-u)}{\alpha} \quad (\text{B.1b})$$

where $F_X(x)$ is the cumulative distribution function (c.d.f.), x the variate, and y the reduced variate. The parameters that map the variate x into the reduced variate y , are the location parameter u and the scale parameter α . Generally, $F_X(x)$ is expressed in terms of the probability of exceedance and the return period. In the case of the 200-year return period, the risk or probability of exceedance is 0.005, and the return period can be expressed as,

$$T_r = \frac{1}{1-F_X(x)} \quad (\text{B.2})$$

By substituting Eq. B.2 into Eq. B.1, and by replacing the variate x for the wind speed at the height z (10 meters in theory, however such information needs to be corroborated):

$$U_z = u - \frac{1}{\alpha} \left\{ \ln \left(\ln \left(1 - \frac{1}{T_r} \right) \right) \right\} \quad (\text{B.3})$$

For the extreme value analysis, all observed annual maxima are ranked as $G_i (= m/(N + 1))$; where m is the rank of the observation, and N the total number of observations. There are other ways recommended for an unbiased plotting, such as $(m - 0.44)/(N + 0.12)$, originally proposed by Palutikof, (1999). Nevertheless, the predicted values of the mean annual maximum wind speed tend to be conservative.

The analysis of the Gumbel probability paper for representative meteorological stations is presented in section B 7, at the end of this Appendix. In the Gumbel probability paper the ordinate represents the linearization of the probability of exceedance and the abscissa the annual maxima for wind speeds. For the Gumbel distribution, the method of moments (MOM) and the least square method (LSM) are used for fitting purposes. Nevertheless, several other methods can also be used for the fitting of the Gumbel distribution. These other methods are known as the method of maximum likelihood (MML), the probability-weighted moments (PWM), and the method of L-moments (MLM) or the Lieblein BLUE. The implementation of these methods for the Gumbel distribution are not considered in this study. The study of the relative performance of these different fitting methods is studied by Hong (2013), in terms of their efficiency, bias, and root means square error.

For the Gumbel distribution, the sample mean and standard deviation are defined by $\hat{u} + 0.577\hat{a}$ and $\pi\hat{\alpha}/\sqrt{6}$, respectively. Where \hat{u} and \hat{a} are the estimated location and scale parameter. When the MOM is used, the estimated parameters of the distribution are defined based on the samples mean and standard deviation. In contrast, when the LSM is considered, the estimated distribution parameters are the product of an optimization problem based on the minimization of the distance between observed and predicted value from the distribution. Contrary to the Gumbel distribution, the GEV distribution requires a non-linear model for the process of optimization. In this case three parameters are necessary for the numerical optimization, which in this case include the scale u , the

location α and the shape ξ parameter. Similar as in the case of the LSM, the non-linear least square optimization for the GEV distribution consists in the minimization of the distance between observed ranked data and the fitting distribution model. Generally the relation between the difference from estimated and ranked value is called the residual.

The p.d.f. and the cumulative density function (c.d.f.) for the GEV distribution (Martins, 2000), are given by:

$$f_X(x) = \frac{1}{\alpha} ([1 + \xi y])^{-\frac{1}{\xi}-1} \exp \left\{ -(1 + \xi y)^{-\frac{1}{\xi}} \right\} \quad (\text{B.4a})$$

$$F_X(x) = \exp \left(-(1 + \xi y)^{-\frac{1}{\xi}} \right) \quad (\text{B.4b})$$

where y is the reduce variate (see Eq. B.1b), ξ the shape parameter, $f_X(x)$ the p.d.f. and $F_X(x)$ the c.d.f. One of the advantages of the GEV distribution is that the Gumbel, Fréchet, and Weibull distributions are contained within this same distribution, based on the shape parameter ξ . The extreme value distribution types II and III, referred as the Fréchet and Weibull distribution corresponds to the GEV distribution when the shape parameter is $\xi < 0$ or $\xi > 0$ (Coles, 2011), respectively. In contrast, the Gumbel distribution represents the limit case of the GEV distribution when $\xi \rightarrow 0$, leading to the Fisher Tippett Type I, or Gumbel distribution (Gumbel, 2004).

For the GEV distribution, the estimated values for each ranked annual maximum are given by $F_i(x_m)$ (see Eq. B.4b), as a function of the scale, location, and shape parameter (α, u and ξ). For the optimization of the GEV distribution, our main interest is focused on the merit function. The merit function which in this case minimizes the sum of residuals is given by (Pujol, 2007), :

$$s(x) = \sum_{i=1}^N \left(F_i(x_m) - \hat{G}_i(x_m) \right)^2 \quad (\text{B.5})$$

where $F_i(x_m)$ is given by Eq. B.4b, $G_i(x_m)$ is the empirical probability of the mean annual maximum wind speed given by $m/(N+1)$, where m represents the ranked value, $\hat{G}_i(x_m)$ the estimated value of $G_i(x_m)$, and N the number of years of available data for each station.

Martins and Stedinger, (2000) compared the performance of the maximum likelihood estimators (MLE), the method of moments (MOM) and the L-moments estimator. In this case, their study suggest that the MLE is preferred in comparision to the other methods in relation to their efficiency, bias, and root mean square error.

A practical solution of the non-linear least square problem is presented by the MLE, with the aid of the Newton-Raphson method for the optimization of the parameters of the distribution. One of the advantages of the Newton-Raphson method is that it approximates second-order derivatives by the well known Jacobian i.e., the squared product of the Jacobian $J * J^T$ is equivalent to the Hessian matrix. This particular issue is of great advantage since it allows to find without much numerical difficulty the values of the scale, location, and shape parameter.

A typical approach for solving the c.d.f. of the GEV distribution $F_i(x)$, is in terms of the well known Taylor series expansion, by making an estimation of the solution by expanding in relation to an initial guess point,

$$F_i(x) \approx \hat{G}_i(x_0) + \sum_{j=1}^N \left. \frac{\partial F_i}{\partial x_i} \right|_{x=x_0} (x_i - x_i^0); \quad i = 1, \dots, N \quad (\text{B.6})$$

By simplifying the notation for the expansion, in terms of $\delta_i = x_i - x_i^0$, and $c_i = F_i(x) - \hat{G}_i(x_0)$, the merit function (Pujol, 2007), is given by:

$$s(x) = (c^T - \delta^T J^T)(c - \delta J) = c^T c - 2c^T J \delta + \delta^T J^T J \delta \quad (\text{B.7})$$

The minimization of the merit function $s(x)$, requires the computation of the derivatives of Eq B.7 in relation to δ_i , and setting Eq B.7 equal to zero,

$$(J^T J) \delta_i = -J^T c_i \quad (\text{B.8})$$

As mentioned previously, an advantage of the Gauss-Newton method is that the Hessian matrix is approximated by the product of the Jacobian $J^T J$, and second-order derivatives are not necessary. Thus, based on the maximum likelihood score function (Gatey, 2011),

$$\frac{\partial}{\partial u} \log f_i(x) = -\frac{\xi}{\alpha(1+\xi y_i)} - \frac{1}{\alpha} (1 + \xi y_i)^{-\frac{1}{\xi}-1} \quad (\text{B.9a})$$

$$\frac{\partial}{\partial \alpha} \log f_i(x) = -\frac{1}{\alpha} + \frac{(1+\xi)y_i}{\alpha(1+\xi y_i)} - \frac{y_i}{\alpha} (1 + \xi y_i)^{-\frac{1}{\xi}-1} \quad (\text{B.9b})$$

$$\frac{\partial}{\partial \xi} \log f_i(x) = -\frac{1}{\xi^2} \log(1 + \xi y_i) \left(1 - (1 + \xi y_i)^{-\frac{1}{\xi}}\right) - \frac{y_i \left(1 + \xi - (1 + \xi y_i)^{-\frac{1}{\xi}}\right)}{\xi(1 + \xi y_i)} \quad (\text{B.9c})$$

where $f_i(x)$ is the p.d.f. (see Eq. B.4a), y_i the reduced variate (see Eq. B.1b), u the location parameter, α the scale parameter, and ξ the shape parameter. For the solution of the merit function $s(x)$ (see Eq. B.5), a damped solution can be used such as the one presented by Levenberg (1944), or the one purposed by Marquardt (1963). For the numerical optimization problem, the Levenberg- Marquardt damped least-squares solution is given by(Pujol, 2007),

$$(J^T J + \lambda I) \delta_i = -J^T c_i \quad (\text{B.10})$$

where I is an identity matrix, $\delta_i = x_i - x_i^0$, $c_i = F_i(x) - \hat{G}_i(x)$, and λ is a functional parameter that can take different values in order to approach the minimization process of the merit function $s(x)$, and that can change its value depending on each consecutive iteration. Thus, as a first step in the solution of the merit function $s(x)$, we define $\lambda_1 = 0.1$ and $\lambda_1 = 10$, and obtained the corresponding merit function, $s_{\lambda_1=0.1}(x)$ and $s_{\lambda_1=10}(x)$. From the first iteration, the smallest value obtained from the merit function is stored, and we proceed to the next iteration. When the merit function $s(x)$ is closer to the solution, λ approaches zero. In contrast, when the values of $s(x)$ is distant from the solution, λ takes a high value. In the former case the solution converges to the Gauss-Newton method, while in the latter to the Steepest Descent method. Even though, the latter case can guarantee the convergence of the solution, this method becomes extremely slow after a couple of iterations. Both of the methods originally purposed by Marquardt (1963), or by Levenberg (1944) can take the best features of both the Gauss-Newton and the Steepest descent methods.

B.4 Roughness correction

Well established procedures are used for the roughness correction into a single type of terrain exposure, which is generally considered as open country exposure. The correction of the exposure based on ESDU standards follows the criteria followed by Harris and Deaves boundary layer method (Harris and Deaves, 1980; Deaves, 1981). The considered procedure incorporates the transitions of roughness length over varying fetches. Most of the land use considered for the categorized stations are divided into built-up areas or farmlands (see Table B 1).

Table B 1 List of roughness lengths (after ESDU, 01008).

BUILT-UP AREAS				
	Centres of large towns and cities:	Centres of small towns:	Suburbs, villages:	Airports; runway area:
z_0 (m) =	0.7	0.5	0.3	0.03

FARMLAND				
	Many trees, hedges, few buildings:	Many hedges, some trees:	Hedges, few trees:	Open country with isolated trees, some hedges:
z_0 (m) =	0.2 to 0.3	0.08	0.05	0.03

The simplified method proposed by Hong, (2013) can also be used for the roughness correction. In this method the annual maxima is assigned to different azimuthal bins at 10° increments, based on the wind direction. None of this methodologies are considered within this study, for simplicity on the correction of erroneous data within the different datasets.. Nevertheless, most of the stations analysed within this study presented regular conditions of roughness, in general. However, stations that could differ from the previous type of homogenization into a single category of terrain, are identified. The identified stations are marked with an asterisk before the name of the station (see Tables B 2 and B 3). For instance, Table B 2 displays the stations of Mexico, where nine stations were identified as presenting inhomogeneous roughness. In contrast, 47 stations are considered as having homogeneous roughness conditions.

Table B 2 Name of station, location and number of years of available data for stations in Mexico

No.	state	station*	latitude	longitude	number of years of data
1	Baja California	*GENERAL_RODOLFO_SANCHEZ_TABOAD	32.63	-115.24	28
2		ISLA_GUADALUPE	29.17	-118.32	21
3		SAN_FELIPE_BCN	31.03	-114.85	33
4	Baja California Sur	GENERAL_MANUEL_MARQUEZ_DE_LEON	24.07	-110.36	42
5		*LA_PAZ_BCS	24.17	-110.30	41
6		LOS_CABOS_INTL	23.15	-109.72	25
7	Campeche	CIUDAD_DEL_CARMEN_INTL	18.65	-91.80	30
8		INGENIERO_ALBERTO_ACUNA_ONGAY	19.82	-90.50	27
9	Chihuahua	HIDALGO_DEL_PARRAL_CHIH	26.93	-105.67	29
10		NUEVA_CASAS_GRADES_CHIH	30.37	-107.95	35
11		TEMOSACHIC_CHIH	28.95	-107.82	37
12	Coahuila	*MONCLOVA_INTL	26.96	-101.47	26
13		PLAN_DE_GUADALUPE_INTL	25.55	-100.93	25
14	Colima	'MANZANILLO_COL	19.05	-104.32	41
15		'PLAYA_DE_ORO_INTL	19.15	-104.56	39
16	Distrito Federal	LICENCIADO_BENITO_JUAREZ_INTL	19.44	-99.07	26
17	Durango	*DURANGO_DGO	24.05	-104.60	43
18		DURANGO_INTL	24.12	-104.53	42
19	Estado de Mexico	*LICENCIADO_ADOLFO_LOPEZ_MATEOS	19.34	-99.57	27
20		'TOLUCA_MEX	19.28	-99.68	33
21	Guanajuato	GUANAJUATO_GTO	21.00	-101.28	38
22		GUANAJUATO_INTL	20.98	-101.48	27
23	Guerrero	ACAPULCO_GRO	16.75	-99.75	42
24		CHILPANCINGO_RO	17.55	-99.50	42
25		GENERAL_JUAN_N_ALVAREZ_INTL	16.76	-99.75	43
26		'IXTAPA_ZIHUATANEJO_INTL	17.60	-101.46	37
27	Hidalgo	PACHUCA_HGO	20.13	-98.75	34
28	Jalisco	COLOTLAN_JAL	22.10	-103.27	22
29		*DON_MIGUEL_HIDALGO_Y_COSTILLA	20.52	-103.31	28
30		GUADALAJARA_JAL	20.67	-103.38	35
31		LICENCIADO_GUSTAVO_DIAZ_ORDAZ	20.68	-105.25	28
32	Michoacan	MORELIA_MICH	19.70	-101.18	41
33	Monterrey	*DEL_NORTE_INTL	25.87	-100.24	45
34	Morelos	GENERAL_MARIANO_MATAMOROS	18.84	-99.26	28
35	Nayarit	TEPIC	21.42	-104.84	28
36	Oaxaca	HUAJUAPAN_DE_LEON_OAX	17.80	-97.77	33
37		'PUERTO_ANGEL_OAX_1	15.68	-96.48	33
38		'PUERTO_ESCONDIDO_INTL	15.88	-97.09	29

39	Puebla	HERMANOS_SERDAN_INTL	19.16	-98.37	29
40	Queretaro	QUERETARO_INTERCONTINENTAL	20.62	-100.19	23
41	Quintana Roo	CANCUN_INTL_1	21.03	-86.87	20
42		'CHETUMAL_INTL	18.51	-88.33	44
43		COZUMEL_INTL 1	20.52	-86.92	21
44		FELIPE_CARRILLO_PUERTO_Q_ROO	19.57	-88.05	35
45	San Luis Potosi	RIO_VERDE_S.L.P	21.93	-99.98	35
46	Sinaloa	CHOIX_SIN	26.73	-108.28	32
47	Sonora	CIUDAD_OBREGON_SON	27.48	-109.92	21
48	Tamaulipas	CIUDAD_VICTORIA_TAMPS	23.73	-99.13	45
49		GENERAL_PEDRO_JOSE_MENDEZ_INTL	23.70	-98.96	31
50		*QUETZALCOATL_INTL	27.44	-99.57	28
51	Tlaxcala	*TLAXCALA_TLAX	19.317	-98.25	36
52	Veracruz	COATZACOALCOS_VER	18.183	-94.5	32
53		ORIZABA_VER	18.85	-97.1	31
54	Yucatan	PROGRESO_YUC	21.3	-89.65	30
55		VALLADOLID_YUC	20.683	-88.2	41
56	Zacatecas	SOMBRETERE_ZAC	23.633	-103.650	39

(*) inhomogeneous roughness

In addition, Table B 3 presents the stations near the borders of U.S.A., Guatemala, and Belize. In this case, only one station is considered as inhomogeneous (see Table B 3).

Table B 3 Name of station, location and number of years of available data for stations in the boarder of U.S.A., Guatemala and Belize.

No.	country	station*	latitude	longitude	Number of years of data
1	USA	BURBANK-GLENDALE-PASA_ARPT	34.201	-118.358	37
2		LONG_BEACH_DAUGHERTY_FIELD	33.812	-118.146	67
3		MARINE_CORPS_AIR_STATION	33.3	-117.35	35
4		NAF	32.817	-115.683	34
5		NORTH_ISLAND_NAS	32.7	-117.2	73
6		SAN_NICOLAS_ISLAND_NAVAL_OUTLY	33.24	-119.458	35
7		SOUTHERN_CALIFORNIA_LOGISTICS	34.583	-117.383	50
8		TWENTY_NINE_PALMS	34.3	-116.167	28
9		*EL_PASO_INTERNATIONAL_AIRPORT	31.811	-106.376	68
10		MARFA_MUNICIPAL_AIRPORT	30.371	-104.017	34
11		ROSWELL_INTERNATIONAL_AIR_CENT	33.308	-104.508	68
12		LAUGHLIN_AFB_AIRPORT	29.367	-100.783	54
13		SAN_ANGELO_REGIONALMATHS_FIEL	31.352	-100.495	45

14		WINKLER_COUNTY_AIRPORT	31.78	-103.202	40
15		DAVIS-MONTHAN_AFB_AIRPORT	32.167	-110.883	65
16		ERNEST_A_LOVE_FIELD_ARPT	34.652	-112.421	28
17		LUKE_AFB_AIRPORT	33.55	-112.367	59
18		PHOENIX_SKY_HARBOR_INTL_AIRPOR	33.428	-112.004	45
19		SIERRA_VISTA_MUNICIPAL-LIBBY_A	31.588	-110.344	53
20		WILLIAMS_GATEWAY_AIRPORT	33.3	-111.667	62
21		YUMA_MARINE_CORPS_AIR_STATION	32.667	-114.6	27
22		CHASE_NAVAL_AIR_STATION	28.367	-97.667	20
23		CORPUS_CHRISTI_INTERNATIONAL	27.774	-97.512	63
24		CORPUS_CHRISTI_NAS	27.683	-97.283	45
25		HONDO_MUNICIPAL_AIRPORT	29.36	-99.174	34
26		LACKLAND_AIR_FORCE_BASE_KELLY	29.383	-98.583	72
27		RANDOLPH_AFB_AIRPORT	29.533	-98.262	70
28		SAN_ANTONIO_INTERNATIONAL_AIRP	29.544	-98.484	66
29	Guatemala	FLORES_SANTA_ELENA	16.917	-89.883	22
30		HUEHUETENANGO	15.317	-91.467	38
31		LA_AURORA	14.583	-90.527	40
32		SAN_JOSE	13.936	-90.836	23
33	Belize	PHILIP_S_W_GOLDSON_INTL	17.539	-88.308	25

(*)inhomogeneous roughness

Some examples concerned to the categorization of roughness length for some stations is discussed above. From the Google maps landscape the surrounding of the station are presented. In this case, a zoom within two and ten kilometers is shown. For the station of Guadalajara presented in Fig B 6, a roughness length z_0 of 0.5 is considered. In this case, the roughness characterisation is considered as an homogeneous condition throughout the periphery. Similar as to the station of Guadalajara, a roughness length of 0.5 is also considered for the state of Toluca (station no. 20, Table B 2). This particular roughness length is a typical value that is regularly used in the case of centres of small towns. Both Guadalajara and Toluca are relatively dense cities, within the country of Mexico. Small towns is referred more to the average height of the surrounding buildings, instead of the size of the city. Therefore, when cities as Toluca and Guadalajara are referred as small towns, this is in reference to big cities with high skyscrapers such as New York in U.S.A., Toronto, in Canada, or Mexico city in the country of Mexico. Therefore, from all the analysed meteorological stations, the highest roughness length was considered for the airport station in Mexico City (station no. 16, Table B 2), with a value of z_0 of 0.7.

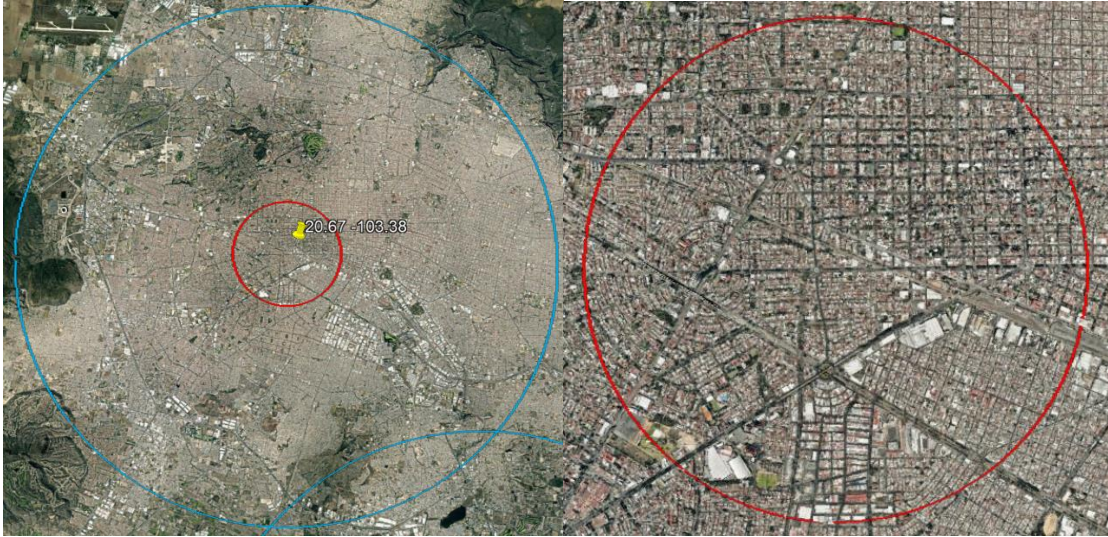


Figure B 6 Station of Guadalajara, Jalisco (circumference of 4 and 20 km in diameter).

Another example of roughness correction is presented in Fig. B 7, for the station of Oaxaca, in the village of Huajuapán de León. In this case, the terrain is not as homogeneous as in the previous example considered for the station of Guadalajara (Fig. B 6). However, the homogenization of the terrain is still considered. In this case, a roughness length z_0 of 0.3, is assigned for the first two kilometers. After the first two kilometers, the surrounding area is classified as farmland with many hedges and few trees. In this case, the roughness length is considered as 0.08.

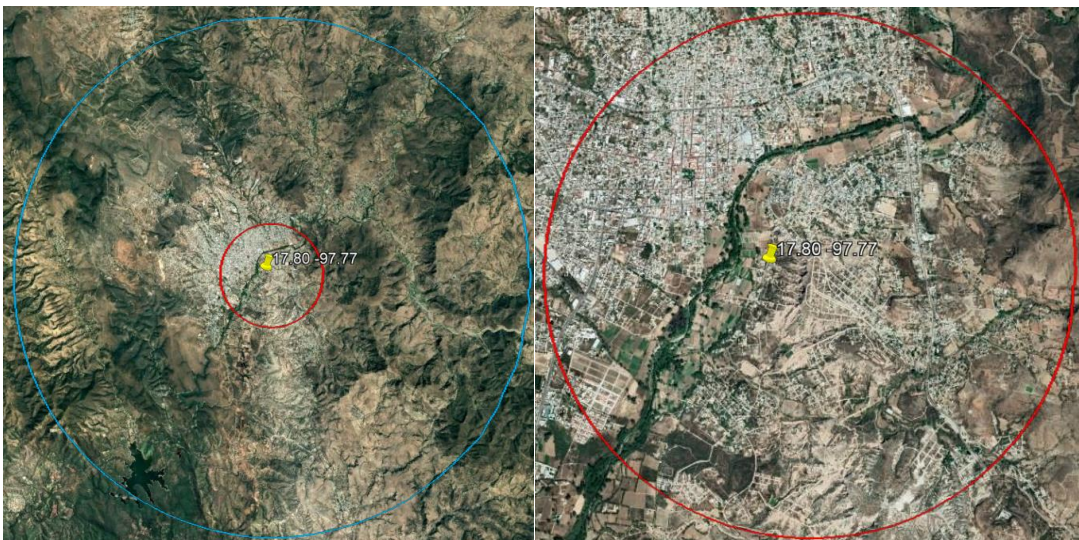


Figure B 7 Station Huajuapán de León, Oaxaca.

Another example of roughness correction is presented for the station of Morelia Michoacan (Fig B 8). In this station, a roughness length z_0 of 0.3 is considered, in the case of the the first four kilometers. Beyond the first four kilometers of radius, a z_0 of 0.2 is considered. In the former case, the zone is categorized as suburbs and villages, and in the latter as farmland with many trees and hedges and few buildings. Similar corrections as the ones presented in this section are generated for all the stations (Table B 2 and B 3), considered within the analysis.

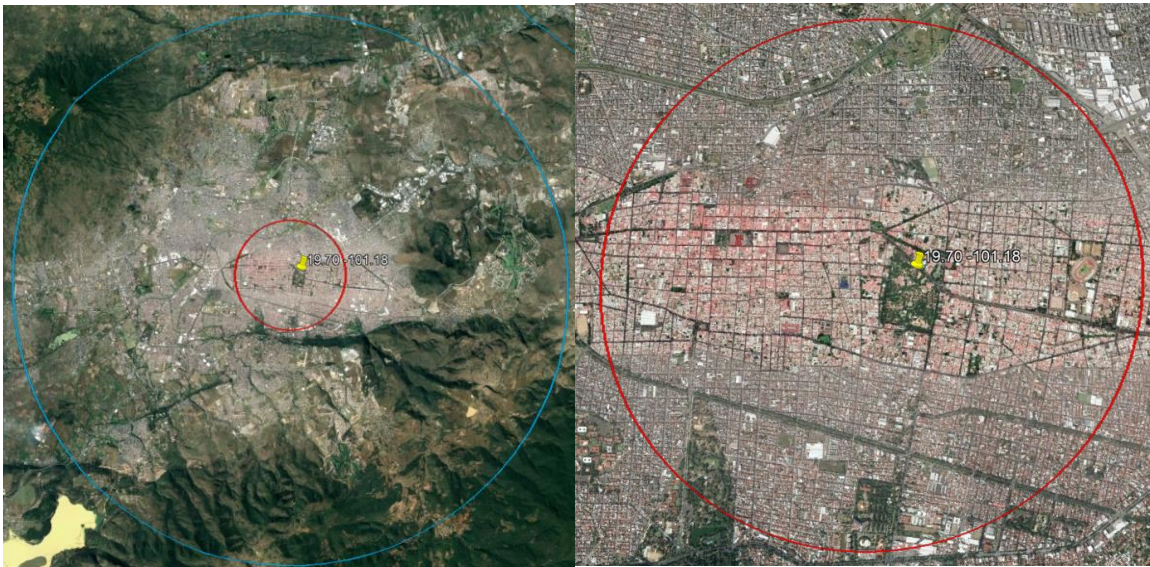


Figure B 8 Station Morelia, Michoacan.

B.5 Results and discussion

The 200-year mean annual maximum wind speed for a different states in Mexico (see also Table B 2) is presented in Table B 4. The probability paper for some of the analyzed stations is presented in section B 7. The fitted data presents good stability that is seen throughout the linearized distribution of the Gumbel or GEV distribution. Another important attribute of the selected data is the quality and stability that the upper tail of the linearized distribution presents. This aspect within the linearized distribution guarantees the efficiency and the accurate prediction of the extreme. As it is observed within the Gumbel probability paper (see section B 7), the stability of the upper tail of the linearized data is appropriate and in all cases promotes the stability of the data.

For accepting or rejecting data within the analysis of the different meteorological stations, the predicted models were evaluated based on the Kolmogorov-Smirnov test. In this type of test, the allowed deviation between the observed value and predicted model is tested. From the Kolmogorov-Smirnov tests, most of the fitting distributions fall above 80% of the confidence level. The Kolmogorov-Smirnov test for different stations, and considering a particular significance level, are shown in Table B 4. In the Table are also presented the day of the registered maximum wind speed and its value, the 200 year mean annual maximum wind speed and the used distribution model.

Table B 4 200 year mean annual maximum wind speeds for the stations of Mexican

No.	maximum wind registered	day of maximum wind	distribution type	Mean annual maximum wind speed (km/h)	Kolmogorov Smirnov test		
					α	Dcrit, α	Dn
1	118.80	1992-11-29	Gumbel	148.0	0.20	0.197	0.141
2	118.80	1990-10-20	GEVD	144.4	0.20	0.226	0.081
3	115.20	2006-01-21	Gumbel	148.2	0.20	0.186	0.095
4	115.20	1992-07-25	GEVD	159.4	0.20	0.165	0.124
5	115.20	1991-04-30	Gumbel	167.4	0.20	0.167	0.128
6	111.24	1995-10-28	Gumbel	173.0	0.20	0.208	0.140
7	111.24	1991-06-28	GEVD	140.4	0.20	0.190	0.128
8	111.60	2013-04-20	GEVD	176.7	0.20	0.200	0.141
9	118.80	1989-03-06	Gumbel	183.2	0.20	0.193	0.091
10	108.00	2006-02-19	Gumbel	142.4	0.10	0.202	0.201
11	108.00	1998-11-09	Gumbel	145.4	0.20	0.176	0.082
12	100.08	2007-10-23	Gumbel	129.9	0.20	0.204	0.201
13	118.44	2005-12-11	GEVD	163.7	0.20	0.208	0.104
14	118.80	1989-08-11	Gumbel	147.2	0.20	0.167	0.116
15	111.24	1994-11-18	GEVD	119.9	0.20	0.171	0.146
16	107.28	2005-02-08	GEVD	193.2	0.20	0.204	0.172
17	133.20	1997-02-07	GEVD	194.7	0.20	0.163	0.119
18	120.24	2000-12-18	GEVD	158.5	0.20	0.165	0.147
19	108.00	1992-09-08	GEVD	183.3	0.20	0.200	0.138
20	115.20	1998-05-02	Gumbel	229.0	0.20	0.186	0.137
21	90.00	1996-06-28	GEVD	135.9	0.20	0.226	0.109
22	118.44	1994-12-01	GEVD	144.3	0.20	0.221	0.179
23	108.00	2007-02-11	GEVD	127.1	0.20	0.216	0.170
24	108.00	2004-06-07	Gumbel	195.9	0.20	0.165	0.067

25	110.88	1976-05-10	GEVD	121.8	0.02	0.232	0.209
26	111.24	2001-06-05	GEVD	139.0	0.10	0.201	0.179
27	118.80	2008-03-12	Gumbel	210.4	0.20	0.200	0.060
28	97.20	2014-03-26	Gumbel	144.4	0.20	0.221	0.116
29	110.88	1993-01-12	GEVD	148.9	0.20	0.197	0.139
30	108.00	2008-11-18	GEVD	236.1	0.20	0.177	0.154
31	101.52	1993-04-23	GEVD	121.1	0.20	0.197	0.125
32	108.00	1995-01-30	GEVD	162.9	0.20	0.167	0.132
33	115.20	1992-12-05	GEVD	170.0	0.20	0.156	0.103
34	118.80	2016-11-19	GEVD	183.4	0.20	0.197	0.137
35	104.40	2017-05-08	GEVD	143.3	0.20	0.197	0.133
36	115.20	1997-07-27	GEVD	166.1	0.20	0.186	0.122
37	118.80	1998-09-16	Gumbel	173.8	0.20	0.186	0.095
38	111.24	1998-10-17	Gumbel	167.2	0.20	0.193	0.097
39	118.80	1996-04-08	GEVD	162.1	0.20	0.193	0.132
40	118.44	1995-08-29	GEVD	147.3	0.20	0.216	0.175
41	107.64	1991-03-29	Gumbel	173.7	0.20	0.233	0.128
42	118.80	1994-05-07	GEVD	172.1	0.20	0.165	0.130
43	96.12	1993-11-27	Gumbel	167.4	0.20	0.226	0.112
44	115.20	2005-12-09	Gumbel	188.5	0.20	0.181	0.149
45	111.60	2006-03-26	Gumbel	197.2	0.20	0.181	0.133
46	104.40	2015-05-30	Gumbel	163.3	0.20	0.189	0.110
47	114.84	1974-04-18	GEVD	185.1	0.20	0.226	0.090
48	94.32	1975-04-28	GEVD	153.8	0.20	0.156	0.087
49	118.44	1988-01-20	Gumbel	177.3	0.20	0.192	0.130
50	111.24	1998-11-11	Gumbel	175.9	0.20	0.197	0.132
51	118.80	2002-11-29	Gumbel	215.0	0.20	0.178	0.098
52	111.60	2014-09-20	Gumbel	140.1	0.20	0.189	0.133
53	100.80	1998-01-07	GEVD	162.4	0.20	0.192	0.146
54	100.80	1990-01-13	Gumbel	122.0	0.20	0.190	0.076
55	90.00	2011-09-05	GEVD	157.9	0.20	0.167	0.097
56	108.00	1993-01-14	GEVD	146.3	0.20	0.171	0.108

The same information used for Table B.4., is now elaborated for the the stations located in the U.S.A, Guatemala, and Belize (see Table B 5). By observing the Kolmogorov-Smirnov test, most of the fitting data are above 80% of the confidence level. While for few station for both table B 4 and .B 5, the confidence level is even higher, for both table B 4 and .B 5.

Table B 5 200-year annual maximum wind speeds for U.S.A., Guatemala, and Belize.

No.	maximum wind registered	day of maximum wind	distribution type	Mean annual maximum wind speed (km/h)	Kolmogorov Smirnov test		
					α	Dcrit, α	Dn
1	114.84	1998-02-02	GEVD	174.9	0.10	0.201	0.182
2	101.88	1976-08-15	Gumbel	175.4	0.20	0.131	0.113
3	92.52	2005-09-23	Gumbel	122.6	0.20	0.177	0.076
4	101.88	2006-03-20	Gumbel	122.8	0.20	0.184	0.127
5	100.08	2005-05-25	GEVD	117.5	0.20	0.125	0.105
6	101.88	1992-01-17	Gumbel	104.4	0.20	0.177	0.076
7	87.12	1954-03-17	Gumbel	105.2	0.20	0.148	0.071
8	92.52	2004-08-24	Gumbel	111.7	0.20	0.197	0.126
9	100.08	1950-05-05	GEVD	138.3	0.20	0.148	0.105
10	116.64	1980-01-11	Gumbel	155.6	0.20	0.184	0.115
11	107.28	1980-01-11	Gumbel	122.8	0.20	0.130	0.101
12	111.24	1990-04-26	Gumbel	127.8	0.20	0.146	0.097
13	118.44	1980-03-31	Gumbel	134.3	0.20	0.156	0.119
14	113.04	1996-12-11	Gumbel	134.5	0.20	0.165	0.136
15	100.08	2011-07-05	Gumbel	135.4	0.20	0.131	0.081
16	83.52	2010-01-22	Gumbel	98.3	0.20	0.197	0.134
17	111.60	2016-07-30	GEVD	138.6	0.20	0.139	0.104
18	103.68	1978-10-20	GEVD	171.2	0.20	0.156	0.096
19	109.44	1997-04-24	GEVD	132.7	0.20	0.147	0.078
20	100.08	1945-08-02	GEVD	146.0	0.20	0.136	0.070
21	103.68	1978-12-09	Gumbel	172.2	0.20	0.200	0.099
22	97.92	1975-06-09	Gumbel	157.3	0.20	0.232	0.132
23	113.04	1947-05-20	GEVD	160.4	0.05	0.171	0.161
24	113.04	2010-08-07	Gumbel	152.8	0.20	0.156	0.140
25	87.12	2017-06-05	GEVD	119.5	0.20	0.184	0.100
26	114.84	1997-05-28	GEVD	180.1	0.20	0.126	0.104
27	103.68	1993-06-25	GEVD	149.5	0.20	0.128	0.105
28	116.64	1979-02-23	GEVD	192.8	0.05	0.167	0.155
29	64.80	2003-09-15	Gumbel	114.6	0.20	0.221	0.136
30	81.36	1988-11-09	Gumbel	138.6	0.20	0.174	0.124
31	115.20	1981-12-21	GEVD	189.4	0.20	0.165	0.100
32	105.48	2002-03-26	Gumbel	155.7	0.20	0.177	0.098
33	111.24	1994-05-30	Gumbel	178.8	0.20	0.208	0.159

For synoptic type of wind, the isopleths of the 200-year mean annual maximum wind speed are presented in Fig. B 9. The highest risk is presented throughout different regions

within the country, with variations in wind speed ranging from 168 to 195 km/h. From the Pacific coast, the peninsula of Baja California and part of Sinaloa present the highest wind speeds, while on the Gulf of Mexico, the border of Tamaulipas and Veracruz. Besides, in the central part of the country the states of Queretaro, Puebla, and Oaxaca are also prone to the highest wind speeds. The average value of the mean annual maximum wind speed within the country is in the range of 153 to 168 km/h, and is the typical value expected for most of the country, with the exception of the boarder between Mexico and the U.S.A. in which lower values of wind speed are expected

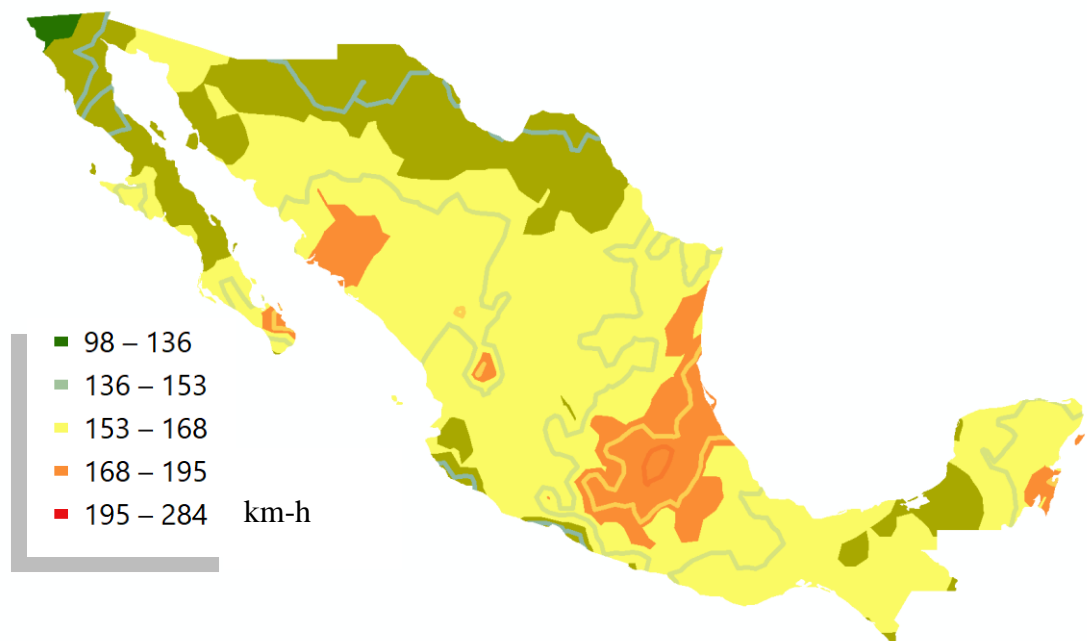
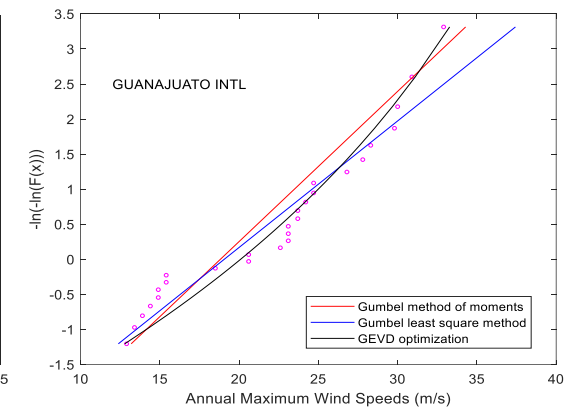
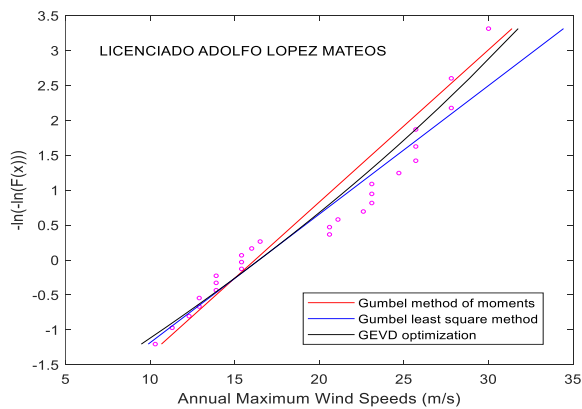
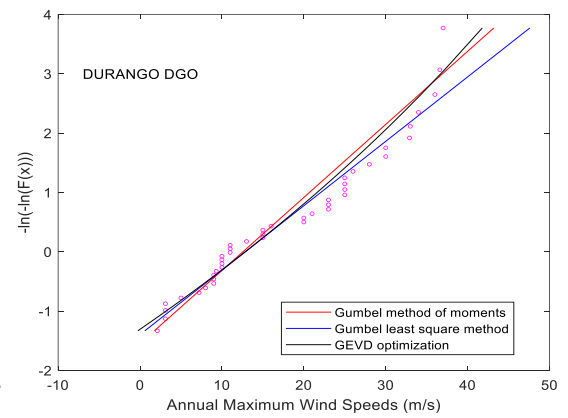
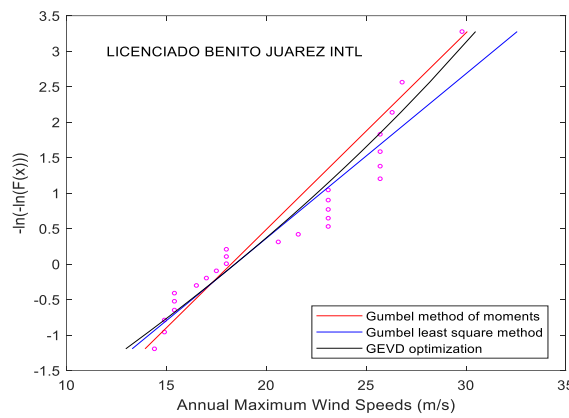
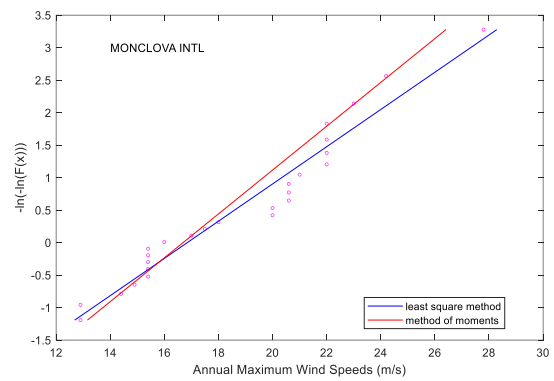
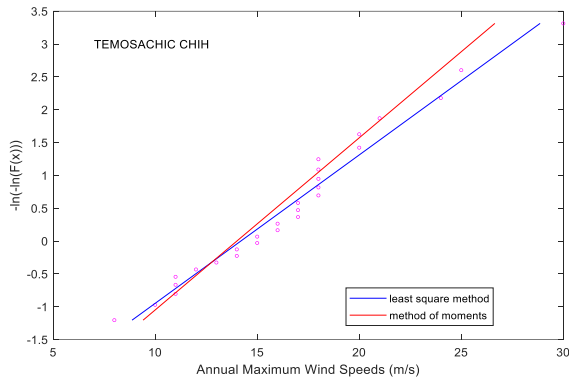


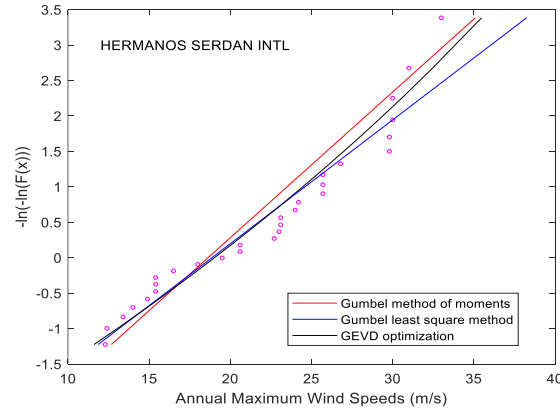
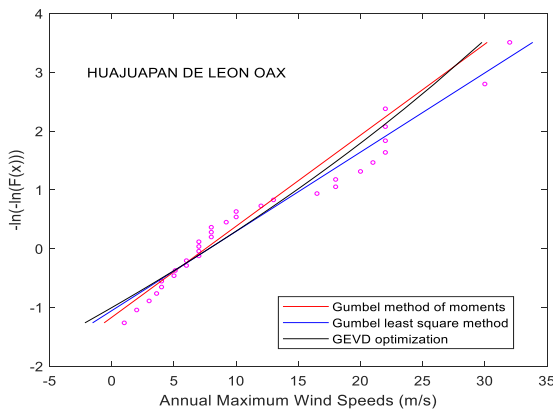
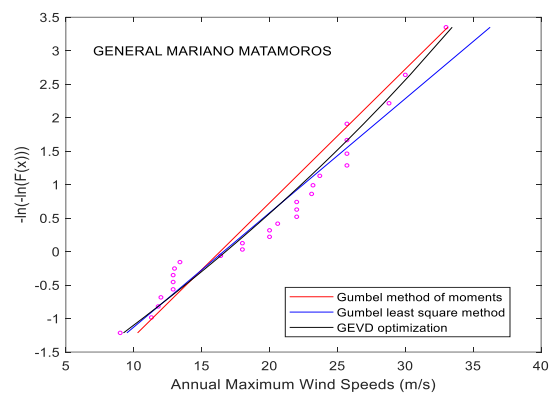
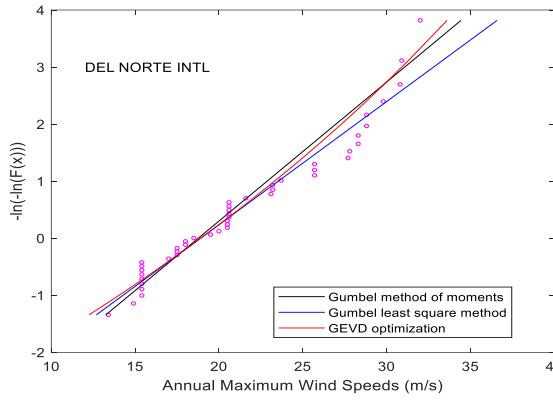
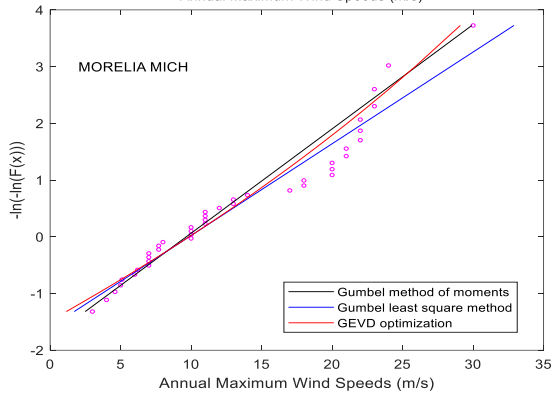
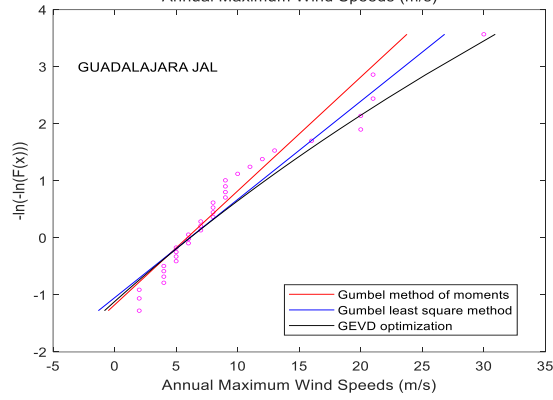
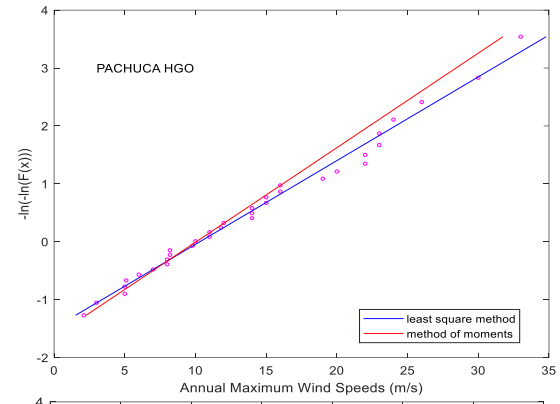
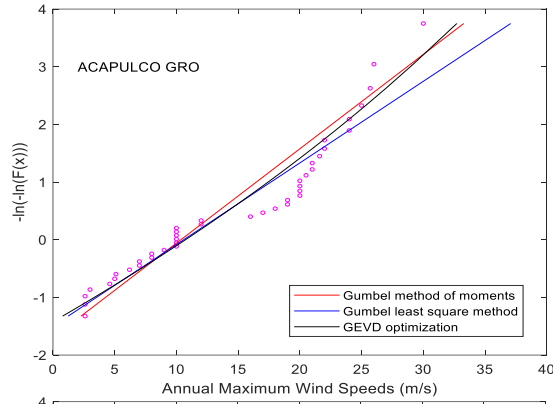
Figure B 9 Regional velocities for synoptic type of wind, from the NOAA datasets

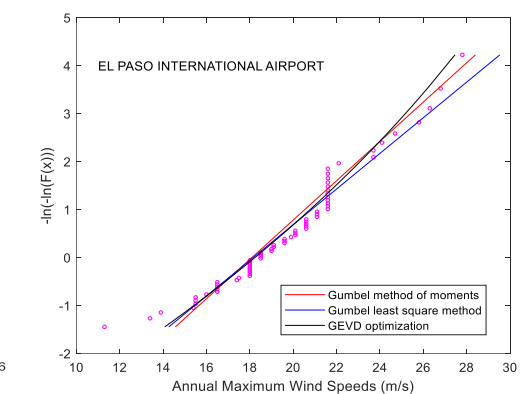
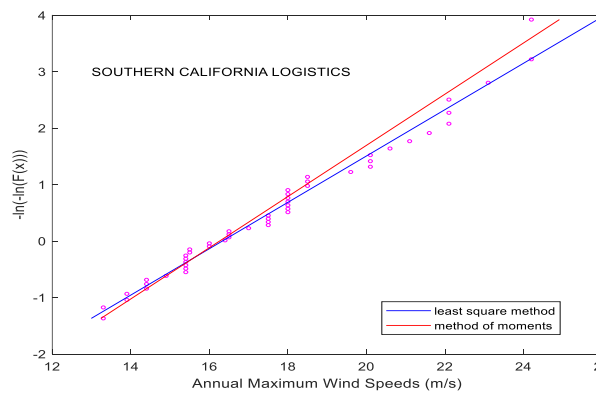
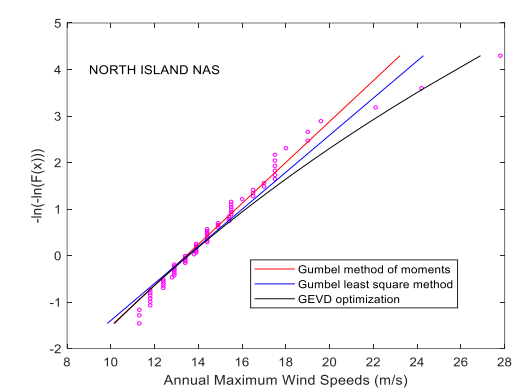
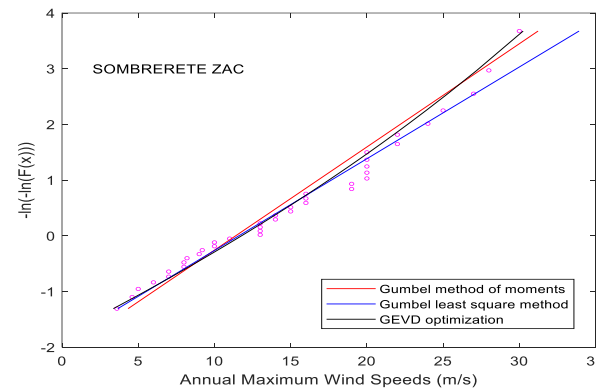
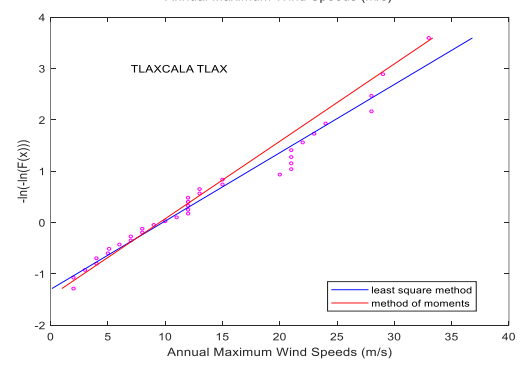
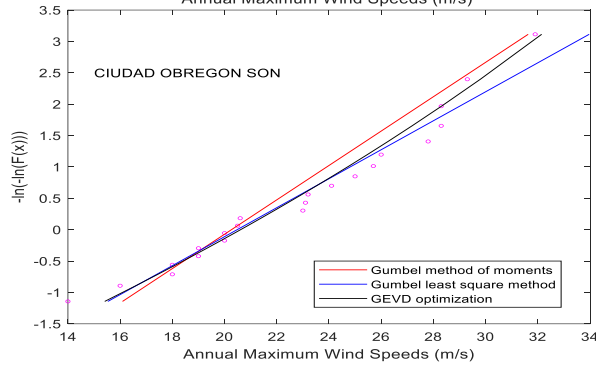
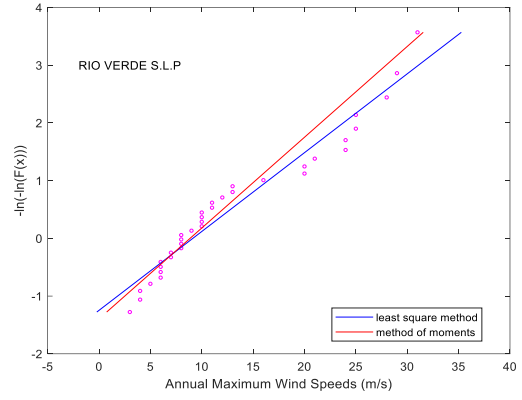
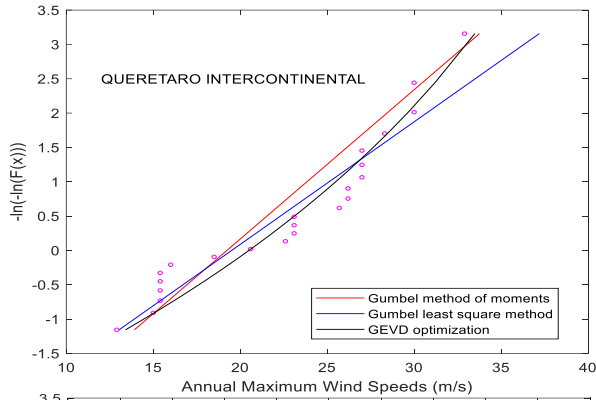
B.6 Conclusions

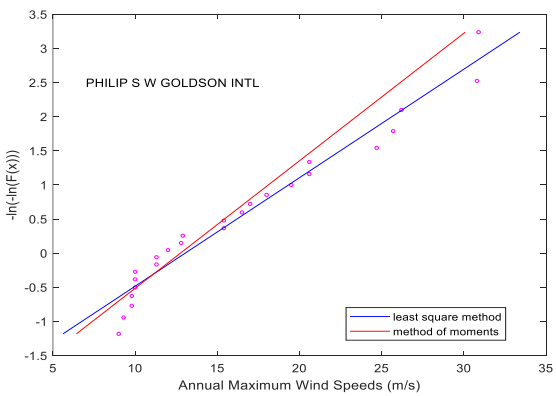
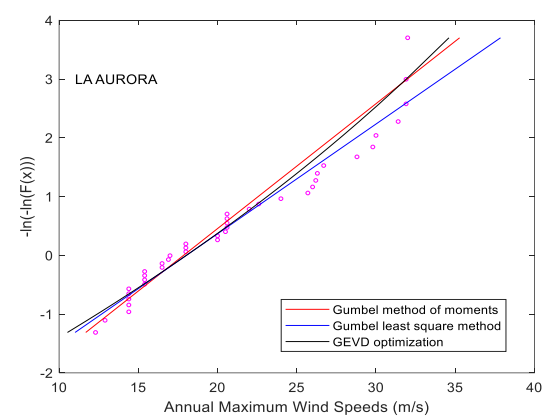
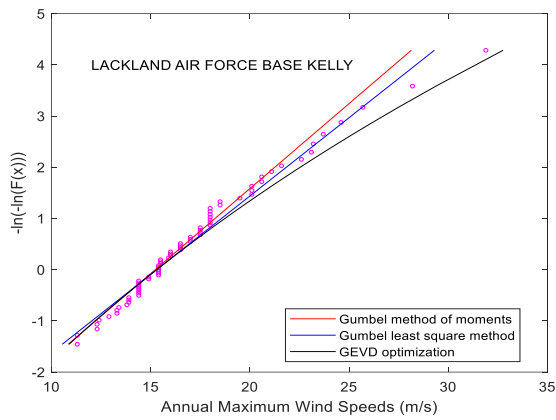
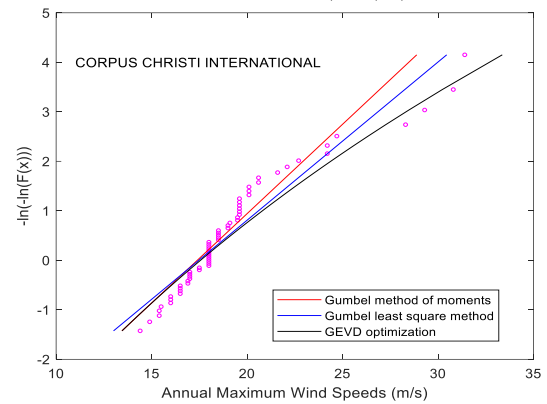
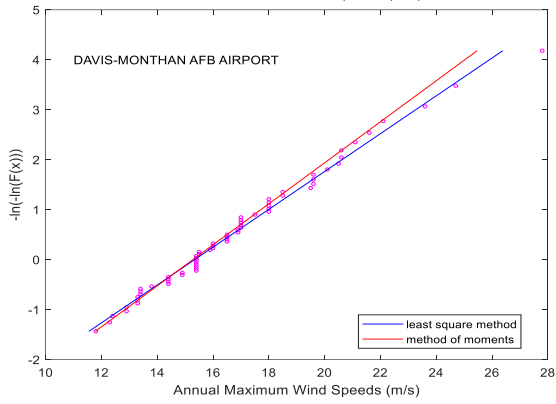
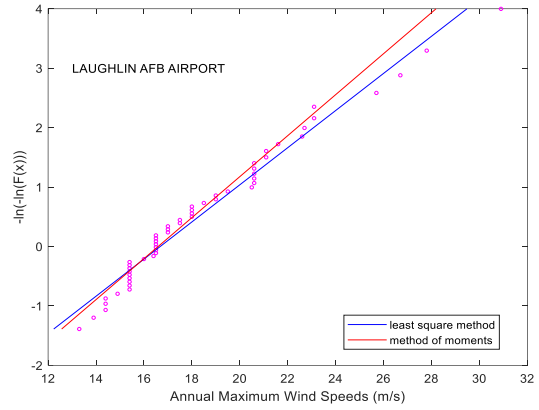
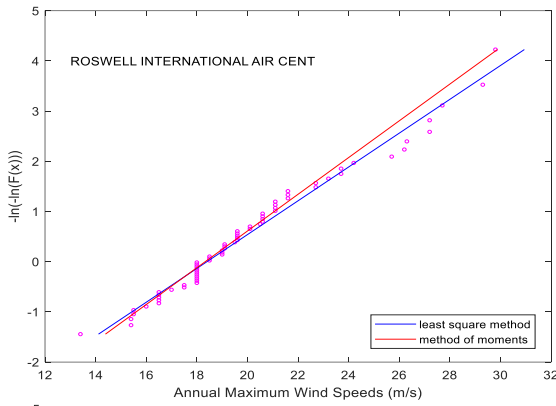
For the country of Mexico, a preliminary regional map of the 200-year mean annual maximum wind speed is presented. The analysis of wind speed is focused exclusively on synoptic type of wind. Before arriving at conclusions, it is important to acknowledge the actual condition of the existing datasets from the different meteorological stations. One of the main objectives from this study was to generate a more standard and homogeneous database for the analysis of wind speeds. Therefore, the correction of raw data was established in a systematic manner. For the extreme value analysis, the Gumbel and the Generalized Extreme Value (GEV) distribution are used as fitting models. The roughness correction of the terrain is also presented. From the total number of analysed stations only the stations that presented the best fit for the Gumbel or GEV distribution were selected. In this case, fifty-seven stations from Mexico, twenty-nine stations from the U.S.A., four from Guatemala, and one from Belize, were considered in the analysis of wind records. The analysis of the isopleths for the 200-year return period maps is mainly based on synoptic type of wind. A further inclusion of hurricane wind is not considered, since the data that was analysed in most cases was found to be highly contaminated. In this case, for synoptic type of wind, the highest risk is presented within the lower region of Baja California Sur and the upper part of Sinaloa on the Pacific coast, and near the border of Tamaulipas and Veracruz on the Gulf of Mexico. Besides, in the center of the country, the states of Queretaro, Puebla, and Oaxaca, are also sensitive to high wind speeds.

B 7 Prediction models from the Gumbel and Generalized extreme value (GEV) distribution









B.7 References

- Aguirre, J.E., Sanchez-Sesma, J. (1986). Probabilistic considerations in Transmission Line Wind Design for Mexico, Probabilistic Methods Applied to Electric Power Systems, Proceedings of the First International Symposium, Toronto, Canada, (1986).
- Bradford, F. K. (1955). Application of the Theory of Extreme Values. *Journal. of the American Statistical Association.*, 50, (270), 517-528.
- Coles, S., (2011). *An Introduction To Statistical Modeling Of Extreme Values (Springer Series In Statistics)* . Heidelberg, Germany: Springer.
- Deaves, D.M. 1981. Computations of wind flow over changes in surface roughness. *Journal of Wind Engineering and Industrial Aerodynamics*, 7(1), 65-94.
- ESDU. 2002. Computer program for wind speeds and turbulence properties: flat or hilly sites in terrain with roughness changes. ESDU Data Item No. 01008.
- ESRI. 2011. ArcGIS Desktop: Release 10. Redlands, CA: Environmental Systems Research Institute.
- Comisión Federal de Electricidad (2008). “Diseño por Viento, Manual de Diseño de Obras Civiles de la CFE.”, México. (In Spanish).
- Crutcher, H.L. (1975). A note on the possible misuse of the Kolmogorov-Smirnov test. *Journal of Applied Meteorology*. 14,(8),1600-1603.
- Gatey. (2011). The analysis of extreme synoptic wind. *PhD Thesis. The Univeristy of Western Ontario*.
- Gumbel, E.J. (2004). *Statistics of extremes*. Dover. Mineola. New York.

- Harris, R.I. and Deaves, D.M. (1980). The structure of strong winds. Paper 4 CIRIA Conference on “Wind Engineering in the Eighties”. Construction Ind.Res and Inf, Assoc, London
- Hong, H.P.,Mara, T.G. (2013). Performance of the generalized least-square method for the Gumbel distribution and its application to annula maximum wind speeds. Journal of Wind Engineering and Industrial Aerodynamics, 119, 121-132.
- Infraestructura Educativa & Secretaría de educaión Punlica (INIFED & SEP). (2015). “Normas y Especificaciones para Estudios, Proyectos, Construcción e Instalaciones”, 4(3):1-24
- Kimball, B.F.(1955). Application of the Theory of Extreme Values. Journal. of the American Statistical Association., 50(270): 517-528.
- Levenberg, K. (1944). A method for the solution of certain non-linear problems in least squares, Quarterly of. Applied. Mathematics, 2(2), 164-168.
- López, A., Vilar, J.I. (1995). Basis of the Mexican Wind Handbook for the Evaluation of the Dynamic Response of Slender Structures, Ninth International Conference of Wind Engineering, New Delhi, India.
- López, A.L., Sesma, J.S., Muñoz C.J., Pech,L.E.,(2018). Analysis of extreme wind speeds for structural design in Mexico, International Workshop on Wind-Related Disaster and Mitigation, Sendai, Japan.
- López, A.L., Sesma, J.S.,Black, C.J. Rocha,L.E.,Macías,C.C.(2008).Criterios óptimos en el diseño por viento para México.XVI Congreso Nacional de Ingeniería Estructural. Veracru,z México.
- Martins, E.S.,Stedinger, J.R. (2000). Generalized maximum-likelihood generalized extreme-value quantile estimators for hydrologic data.Water Resources Research, 36(3):737-744.

Marquardt, D.W. (1963), An algorithm for least-square estimation of nonlinear parameters, *Journal. Soc. Indust. Appl. Math.*, 11(2):431-441.

Palutikof, J.P., Brabson, B.B., Lister, D.H., Adcock, S.T. (1999). A review of methods to calculate extreme wind speeds. *Meteorol. Appl.* 6:119–132.

Pujol, J. (2007). The solution of nonlinear inverse problems and the Levenberg-Marquardt method, *Geophysics*, 72(4),W1-W16

Curriculum Vitae

Name: Héctor Hernández Landero

Post-secondary Education and Degrees:

The University of Western Ontario
London, Ontario, Canada
2015-2022 PhD (Structural Engineering)

National Autonomous University of Mexico
Mexico City, Mexico
2013-2015 M.S. Structural Engineering)

National Autonomous University of Mexico
Mexico City, Mexico
2012-2013 M.Eng (Structural Engineering)

University of the Americas Puebla (UDLAP)
Puebla, Mexico
1998-2003 B.Sc. (Civil Engineering)

Scholarship: National Council of Science and Technology of Mexico and Ontario Council of Graduate Studies Scholarship, 2015-2020

Related Work Experience

Research and Teaching Assistant
The University of Western Ontario
London, Ontario, Canada, 2015-2019

Research Assistant
Institute of Engineering, National Autonomous University of Mexico
Mexico City, Mexico, 2012-2015

Publications:

Pozos-Estrada, A., Gómez-Martínez, R., Hong, H.P, Hernández-Landero, H. (2015) “Wind induced response of a cable-stayed bridge under partially and fully correlated buffeting forces” 14th International Conference on Wind Engineering, Porto Alegre, Brazil